

I have discovered that the world over, unusual weather prevails at all times of the year.

—Edgar Rice Burroughs

University of Alberta

Intelligent Methods for Evaluating the Impact of Weather on Power Transmission Infrastructure

by

Pawel Maksymilian Pytlak

A thesis submitted to the Faculty of Graduate Studies and Research
in partial fulfillment of the requirements for the degree of

Doctor of Philosophy

in

Software Engineering and Intelligent Systems

Department of Electrical and Computer Engineering

© Pawel Maksymilian Pytlak
Fall 2012
Edmonton, Alberta

Permission is hereby granted to the University of Alberta Libraries to reproduce single copies of this thesis and to lend or sell such copies for private, scholarly or scientific research purposes only. Where the thesis is converted to, or otherwise made available in digital form, the University of Alberta will advise potential users of the thesis of these terms. The author reserves all other publication and other rights in association with the copyright in the

thesis and, except as herein before provided, neither the thesis nor any substantial portion thereof may be printed or otherwise reproduced in any material form whatsoever without the author's prior written permission.

ABSTRACT

Weather has a significant impact on human society, both in driving the life-giving physical processes that allow humans to meet their most basic needs, and as an adversarial force, often causing significant losses to property and life. The electrical power industry is particularly subject to significant weather influence due to the wide-scale exposure of its infrastructure to nature's elements. Severe storms can cause damage in the millions of dollars, and even directly or indirectly cause fatalities. Weather patterns and their impact on the industry are hard to predict using simple statistical measures, and thus more complex methodologies must be used to provide accurate forecasts and impact assessment. The increasing global awareness of climate change is driving the power industry to adopt more green energy sources. Unfortunately, these sources cannot be constructed at will; they must be harnessed where they are available. Consequently, the power industry is not always ready to incorporate these sources into the existing grid without costly infrastructure upgrades and/or expansion projects.

To help alleviate these concerns, this thesis presents intelligent methodologies that can use either modern Numerical Weather Prediction (NWP) models or direct weather observations to solve some of the challenges faced by the power industry. It describes the optimization and verification of an ice accretion forecast system that is tuned to increase its predictive accuracy us-

ing computational intelligence techniques. The performance of the system is also evaluated in a true forecast simulation. This thesis also describes the enhancement of an industry standard line rating model that is expanded to include the cooling impact of precipitation. Studies are presented that discover the optimal configuration of weather-based dynamic thermal rating systems, evaluate the accuracy and risk of forecasting line ampacity ratings using NWP models, and assess the reduction in emissions by using dynamic ratings to incorporate more green energy into the transmission grid. Finally, this thesis describes intelligent systems aimed at assisting and supporting planning decisions in transmission infrastructure construction and expansion projects.

ACKNOWLEDGMENTS

Firstly, I would like to thank my supervisors: Dr. Petr Musílek and Dr. Edward Lozowski for granting me the incredible opportunity to conduct this exciting research, for their support and guidance. Secondly, I would like to thank FACIA members, support staff and peers for their input, collaboration, as well as their friendship. Finally, I would like to thank my parents for their support and encouragement in this endeavor.

TABLE OF CONTENTS

- 1 INTRODUCTION 1
 - 1.1 Objectives 3
 - 1.2 Organization 3

- 2 BACKGROUND 5
 - 2.1 Power Transmission Systems 5
 - 2.1.1 Transmission Lines 5
 - 2.1.2 Challenges Faced by Transmission Utilities 7
 - 2.1.3 Weather Impact 9
 - 2.1.3.1 Atmospheric Icing 10
 - 2.1.3.2 Line Thermal State 15
 - 2.1.4 Line Rating 19
 - 2.1.5 Existing DTCR Technology 21
 - 2.2 Computational Intelligence 24
 - 2.2.1 Fuzzy Logic 24
 - 2.2.2 Evolutionary Computing 26
 - 2.2.3 Path Search Algorithms 29

- 3 ICE ACCRETION FORECASTING 32
 - 3.1 P-Type Classification 33
 - 3.2 Ice Accretion Model 36

3.3	Evolutionary Optimization of Model Parameters	41
3.3.1	Data Description	41
3.3.2	Optimization of Ice Accretion Model Engagement Function	48
3.3.2.1	GA Implementation	48
3.3.2.2	Development of the Forecasting System	53
3.3.2.3	Optimization of the Forecasting System	61
3.3.2.4	Evaluation of the Forecasting System	68
3.4	Application	69
3.4.1	Newfoundland 2010 Ice Storm Event	70
3.4.1.1	Ice Storm Description	70
3.4.1.2	NWP Model Setup	71
3.4.2	Evaluation	72
3.5	Summary	86
4	DYNAMIC THERMAL RATING	88
4.1	Precipitation Cooling of Overhead Conductors	88
4.1.1	Enhanced Dynamic Thermal Model	89
4.1.2	Available Measurements	98
4.1.2.1	Conductor	98
4.1.2.2	Sensor Instruments	98
4.1.2.3	Preprocessing	99
4.1.3	Evaluation	104
4.1.3.1	Results	104
4.1.3.2	Discussion	108
4.2	Optimal DTCR Configuration	113

4.2.1	Sampling Interval Data	114
4.2.2	DTCR Simulation	118
4.2.3	Analysis	120
4.2.4	Time Resolution Effects on Transient Conductor Temperature	122
4.2.5	Time Resolution Effects on Ampacity	122
4.3	Accuracy of DTCR Forecasts	128
4.3.1	Forecast Simulation Setup	129
4.3.2	Evaluation	131
4.4	Applications of DTCR Technology	141
4.4.1	Optimal Routing of Power Transmission Lines	142
4.4.1.1	Approach	143
4.4.1.2	Case Study	145
4.4.1.3	Analysis	147
4.4.2	Identifying Line Segments for Upgrading	151
4.4.2.1	Approach	152
4.4.2.2	Optimization Function	155
4.4.2.3	Case Study	158
4.4.2.4	Analysis	161
4.4.3	Reduction of Power Generation Emissions by Using DTCR ¹⁶⁹	
4.4.3.1	Power Generation Emissions	169
4.4.3.2	Case Study	171
4.4.3.3	Reduction in Emissions	180
4.4.3.4	Analysis	180
4.5	Summary	182

TABLE OF CONTENTS

5 CONCLUSIONS 186

5.1 Contributions 186

5.2 Significance 188

5.3 Future Work 190

BIBLIOGRAPHY 194

A WRF PARAMETERIZATION 204

B CONDUCTOR PARAMETERS 206

LIST OF TABLES

Table 1	Description of storms used for development of the IAFS system.	44
Table 2	Radial equivalent ice thickness determined by ASOS sensors, the difference of ice thickness modelled using CRREL and SM with observed meteorological input and using IAFS with hand-tuned and GA optimized parameters for the December 2002 ice storm.	46
Table 3	Accuracy of WRF predictions with respect to observations of meteorological variables used by accretion models.	47
Table 4	GA parameters used in the IAFS optimization process.	52
Table 5	Sum of the radial equivalent thicknesses for all 20 ASOS stations, and errors relative to the ASOS sensor output for the December 2002 ice storm.	55
Table 6	Error statistics of IFAS-GA for five testing storms.	61
Table 7	The optimal parameters of the engagement function discovered using the GA optimization process for each considered ice storm during a 10-fold cross-validation session.	63

Table 8	Error statistics of IAFS-5GA for the training set, testing set and all considered stations, and averages of the error statistics for top ten parameters from the random sub-sampling cross-validation session using all five ice storm events (5GA).	66
Table 9	Error statistics of IAFS-5GA for each of the five considered ice storms.	66
Table 10	Error statistics of IAFS-5GA for each of the three ice storms used for testing.	68
Table 11	Icing forecast skill of various IAFS in terms of total error compared to SM with a simple Ramer-like engagement function.	69
Table 12	Daily total precipitation observed on March 5, 2010, and simulated total precipitation for the same period. .	73
Table 13	Daily total precipitation observed on March 6, 2010, and simulated total precipitation for the same period. .	73
Table 14	Conductor specifications used in the precipitation based conductor cooling study.	99
Table 15	Description of the Artech SMT sensor unit installed at the Indian Arm crossing.	99
Table 16	Description of sensors installed at the Indian Arm crossing.	101
Table 17	MAE, ME, and RMSE of the line thermal model with and without the precipitation cooling extension.	105

Table 18	Statistics of conductor temperatures calculated using averaged and instantaneous values, compared to 1 min series.	120
Table 19	Mean Absolute Percentage Error (MAPE) of calculated ampacities compared to 1 min averaged series, and the 95 th and 99 th percentiles of the corresponding differences.	125
Table 20	Operating characteristics of the hypothetical transmission line placed using the line routing system.	149
Table 21	Conductor indices used in the intelligent line upgrade segment selection system.	160
Table 22	Assumed transmission line upgrading costs used in the line upgrading GA fitness function.	160
Table 23	GA parameters used for the presented line upgrading study.	160
Table 24	Increase in the NLH TL-201 transmission line capacity after a suggested line upgrade.	162
Table 25	Increase in the given AB transmission line capacity after a suggested line upgrade.	162
Table 26	Increase in the BC Hydro transmission line 5L011 capacity after a suggested line upgrade.	166
Table 27	Average GHG emissions released by electric power generation technologies over the plant life cycle.	170
Table 28	Major pollutants released by coal-fired power plants per kWh during power generation.	171
Table 29	Reduction in GHG emissions gained by using DTCR systems.	181

Table 30	WRF configuration for the IAFS GA optimization study. .	205
Table 31	WRF configuration for the Newfoundland 2010 ice storm event forecast.	205
Table 32	WRF configuration for the NWP DTCR verification study.	205
Table 33	WRF configuration for the optimal transmission line routing study.	205
Table 34	Conductor specifications obtained from manufactur- ers' data-sheets.	206

LIST OF FIGURES

Figure 1	A plot of the IAFS engagement function with respect to wet-bulb temperature and fraction of frozen precipitation.	40
Figure 2	Total precipitation for December 3-5, 2002 as hindcast by the WRF model.	43
Figure 3	Distribution of the calculated engagement function parameters obtained by the GA using the December 2002 ice storm.	54
Figure 4	Comparison of icing model accuracy for December 2002 storm with respect to observations from 20 ASOS stations.	56
Figure 5	Plot of observed vs. hindcast radial equivalent ice thickness for the December 2002 ice storm.	57
Figure 6	Observed precipitation type as a function of I_f and T_w	59
Figure 7	Distribution of the wet bulb temperature and the fraction of frozen precipitation for the five ice storms used for cross-validation training of IAFS-5GA.	64
Figure 8	Distribution of the calculated parameters of the engagement function discovered using the five ice storms for cross-validation training of IAFS-5GA.	65

Figure 9	Plot of observed vs. hindcast radial equivalent ice thickness for all five events using the winning parameters based on all five ice storm events.	67
Figure 10	The inner domain of the WRF model and the main power distribution line on the Bonavista peninsula. . .	74
Figure 11	Total precipitation for the March 2010 ice storm event as simulated starting on March 5 0:00 UTC. . . .	75
Figure 12	Cumulative observed 6-hour total precipitation amounts at Bonavista and corresponding total precipitation simulated by WRF.	76
Figure 13	Observed surface air temperature at Bonavista and temperature modelled with WRF.	77
Figure 14	Fraction of frozen precipitation on March 6 0:00 UTC as simulated on March 5 0:00 UTC.	78
Figure 15	Cumulative radial equivalent ice thickness from March 5 0:00 UTC to March 8 0:00 UTC, as calculated with the optimized Ice Accretion Forecast System (IAFS) algorithm.	79
Figure 16	Radial equivalent ice thickness accumulation over 19 mm, overlaid on a map of Newfoundland municipalities. . .	80
Figure 17	Radial equivalent ice thickness accumulated on the Bonavista power line over the entire March 2010 event.	81
Figure 18	Radial equivalent ice thickness accumulated at the most exposed point on the Bonavista power line.	82
Figure 19	FTS Meteorological Station installed at the BC Indian Arm crossing transmission line.	100

Figure 20	Arteche SMT sensor unit clamped onto the BC Indian Arm crossing transmission line.	102
Figure 21	Observed cumulative precipitation and precipitation rate before and after smoothing.	103
Figure 22	Observed and modelled conductor temperature for the Indian Arm Crossing transmission line, for the period between August 31 and September 1, 2010.	106
Figure 23	Observed and modelled conductor temperature for the Indian Arm Crossing transmission line, for the period between September 18 and 19, 2010.	107
Figure 24	Observed and modelled conductor temperature for the Indian Arm Crossing transmission line, for September 26, 2010.	107
Figure 25	Observed and modelled conductor temperature using the precipitation cooling model, for all data samples with non-zero precipitation rate.	108
Figure 26	Increase in computed line capacity, as estimated using the precipitation cooling extension.	109
Figure 27	Increase in computed line capacity, as estimated using the precipitation cooling extension.	109
Figure 28	Indian Arm Crossing estimated transmission line ampacity.	110
Figure 29	Normalized frequency distribution of the data used in the sampling interval study.	115
Figure 30	A view of the meteorological mast at Dlouha Louka. . .	116

Figure 31	Sample of the 1 min averaged wind time series used in this study (June 19, 1999).	117
Figure 32	Example of transient conductor temperatures, computed by the thermal model for the Finch conductor, and driven by instantaneous and averaged inputs.	121
Figure 33	Spectral density, normalized with frequency, of time series of wind speed and conductor temperature.	123
Figure 34	Cumulative frequency distribution of the conductor temperature, calculated with various average and update periods for the Finch conductor.	126
Figure 35	Distribution of differences in ampacity between 1 min updated-and-averaged time series and those with longer update periods for the Finch conductor.	127
Figure 36	NWP DTCR ampacity error statistics (Mean Absolute Error (MAE) & Root Mean Square Error (RMSE)) with respect to the forecast horizon.	131
Figure 37	A sample NWP-based DTCR ampacity time series output for the BC Indian Arm crossing transmission line.	132
Figure 38	Average conductor temperature for all forecast ampacities with respect to the forecast horizon.	132
Figure 39	Mean Error (ME) of for the NWP-based ampacity forecast with respect to the forecast horizon.	133
Figure 40	Pred(25) indicator of NWP forecast ampacity accuracy with respect to the forecast horizon.	134
Figure 41	A temperature histogram for the BC Hydro Indian Arm Crossing transmission line for a 0–6 hr forecast horizon.	135

Figure 42	A temperature histogram for the BC Hydro Indian Arm Crossing transmission line for a 6–12 hr forecast horizon.	135
Figure 43	A temperature histogram for the BC Hydro Indian Arm Crossing transmission line for a 12–24 hr forecast horizon.	136
Figure 44	A temperature histogram for the BC Hydro Indian Arm Crossing transmission line for a 24–48 hr forecast horizon.	136
Figure 45	A temperature histogram for the BC Hydro Indian Arm Crossing transmission line for a 48–84 hr forecast horizon.	137
Figure 46	A CDF of conductor temperature calculated using the FTS weather observations and line current based on the forecast line ampacity.	138
Figure 47	A CDF of conductor temperature using only 75% of forecast line ampacity.	139
Figure 48	Average ampacity deviation for each of the four possible conductor orientations across the considered region.	147
Figure 49	The power transmission line routing discovered by the intelligent line routing system.	148
Figure 50	The NLH TL-201 transmission line used for the line upgrade system evaluation study.	163
Figure 51	The AB transmission line segment used for the line upgrade system evaluation study.	164
Figure 52	The BC Hydro 5L011 transmission line used for the line upgrade system evaluation study.	165

Figure 53	GA population fitness value trend for the ROI objective line upgrade system.	166
Figure 54	Simplified power transmission scenario used for the GHG reduction using DTCR study.	174
Figure 55	Power curve for the wind turbine model used in the GHG using DTCR reduction study.	175
Figure 56	Distribution of the ampacity gain at a given sample point during summer months.	176
Figure 57	Distribution of the ampacity gain at a given sample point during winter months.	177
Figure 58	Distribution of the amount of potential power generated by a single turbine for the Ponoka site.	178
Figure 59	Distribution of the amount of potential power generated by a single turbine for the Chigwell site.	178
Figure 60	Amount of potential power generated by a single turbine for the Ponoka site.	179
Figure 61	Amount of potential power generated by a single turbine for the Chigwell site.	179
Figure 62	Amount of current supplied and carried by the transmission lines with respect to the number of turbines and available line capacity.	180
Figure 63	Fraction of total generated energy carried by transmission line with respect to wind farm size.	182

LIST OF SYMBOLS

β	angle between wind direction and a plane perpendicular to the axis of conductor [°]
$\cos \varphi$	power factor
Γ	fuzzy engagement function
μ_f	dynamic viscosity of air [Pa·s]
ρ_f	density of air [$\text{kg}\cdot\text{m}^{-3}$]
ρ_i	density of ice accretion [$\text{kg}\cdot\text{m}^{-3}$]
ρ_w	density of water [$\text{kg}\cdot\text{m}^{-3}$]
τ	thermal time constant [s]
A	ampacity [A]
c_i	specific heat capacity of ice [$\text{J}\cdot\text{kg}^{-1}\cdot\text{K}^{-1}$]
C_p	heat capacity of conductor [$\text{J}\cdot\text{kg}^{-1}\cdot\text{K}^{-1}$]
c_p	specific heat of air at constant pressure [$\text{J}\cdot\text{kg}^{-1}\cdot\text{K}^{-1}$]
c_w	specific heat capacity of liquid water [$\text{J}\cdot\text{kg}^{-1}\cdot\text{K}^{-1}$]
D	conductor diameter [m]

d_s	conductor strand diameter [m]
e_a	saturation vapour pressure of water at air temperature [Pa]
e_c	saturation vapour pressure of water at conductor temperature [Pa]
e_s	saturation vapour pressure of water [Pa]
H	enthalpy of vapourization of water [$\text{J}\cdot\text{mol}^{-1}$]
h	heat transfer coefficient [$\text{W}\cdot\text{m}^{-2}\cdot\text{K}^{-1}$]
I	current [A]
I_f	final current [A]
I_f	fraction of frozen precipitation
I_i	initial current [A]
k	ratio of the molecular weights of water vapour and dry air
k_f	thermal conductivity of air [$\text{W}\cdot\text{m}^{-1}\cdot\text{K}^{-1}$]
K_{angle}	wind direction compensating factor
L_e	specific latent heat of evaporation of water [$\text{J}\cdot\text{kg}^{-1}$]
L_f	specific latent heat of fusion of water at 273.15 K [$\text{J}\cdot\text{kg}^{-1}$]
m	mass of conductor per unit length [$\text{kg}\cdot\text{m}^{-1}$]
m_a	mass flux rate of water striking conductor surface [$\text{kg}\cdot\text{s}^{-1}\cdot\text{m}^{-1}$]
m_c	actual mass flux of water evaporating from conductor surface [$\text{kg}\cdot\text{s}^{-1}\cdot\text{m}^{-1}$]
m_e	maximum possible evaporative mass flux of water [$\text{kg}\cdot\text{s}^{-1}\cdot\text{m}^{-1}$]

n_s	number of strands in the outer layer of a conductor
P	power [W]
p_a	atmospheric pressure [Pa]
P_c	conductor perimeter [m]
P_r	precipitation rate [mm·h ⁻¹]
q_c	convective heat loss rate per unit length [W·m ⁻¹]
q_e	evaporative heat loss rate per unit length [W·m ⁻¹]
q_j	Joule (resistive) heat gain rate per unit length [W·m ⁻¹]
q_r	thermal radiation heat loss rate per unit length [W·m ⁻¹]
q_s	heat gain rate from solar radiation per unit length [W·m ⁻¹]
R	universal gas constant [J·K ⁻¹ ·mol ⁻¹]
R_c	resistance of conductor per unit length [Ω ·m ⁻¹]
R_{eq}	radial equivalent ice thickness [mm]
RH	relative humidity [%]
t	time [s]
T_a	air temperature [K]
T_b	boiling point of water [K]
T_c	conductor temperature [K]
T_e	evaporation temperature of water [K]

List of Figures

T_f	final conductor temperature [K]
T_i	initial conductor temperature [K]
T_s	water surface temperature [K]
T_w	wet bulb temperature [K]
V	voltage [V]
V_w	wind speed [$\text{m}\cdot\text{s}^{-1}$]
W	energy [$\text{W}\cdot\text{s}^{-1}$]
w	airborne liquid water content [$\text{kg}\cdot\text{m}^{-3}$]

LIST OF ABBREVIATIONS

AACSR Aluminium Alloy Conductor Steel-Reinforced

ACSR Aluminium Conductor Steel-Reinforced

AE Absolute Error

AGL Above Ground Level

ASL Above Sea Level

ASOS Automated Surface Observing System

CDF Cumulative Distribution Function

CI Computational Intelligence

CORR Correlation Coefficient R

DTCR Dynamic Thermal Circuit Rating

EC Evolutionary Computing

GA Genetic Algorithm

GHG Green House Gases

GIS Geographic Information System

IAFS Ice Accretion Forecast System

LiDAR Light Detection And Ranging

MAE Mean Absolute Error

MAPE Mean Absolute Percentage Error

ME Mean Error

METAR MÉTéorologique Aviation Régulière

NAM North American Model

NARR North American Regional Reanalysis

NWP Numerical Weather Prediction

RMS Root Mean Square

RMSE Root Mean Square Error

ROI Return on Investment

SM Simple Model

WPS WRF Preprocessing System

WRF Weather Research & Forecasting

1

INTRODUCTION

Almost all aspects of human society are impacted by weather, from simple day-to-day chores to large-scale projects and endeavors. It plays a dual role in our world, both helping to sustain the life on our planet, and causing significant destruction to property and life.

Weather also impacts the stability of power generation, transmission and distribution infrastructure. It dictates how long the equipment can remain in operation in the field. It also governs the thermal state of the power lines, and thus plays a significant role in the operating conditions of the transmission conductors. This in turn determines how much power can be transmitted. It should be noted that meteorological conditions can change rapidly across a given span of line and over time. Hence, the impact of weather on the transmission infrastructure will vary from place to place, even along the same transmission line.

The day-to-day impact of weather on the transmission grid has been compounded by climate change taking place at a rapid pace over the last few decades [1], [2]. Consequently, society demands greener generation sources that have less of a burden on our planet. These sources include hydro, geothermal, wind and solar generation. Unfortunately, they are frequently only available in select, often remote locations. Existing transmission lines were not typically constructed to incorporate these distributed sources of en-

ergy. This has resulted in the need to either perform costly upgrades of the transmission network or to sacrifice some of the potential energy generation capacity.

Additionally, in many urban areas, transmission networks have not seen any major upgrades from their original construction. Thus, their capacity has not kept up with the population expansion and overall increase in demand for electrical energy. Vital capacity upgrades have been postponed, and only recently has the dwindling transmission capacity gained industry attention.

Upgrades and expansion of transmission lines are one of the most costly and time consuming endeavors that a transmission company can undertake. Numerous issues must be considered, regulations met and societal objections addressed. Planning is typically done by experts in the field who use their knowledge and experience to make the best choices given the limited set of relevant information available. This however, can lead to suboptimal planning decisions resulting from human bias, and lack of consideration of all the variables impacting the potential power transmission line.

To minimize short term line capacity problems, some transmission line operators have begun to employ Dynamic Thermal Circuit Rating (DTCR) systems to harness underutilized transmission capacity. Unfortunately, this approach typically requires the installation of expensive sensor networks spanning the entire transmission grid. This limits the widespread application of DTCR technology. Presently, utilities focus DTCR deployments to critical sections of their transmission infrastructure which have been identified as significant bottlenecks and the cost of DTCR equipment is justifiable.

1.1 OBJECTIVES

As weather plays an integral part in the operation of the transmission grid, it is imperative to quantitatively assess its actual impact. Having advanced knowledge of weather's effect on the grid enable operators and management to better plan grid construction and upgrades and make better day-to-day decisions.

Hence, the objective of the research work described in this thesis is to alleviate some of the current challenges faced by the power transmission industry which are caused by weather. This is accomplished by:

1. More accurately predicting ice storm events that may affect power transmission infrastructure
2. Better estimating the capacity of transmission lines by improving a model used in dynamic thermal rating
3. Providing weather-related decision support for transmission line construction, upgrading and expansion projects

1.2 ORGANIZATION

This thesis is organized into five chapters. Chapter 2 provides background on power transmission systems, current challenges faced by the transmission industry, and a survey of relevant literature. It also provides a brief summary of select Computational Intelligence (CI) methods that can be used to

solve some of the challenging problems affecting the power industry. Chapter 3 describes the optimization of an ice accretion forecasting system and its evaluation on several storms that affected transmission network equipment. Chapter 4 presents an enhanced thermal model for ampacity and temperature of transmission conductors, and a study on optimal configuration of the model. The chapter also evaluates the accuracy of using Numerical Weather Prediction (NWP) models to forecast line ampacity and illustrates how DTCR technologies can contribute to the reduction of power generation emissions by allowing to bring more green energy into the power grid, without upgrading existing transmission infrastructure. Finally, chapter 5 concludes this thesis, summarizes the main contributions, and provides suggestions for expanding upon the presented research work.

2 | BACKGROUND

This chapter provides a brief overview of power transmission systems. It describes important details about transmission infrastructure and the challenges faced by the transmission industry. A literature survey is distributed throughout this chapter, covering important topics related to these challenges, and methods that can be used to help solve some of the problems.

2.1 POWER TRANSMISSION SYSTEMS

2.1.1 Transmission Lines

Electric power generation is typically not constructed next to the consumer base; therefore, the power industry must use transmission systems to deliver electricity from generators to the consumers. These systems include many different components and their construction and operation requires knowledge from a diverse engineering base. A critical component of the transmission systems is the power lines that actually transmit electricity to customers.

Power transmission lines are usually constructed above ground. This form of construction suspends the conductors from towers or poles, commonly known as power pylons. The conductors are affixed to or suspended from

the structures by insulators, typically made out of glass or ceramic material. The conductors are usually composed of either aluminium or an aluminium alloy; they are frequently intertwined with steel cables for strength. While copper conductors are a superior choice, their cost and weight do not permit their use for substantial installations. Future transmission networks may see the deployment of conductors made of superconducting cables inside a jacket holding a cryogenic gas; however, this technology is still a few years to a few decades from widespread deployment.

The primary reason for the use of overhead power transmission lines, as opposed to buried, i.e. underground transmission lines, comes down to cost. It is significantly more cost effective to construct the transmission lines in an overhead manner as expensive high voltage insulation is not required, frequent cable splices do not need to be made, and the digging of trenches or tunnels across the country is avoided. Typically, small underground lines cost two to four times as much as above ground lines [3]. Large capacity lines, such as those used in 500 kV transmission, can cost eight to ten times as much. Additionally, given that the conductors are much closer together in underground transmission systems, stability challenges can arise from an increased reactive component. Furthermore, underground power lines are also susceptible to breakage due to excavations. Thus, underground cabling is reserved for cases where the construction of overhead transmission lines would not be otherwise possible. This includes densely urbanized areas, sensitive natural habitats, and other areas where overhead transmission lines would pose either a danger or be an undue burden on the surroundings.

While overhead transmission line construction is cheaper and easier to maintain, it does expose the conductors to the elements and society, which

can cause a significant impact on their operations. Weather phenomena such as icing, wind load and lightning strikes, directly cause a significant impact to the power transmission line, reducing its longevity and increasing the risk of service disruption. Furthermore, ambient weather conditions govern the thermal state of a conductor. Some conditions tend to increase the line's temperature, such as a high ambient air temperature, increased solar radiation on a clear day, or calm air; while others such as high wind speed, cold ambient air temperatures, and various forms of precipitation tend to cool the conductor.

2.1.2 Challenges Faced by Transmission Utilities

The electrical power industry is under increasing pressure to cope with an enlarging market demand for power [4], [5]; however, generation capacity upgrades, often in the form of new wind farms, are increasingly hampered by the lack of transmission capacity to bring the additional power to customers [6]. To compound the problem, infrastructure necessary to deliver power to the consumer base has not received significant upgrades in the last few decades.

Constructing new power lines is a time consuming and expensive process that faces significant political and social challenges [7]. The planning of power transmission line construction itself is a complex task. A given route must satisfy a number of different, often conflicting, constraints [8], caused by technical limitations and economic considerations. The location for construction of new power transmission lines has to be selected so that it

minimizes the impact on the environment, avoids disturbing protected parks and wildlife reserves, and address the concerns of neighbouring communities. At the same time, the routing has to ensure that a given expansion project falls within budget restrictions. Unfortunately, current planning procedures often do not take into consideration other aspects that play a critical role in the operability of power transmission networks. One of the most significant factors that is often neglected or not fully incorporated into the construction planning of new lines is the climatological variation that occurs across the different geographical regions through which a new power line would potentially pass. As a result, the potentially significant impact that weather phenomena have on the line operating characteristics is not taken into account.

While planners are able to access static climatological trends to assist in gauging the meteorological influence on the new lines, these do not fully take into account the actual operating conditions, particularly localized but recurring weather phenomena. Furthermore, the generality of climatological data and human bias tends to prevent the discovery of an optimal positioning.

Upgrading existing power transmission infrastructure also poses significant road blocks due to the expense of the upgrades and the need to bring the power lines off-line for reconductoring and/or other other necessary hardware upgrades.

In an ideal situation, power transmission networks would be regularly upgraded to meet the demands. However, this is not always possible because of the major financial costs to upgrade and deploy new transmission lines, increased government and environmental regulations such as laws aimed at

preserving the natural habitat, and public opposition commonly known as NIMBY (“not in my back yard”).

Increased global awareness of climate change, and the need to reduce human impact on the planet is exerting pressure on all segments of society to adopt cleaner and more sustainable technologies. Among other impacts, it is driving the power industry to incorporate more green energy sources into its production in order to minimize the emissions of Green House Gases (GHG) and other pollutants from power generation.

As a result, significant investments are being made to bring more green renewable energy sources onto the market. However, existing transmission infrastructure often does not have the capacity to incorporate the new generation sources. Unfortunately, green energy resources, such as hydro, geothermal and wind power, unlike many conventional sources of generation, are relatively immobile and must be harnessed where they are available. Often no immediate access to high capacity power transmission lines is available. As such, the power industry is not always capable of optimally incorporating these sources into the existing grid, without costly infrastructure upgrades and/or expansion projects.

2.1.3 Weather Impact

Weather plays a major role in the operability of electric power systems. Meteorological conditions impact power production and consumption patterns, the integrity of the power transmission infrastructure and the characteristics of transmission networks, including the actual capacity of the power lines [9].

Weather phenomena and indirect events attributed to weather that can cause transmission line failures and outages include: extreme winds, extreme ice loads, combined wind-on-ice loads, lightning strikes, conductor vibrations and galloping (high amplitude, low frequency resonant oscillations of power line conductors induced by wind [10]), avalanches, landslides and flooding [11]. Excessive icing on overhead transmission lines can be particularly expensive, resulting in repair costs of many millions of dollars [12].

2.1.3.1 *Atmospheric Icing*

The top three causes of damage to power transmission lines were identified by the International Council on Large Electric Systems (CIGRE) as wind, ice and combined wind-on-ice loads, in a study conducted to analyze failures occurring worldwide between 1991 and 1996. 87% of the total damage costs can be attributed to these types of events [11]. There are several ways in which accreted ice can damage transmission systems. Ice loads on overhead power line conductors can snap conductors and break the connecting insulators or their support structures; excess weight on nearby tree limbs may cause them to fall onto conductors; and ice accretions enlarge the exposed surface area and alter the conductor's profile, resulting in greater wind loads and possibly galloping [13].

A freezing rain ice storm is typically characterized by freezing precipitation known as glaze. A typical event usually brings at least half a centimetre of accumulated ice [14]. However, very severe icing events result in ice accumulations of over 10 cm. This weather phenomenon often forms when a warm layer of air is sandwiched between two layers of cold air near the surface. As the frozen precipitation falling from the upper cold layer moves through the

warm layer, it melts and then continues falling as liquid droplets. It then proceeds to fall through the lower cold air layer, where it becomes supercooled to temperatures below freezing. These liquid droplets freeze upon contact with any structure whose temperature is below freezing [15], forming a layer of ice.

Although icing events are rare, they can be very costly. Damage from freezing rain causes an annual property-related loss averaging \$313,000,000 in the USA alone [16]. An extreme example is the ice storm that occurred in early January 1998. This storm brought a prolonged freezing rain event to many parts of Quebec and Ontario in Canada, and to the North-Eastern United States, resulting in ice accumulations of up to 70 mm. This single storm caused the largest insured loss in Canada, estimated to be at \$1.44 billion [17]. As a result, 5.2 million people were without power in Canada and the USA, and there were 25 fatalities. Although the damage incurred by the freezing rain event could not have been prevented entirely, an early warning system would have allowed the population to be better prepared for this disaster. Additionally, a system built to predict potential transmission system damage would have allowed the operators of power transmission systems to take preventative or mitigating measures before the storm hit. These measures can include intentionally increasing current flowing through the conductors to raise their temperature sufficiently to prevent ice accretion [18] or having repair crews on standby to clear the ice once it forms on the conductors.

Steady progress has been made in modelling ice accretion over the past few decades. Numerous ice accretion algorithms [19], [20], [21], [22], [23] have been developed by researchers. They work by modelling the accretion of supercooled water droplets onto structures. Some of these ice accretion

models, e.g. the morphogenetic or random walk scheme [24], are more suited for detailed icing studies rather than for operational use.

Diagnostic models are usually based on the mass flux of water droplets reaching the surface of the icing object and the efficiency of the accretion process [25]. Modelling freezing rain accretion using these models involves the adoption of several simplifying assumptions that make their operational use less computationally demanding. First, freezing raindrops are assumed to be large enough so that their collision efficiency can be considered unity. Second, the wind is assumed to be perpendicular to the line, which is generally considered to produce the highest ice loads. Third, the accretion is assumed to be a circular cylinder. Thin ice accretions on overhead power line conductors are quasi-circular, as are large ice accretions on torsionally weak conductors. However, when the ice accretion is dry and the conductor is torsionally stiff, the ice forms on the upper, windward side, giving rise to a quasi-elliptical shape. At air temperatures within a few degrees of freezing, icicles tend to form. Because icicles intercept additional droplets and provide an opportunity for unfrozen surface liquid to freeze instead of being shed, ice loads with icicles can exceed those computed with a simple, cylindrical model. Fourth, melting is ignored. Simple models making these assumptions are sufficient for freezing rain simulation, as long as the ice growth remains in the dry regime [22]. Using all these assumptions, a simple model can be formulated to calculate the radial equivalent ice accretion thickness on a cylinder, which does not depend on the original size of the object [23].

Unfortunately, many of the more complex icing model implementations are not suitable for on-line use in operational forecasts. This is due to the fact that they require detailed knowledge about the state of the liquid in the

atmosphere, such as the distribution of droplet size. Such information is not readily available from a Numerical Weather Prediction model that would be employed in forecasting the state of the atmosphere. Other models require computationally intensive numerical methods that make them unsuitable for cost-effective implementation for forecasting ice accretion over a large area.

In order to forecast ice accretion due to freezing rain, future values of meteorological variables pertinent to glaze ice accretion must be known, including the freezing rain precipitation rate, wind velocity and air temperature. These values can be forecast (or simulated) with a NWP model. However, NWP models do not typically directly output the freezing rain precipitation rate. Consequently, it must be computed in a post-processing step.

The idea of combining a NWP model with an icing model was suggested more than a decade ago [26]. Due to the advanced microphysics schemes invoked in the model, the problem generally requires a fine spatial resolution, resulting in high computational costs. However, the rapid development of computer power during the last decade has made it possible to combine NWP and icing models, while the accuracy of NWP systems has significantly improved [27]. NWP models were recently used to predict rime icing events in mountainous regions [28]. A NWP model, coupled with a universal mass-based icing scheme that resolves both rime and glaze icing was applied in northeast Bulgaria [29].

For operational glaze ice accretion forecasting, the Simple Model (SM) [23] is well suited. It has already been employed in analyzing the ice accretion for past ice storms such as the 2002 ice storm [30]. Furthermore, because of its computational simplicity, it can be efficiently run for a large spatial area. Additionally, due to its similarity to the Goodwin model, which was

recommended by [22], it is an ideal candidate for an operational icing hazard forecast system. The basic principle of SM consists of taking a vector sum of the falling and windblown rain flux and then calculating the thickness of the growth of a uniform ice structure around a cylinder.

To actually forecast the amount of ice accreted on a structure using NWP in a real-world event, the freezing rain model must first determine whether the falling precipitation is in the form of freezing precipitation. Numerous precipitation type algorithms have been published [31], [32], [33]. To make a distinction between the different forms of precipitation, precipitation type algorithms frequently make use of wet bulb temperature for the diagnostic calculations. In particular, the Ramer [33] algorithm determines the precipitation type using a series of calculations based on the wet bulb temperature, pressure, and relative humidity sampled throughout an entire vertical profile above a given location of interest. It then diagnoses the precipitation type as either snow, freezing rain, ice pellets, rain or a combination thereof, using a series of rules that depend on the value of the input variables.

For operational use by power utilities, there have been only a few systems proposed that can provide automated forecasting of ice accretion [34], [35]. One of the most promising systems is the Ice Accretion Forecast System (IAFS) [35]. It is based on a NWP model combined with a precipitation type classifier and an ice accretion model. IAFS improves upon SM's accuracy by using an engagement function to determine during which conditions to employ the SM to accumulate ice and to what degree. The parameters of this function were determined based on the analysis of a well-documented, large-scale icing event.

2.1.3.2 *Line Thermal State*

The amount of power that can be sent through a transmission line is largely limited by the conductor's maximum operating temperature. This maximum temperature limit is selected to ensure that safety regulations are met, line clearances satisfied and to minimize the loss of tensile strength of the conductor [36]. To avoid these problems, the maximum current rating, ampacity, is calculated in terms of the maximum current it can safely transport without a substantial risk of thermal overload.

A line thermal model is used to estimate the maximum current rating from known or assumed operating conditions. The same model can be used to calculate the operating line temperature from a known current flowing through the conductor.

Currently, there are two commonly accepted methodologies used to calculate the current or temperature of overhead conductors. These are the IEEE standard [37] and the CIGRE method [38]. These two approaches were compared in a study which found no significant differences in their performance [39].

Both computations rely on solving a heat balance equation that accounts for the energy gained by the conductor through internal and external heating processes, and the energy lost into the environment. To compute the energy gains and losses, one must know the physical properties of the conductor, the operating conditions of the conductor, and the surrounding ambient conditions.

The thermal model adopted by the power transmission industry in North America [37] is based on the formulation provided by House and Tuttle [40].

It includes all essential factors in the thermal heat balance of the conductor. Previous formulations have neglected some of the terms present in the currently accepted model for simplicity. The formulation was later modified by ECAR [41] to address the discontinuity between laminar and turbulent airflow.

For steady-state conditions, when the line loading characteristics have remained constant for a sufficiently long period of time, the heat balance equation takes the form

$$q_c + q_r = q_s + q_j. \quad (1)$$

Equation 1 balances the heat lost to the environment due to natural or forced convection q_c and thermal radiation q_r against the heat gained from solar radiation q_s and the resistive heating of the conductor q_j . For negligible wind speed, only natural convection is considered in the calculation of q_c . The units of all heat terms in Equation 1 are $[\text{W}\cdot\text{m}^{-1}]$. The resistive heating component depends on the current flowing through the conductor I [A] and the resistance of the line R [Ω] at the conductor's temperature T_c [K],

$$q_j = I^2 R_c (T_c). \quad (2)$$

In the case of a sudden change in the current, the heat balance equation can be modified to incorporate the heat capacity C_p [$\text{J}\cdot\text{kg}^{-1}\cdot\text{K}^{-1}$] of the conduc-

tor's mass m [$\text{kg}\cdot\text{m}^{-1}$], in order to account for changes in its thermodynamic internal energy

$$q_c + q_r + mC_p \frac{dT_c}{dt} = q_s + q_j. \quad (3)$$

The fundamental principle for finding the line current or line temperature, is based on the hypothesis that the energy gained by the line must be equal to energy lost by the line. Thus, it is possible to solve the equation for the unknown temperature, if the current and environmental variables are known, or for the line current at a known line temperature.

Other heat balance equations exist in the literature. To allow for an algebraic solution to the heat balance equation for both the line temperature at a given current and vice-versa, the radiative heat component can be approximated by a linearization of the radiation cooling term [42], [43], [44], and solved as a standard linear differential equation. These linearized formulations are more computationally efficient; however, the resulting mathematical solutions are far more complex. An alternative approach to solving the heat balance can be implemented by representing it as a biquadratic equation, and then solving it for the line temperature [45], [46].

The ampacity of a conductor can be calculated for steady-state conditions, under the assumption that the conductor temperature has already reached equilibrium and the derivative dT_c/dt is set to zero. The remaining equation can be solved for I using a specified function for $R(T_c)$, with T_c set to the maximum safe conductor temperature.

To obtain an ampacity rating for the entire transmission line or a line segment, the conductor's ampacity must be calculated at regular intervals along the line and then the minimum current taken

$$A(t) = \min_i A_i(t), \quad (4)$$

where A is the line ampacity in Amperes, and A_i is the current rating of the conductor at a given point i at time t .

Under varying current and/or ambient conditions, the conductor temperature should be calculated as transient, keeping the derivative dT_c/dt at its actual value. The heat balance equation then needs to be solved numerically at each time step. The transient thermal rating is calculated with respect to a specific time period.

For transient calculations, a thermal time constant for the conductor can be defined. This constant represents the time required for the conductor's temperature to reach 63% of the difference between its initial value and the steady-state value, following a change in current and/or ambient conditions. To reach the steady-state temperature requires, in principle, an infinite time. For a step current change, the thermal time constant can be expressed as

$$\tau = \frac{(T_f - T_i) m C_p}{R(T_c) (I_f^2 - I_i^2)}, \quad (5)$$

where T_i and T_f are the initial and final conductor temperature respectively, and I_i and I_f are the initial and final current, respectively. The initial and final

temperatures are calculated for a wind speed of $0.6 \text{ m}\cdot\text{s}^{-1}$, which corresponds to the standard near-worst-case scenario used by power transmission utilities to rate overhead conductors. Typical values of the thermal time constant for overhead lines lie between 5 and 15 minutes.

The actual amount of electric power that can be transmitted over the lines is calculated by

$$P = \sqrt{3} \cdot A \cdot V \cdot \cos \varphi, \quad (6)$$

where A is the line ampacity, V is the transmission line voltage, and $\cos \varphi$ is the power factor. Power factor is the ratio between active power or real power transmitted to electrical loads and apparent power, which is the product of the Root Mean Square (RMS) voltage and RMS current.

The amount of transmitted energy is calculated as

$$W = P(t) \cdot t, \quad (7)$$

where t is the time period.

2.1.4 Line Rating

As described in the previous section, the limitation of the transmission line current is largely determined by the maximum operating temperature of its conductors and other associated hardware.

There are two main approaches used for thermal rating of power transmission conductors. Static rating [47] assumes a conservative scenario for calculating the steady-state ampacity: high ambient temperature, low wind speed, and high solar radiation. These values can be chosen either arbitrarily or probabilistically. In the case of an arbitrary choice, the values are selected such that their occurrence is almost impossible (also known as the near-worst-case scenario). In the probabilistic case, the values are chosen as quantiles of known distributions of collected historical data. The levels of quantiles depend on acceptable risk tolerance, usually in the range of 2-5%. However, even such conservative ratings may not suffice under true worst-case conditions (e.g. extreme ambient temperatures combined with full solar radiation and no wind). Under such conditions, the actual ampacity may be lower than the static rating, leading to an inadvertent thermal overload of the conductor. This can happen with a probability of few percent, depending on the rating assumptions and climate of the site.

Typically, ampacity values are calculated such that the current in the conductor would cause its temperature to reach, but not exceed, 75°C . This threshold provides a sufficient safety margin from the temperatures that could cause irreversible degradation of a typical ACSR conductor. This value is usually quoted in conductor data-sheets [48] and it is often used for static rating [49], [45]. However, there is no industrial standard or consensus for setting the maximum allowable temperature [50]. As a result, utilities are essentially free to select their own line rating conditions, based on the principle that the asset owners are responsible for the reliability and safety of their facilities [51].

2.1.5 Existing DTCR Technology

Transmission companies are seeking alternatives to expand the capacity available with the existing infrastructure. One modern approach is to use DTCR systems to identify any surplus transmission capacity and make use of existing, underutilized power lines [52].

DTCR systems [53], [54] are capable of increasing the capacity of existing power transmission lines by dynamically rating them in real time. The dynamic rating of transmission lines represents a significant improvement over the more traditional static rating. This is because DTCR uses actual operating conditions, rather than assumed conservative conditions or historical averages [55].

On average, DTCR systems provide electric power utility operators with real-time ampacity ratings that, under typical mid-latitude climatic conditions, are on average twice the static ampacity at a given point [56]. However, it is important to keep in mind that the amount of current that can be passed through an entire line span is limited by a single point along the line having the lowest ampacity. This can potentially put a severe limitation on the net gain that can be achieved through the utilization of DTCR technology.

As such, DTCR systems provide the power transmission industry with a more cost-effective approach to expand available transmission capacity [57]. Furthermore, DTCR systems can decrease the time for new power generation sources to deliver energy to markets, since DTCR installations can be deployed relatively quickly and do not require new infrastructure construction.

A system that involves DTCR and on-line monitoring was proposed by Douglas [55]. In this system, weather data were recorded every 2–5 minutes and

a short-term, emergency ampacity rating was evaluated every 5–60 minutes. The weather parameters that are usually measured for DTCR purposes include ambient air temperature, wind speed and direction, and solar radiation; the latter can be easily calculated for clear-sky days, if measurements are not available. In some cases, the conductor temperature is also measured. Bohme [58] suggests that the observation interval for DTCR purposes should be of the same order as the expected thermal time constant. This is around 3 minutes for a wind speed of $5 \text{ m}\cdot\text{s}^{-1}$, and 17 minutes for no wind. These values depend on conductor diameter.

To survey the operating conditions, modern DTCR systems usually monitor conductor temperature, sag, and/or weather conditions. The measured data are then used to calculate the additional line capacity available for power transmission. This information can be used to increase the normal and emergency operating flexibility of power transmission systems. As conductor temperature varies in time and space [59], ampacity cannot be exactly determined but only estimated. By their very nature, DTCR systems are associated with a risk that the estimated ampacity is higher than its actual value. Analysis of this risk depends on the particular type of DTCR system.

Currently, the electric power industry is capable of operationally determining the thermal state of a line by employing one of several technologies available on the market or under active research, each with varying strengths and weaknesses.

The ThermalRateTM DTCR system [60] uses two simulated conductor sections to assess the environmental impact on the conductor. It does this by exposing two cylindrical elements profiled like the power line conductor and laden with sensors. One section is heated by a constant wattage, while the

other remains unheated. Using the temperature difference between the two sections, the effect of the ambient weather conditions is thus assessed and the conductor ampacity is determined.

An alternative device present on the market is the Power DonutTM. It clamps directly onto the power line to measure the line temperature and passing current. This eliminates the guesswork in determining the actual conductor temperature, but it does not measure the ambient environmental conditions necessary for accurate ampacity calculations.

Another competing product is the SagometerTM. It uses an optical instrument composed of a laser and a target to measure the sag of a given line from a base reading, and from this, estimates the line temperature.

It should be noted that all sensor-based installations require that a communication network be in place, whether in the form of satellite, radio, internet connectivity or a dedicated fiber optical installation. Furthermore, numerous sensors need to be installed to accurately assess the actual line ampacity, and the resulting cost can be significant.

Alternatively, indirect methods of determining the line temperature or ampacity can be employed. These can solve for the thermal state of the power lines using local meteorological reports or forecasts [61] and statistics [62]. However, given potential variations in the weather conditions over a short spatial span, the estimates may not provide reliable accuracy for all the sections of the transmission line.

Currently, identifying bottlenecks in a transmission line, that can hamper the use of DTCR equipment, requires physical monitoring of a transmission line under load. This can be accomplished by using high resolution sensory equipment such as LiDAR [63]. Unfortunately, such methods are time

consuming and expensive, and they are unable to capture the operating characteristics of a given transmission line over an extended period of time under varying weather conditions.

2.2 COMPUTATIONAL INTELLIGENCE

To solve many complex real-world problems, scientists and engineers can employ CI techniques to assist them in finding a solution. This group of methods belong to a class of artificial intelligence algorithms that are typically heuristic in nature. They draw inspiration from human methods of problem solving, as opposed to classical artificial intelligence which are strongly rooted in mathematical principles. Many CI algorithms rely on agents that incorporate some form of artificial intelligence, modelled or inspired by real-world counterparts. Often, simulations using the agents in a representation of the problem space are performed to find the solution.

2.2.1 Fuzzy Logic

Fuzzy logic [64], [65] was originally introduced by Zadeh [66] in the middle of the 20th century as a way to represent imprecise human knowledge in a more formal mathematical way. Classical boolean logic deals with absolutes. However, in the real world, not everything can be quantified in such a manner. Many concepts have degrees of truthfulness and degrees of belongingness to different sets. Furthermore, humans usually use general and

approximate expressions of information on a daily basis as opposed to using precise quantities. As such, it is difficult to map the vague information into classical mathematical formulations. Using concepts of fuzzy logic, powerful expressions can be formulated in a human-centric fashion that capture real-world conditions or processes [67].

To accommodate qualitative knowledge, fuzzy logic utilizes the notion of fuzzy membership functions. This allows a specific instance or element, x , from a domain, termed the universe of discourse of X , to have a range of possible membership to a particular set, A , between 0 and 1. Thus, when the belongingness or membership is given as 0, x is completely excluded from the set A and when the membership is 1, it is completely included in A .

$$\mu_A(x) : X \rightarrow [0, 1], \quad (8)$$

where $\mu_A(x)$ is the membership function of the fuzzy set A , in the universe of X .

The real advantage of fuzzy membership functions comes from the range of values in between 0 and 1. This allows an element to have a partial membership to a set. Furthermore, by having multiple memberships to various sets, a smoother transition between belonging and not belonging to a given class can be made. This permits the definition of real-world groupings, where human concepts often do not have hard boundaries.

It is important to note that the fuzzy membership functions should be defined so that they suitably capture the underlying concept or phenomenon. They must reflect the actual problem, the amount of detail available, and the

context in which they are used. To ensure that the membership of a particular element in a set is bounded, the functions must also be bounded. The membership function should also have at least one point in the universe of discourse with full membership, i.e. be *normal*, and also not be multimodal to properly represent the meaning of the membership to a set. Typical examples of mathematical functions used for the membership functions include the linear, delta, triangular, trapezoidal, gamma, *s*-membership, gaussian and exponential functions [68]. The selection of the function allows the designer to describe for which regions a complete membership exists, known as the core, and for which a fuzzy or uncertain membership exists.

The different operators such as AND, OR, NOT, union and intersection are defined in fuzzy logic through appropriate mathematical operators that meet specific criteria. This allows one to use fuzzy logic in normal boolean algebra equations. Subsequently, real-world rules and relationships can be defined in a more natural and user intuitive manner. Fuzzy sets also intrinsically incorporate concepts of uncertainties in a given problem domain, using the partial membership of an element to one or more sets. This gives the ability to obtain a “possibility” and “confidence” of a given axiom being true.

2.2.2 Evolutionary Computing

Many engineering problems rely on finding optimal solutions to mathematical formulations, often governing some physical processes. Engineers and scientists use their own knowledge and experience to derive a solution. However, this approach may not provide the best solution and it may be biased

by preconceived notions of how the problem should be solved. While many mathematical techniques exist to solve for a global optimum, they require intimate knowledge of the characteristics of the system; however, often this is not available. The field of Evolutionary Computing provides strategies for solving optimization problems, such as selecting parameters and learning optimal functions, without the need for an exact mathematical representation of the problem space. Rather, they use feedback from the environment to assess the performance of a solution, and use this information to generate and modify solutions.

The Genetic Algorithm (GA) [69], [70], [71] relies on simplified models of evolutionary biology, which include operations of selection, crossover and mutation, and hereditary inheritance. GAs encode candidate solutions as chromosomes composed of a set of genes that are distinct components to the solutions. Multiple individuals are maintained in a potential solution pool called a population. Genetic operators are applied on the population to facilitate an iterative refinement of the solution to the optimization problem.

The GA search process is organized in four major steps. The first step is the system initialization, where a new population is created based on a desired distribution, which can be random or composed of seeds taken from a set of potential candidate solutions. This provides the initial solution to the optimization problem.

The second step is used to determine which candidates continue to the next generation and which will be removed. This is based on a fitness function used to evaluate the performance of each candidate solution. The surviving individuals are usually chosen by a stochastic mechanism such as fitness-proportional, rank or tournament selection. Multiple copies of the same indi-

vidual are permitted, as these clones may be modified in the next step, thus providing the same starting point for multiple alternative search directions.

In the third step, the selected candidates are used to form a new pool of individuals. Some individuals may be carried forward into the new population directly. However, the majority of individuals are manipulated by genetic operations. The crossover operation takes two individuals and recombines their genes through swapping, resulting in two new solutions. This mechanism allows existing solutions to be partially merged with the intention of finding a better combination of the two. Alternatively, the mutation operation randomly alters some of the individuals genes to introduce new candidate solutions into the population.

The final step is to check the termination condition. This usually involves computing the error of the discovered solution(s), such as that of the best individual. If the error is acceptable, has not been changing for a specified period of time, or the allocated computing time has expired, the GA process is terminated. Otherwise, the GA returns to the second step with the new population.

Functionally, the GA is a heuristic stochastic search of a given problem space, resembling the classical Hill Climbing search algorithm [72] with the addition of a crossover function. The additional operations incorporated into the GA provide mechanisms which, in many cases, offer substantial speedups and are very effective at escaping local minima.

In operation, GAs provide an effective search and optimization strategy that offers low cost, both in terms of implementation complexity and computational requirements, to solve many hard, real-world problems. Furthermore, because GAs rely on a cost/quality fitness function, an explicit formulation

is often not required. Black-box evaluation can be used to gauge the performance of the candidate solutions.

GAs are an efficient and powerful tool in solving parameter optimization problems [73], due to their ability to manipulate multiple parameters simultaneously. As described by [74], GAs can also be used on optimization problems with real-valued parameters. They do not require domain specific information in the implementation of the GA system, with the exception of the fitness function. Additionally, because solutions discovered are not subject to designer bias, they can generate solutions which may be counter-intuitive to a human expert, yet prove to work in real-world implementations. This occurs because they are not prevented from exploring a search space that a human would avoid due to personal preconceptions.

2.2.3 Path Search Algorithms

Another genre of optimization techniques contains algorithms and methods to solve combinatorial optimization problems, frequently described by graph structures. These include tasks such as discovering the shortest path in a graph, finding a minimum spanning tree, source-sink optimization, and so forth. Dynamic Programming can be used to solve these problems through a divide-and-conquer approach. The problem is partitioned and then incrementally solved. Intermediate values, such as weights, are either calculated and subsequently used in later subproblems, or the problem can be solved using a bottom-up approach recursively.

One of the most fundamental and well-known algorithm, designed to optimally solve a single-source shortest-path problem, is Dijkstra's algorithm [75]. Due to its greedy design, it is capable of finding a solution faster than other optimization methodologies, such as typical dynamic programming solutions. However, one major limitation of Dijkstra's algorithm is that it requires all edges in the graph structure to have non-negative weights. Thus, edge weights cannot be defined as both rewards and penalties simultaneously.

The basic operation of the algorithm is to successively reduce the distances (specified by the user) from the source node to the destination node. This is done by first setting a distance value of zero to the initial node and infinity to all the remaining nodes. The remaining nodes are also marked as unvisited at the same time. Starting from the source node, the unvisited neighbors' tentative distances are calculated back to the source node, and updated if the new distance is smaller than the previously recorded distance value. The next node is chosen based on the smallest distance from the source node. This process is iterated until the destination is reached. The list of nodes that were visited is the shortest path subject to the defined distance measure.

Dijkstra's algorithm is a key instrument in solving many real world problems that can be formulated into a task that involves finding a minimum distance from one point to another. Some prominent examples include road navigation tasks performed by GPS units, Internet packet routing protocols, and flow optimizations.

Listing 2.1: Pseudocode for Dijkstra's algorithm.

```

function Dijkstra(Graph, source):
  for each vertex  $v$  in Graph:
    distance[ $v$ ]  $\leftarrow \infty$ 
    previous[ $v$ ]  $\leftarrow$  undefined
  end for
  dist[source]  $\leftarrow$  0
  Q  $\leftarrow$  set of all nodes in the Graph
  while Q is not empty
     $u \leftarrow$  vertex in Q with smallest distance in distance[]
    if distance[ $u$ ] =  $\infty$ 
      break
    end if
    remove  $u$  from Q
    for each neighbor  $v$  of  $u$ :
      alt  $\leftarrow$  distance[ $u$ ] + distance-between( $u$ ,  $v$ )
      if alt < distance[ $v$ ]:
        distance[ $v$ ]  $\leftarrow$  alt
        previous[ $v$ ]  $\leftarrow u$ 
        decrease-key  $v$  in Q
      end if
    end for
  end while
  return distance[]

```

3

ICE ACCRETION FORECASTING

The ability to model and forecast accretion of ice on structures is very important for many industrial sectors. Studies conducted by the power transmission industry indicate that the majority of failures are caused by icing on overhead conductors and other components of power networks. As such, it would be very advantageous for the industry to have accurate advance knowledge of an impending event that could potentially put the infrastructure at risk.

To help the power transmission industry to accurately forecast ice storms, this chapter presents research work performed to develop an extension to a state-of-the-art ice accretion forecast system, IAFS. IAFS is comprised of an NWP model, a precipitation type algorithm, and an ice accretion model. To optimize the performance of IAFS, the parameters of the precipitation type algorithm are estimated using a GA. The improved system is trained by hindcasting a well-documented freezing rain event, and calibrated using four additional ice storms. Subsequently, the system is tested using three independent storms. The enhanced IAFS is tested in a true forecast configuration on a recent severe ice storm that hit the East coast of Canada in 2010 and caused extensive damage.

3.1 P-TYPE CLASSIFICATION

As the most prevalent form of ice accretion is caused by freezing rain, an effective method for forecasting precipitation type is required to determine when to engage the ice accretion model to compute the ice load. The algorithm currently used in IAFS is based on Ramer [33] because it is statistically the strongest of several algorithms [76] and it uses the fraction of frozen precipitation I_f .

Fraction of frozen precipitation is a dimensionless variable available in the standard Weather Research & Forecasting (WRF) output; it is defined as the ratio of frozen precipitation (in the form of ice, such as snow and ice pellets) and total precipitation. To distinguish between rain and freezing rain, air temperature and fraction of frozen precipitation can be used as described in [33].

To determine the precipitation type, the Ramer algorithm uses the wet bulb temperature, T_w [K], atmospheric pressure, p_a [Pa], and relative humidity, RH, throughout an entire vertical column above a location of interest. It then diagnoses the precipitation type as either snow, freezing rain, ice pellets, rain or a combination thereof, by performing the comparisons outlined below.

Wet bulb temperature, T_w , can be calculated from WRF output variables by using an empirical formulation [77], or by solving the following psychrometric equation

$$e_s(T_d) - e_s(T_w) = \frac{-c_p \cdot p_a}{k \cdot l_v} \cdot (T - T_w). \quad (9)$$

This is done by first rearranging the terms to solve for T_w

$$f(T_w) = 0 = T - T_w + [e_s(T_d) - e_s(T_w)] \cdot \frac{\epsilon \cdot l_v}{c_p \cdot P}. \quad (10)$$

Due to the recursive nature of this equation, where the value T_w is a function of itself, a numerical solving technique, such as Newton's method must be applied in order to solve for the actual wet bulb temperature. The differentiated recursive formula then provides

$$f'(T_w) = -1 - \frac{\epsilon \cdot l_v}{c_p \cdot P} [e'_s(T_w)], \quad (11)$$

where e_s is saturation vapour pressure as defined by [78]. After differentiation, this equation becomes

$$e'_s(T_w) = 0.6112 \cdot \exp\left(\frac{17.67 \cdot t}{t+243.5}\right) \cdot \left[\frac{17.67}{t+243.5} - \frac{17.67 \cdot t}{(t+243.5)^2} \right]. \quad (12)$$

As a result of employing Newton's method, the iterative formula takes the following form

$$T_w^n = T_w^{n-1} - \frac{f(T_w^{n-1})}{f'(T_w^{n-1})}. \quad (13)$$

Using this equation, T_w can be iteratively solved by using an initial guess for the wet bulb temperature, such as using the average of the ambient air

temperature and the dew point temperature, and then repeatedly solving the equation until the difference between two subsequent temperatures is less than some acceptable error.

The wet bulb temperature is then first compared against two temperature thresholds which separate out the simple cases for rain and snow.

Case 1: If $T_w > 2^\circ\text{C}$, then p-type = rain,

Case 2: If $T_w < -6.6^\circ\text{C}$, then p-type = snow.

Should the wet bulb temperature lie between these two thresholds, the Ramer algorithm seeks to determine the location of the precipitation generation layer. This is done by finding the highest saturated layer, at or below 400 mb, with $\text{RH} > 90\%$ extending over a depth of at least 16 mb. In this generation layer, the starting state of a hydrometeor is assumed to be either ice or supercooled water.

Case 3: If T_w in the generation layer $< -6.6^\circ\text{C}$ and $T_w < 0^\circ\text{C}$ for the entire vertical profile below the generation layer, p-type = snow.

In the final case, the hydrometeor is assumed to be supercooled in the generation layer. Additional comparisons are then performed to determine the hydrometeor's state when it falls to the ground, based on the the fraction of frozen precipitation, I_f .

Case 4: If T_w at the generation layer $\geq -6.6^\circ\text{C}$ or $T_w \geq 0^\circ\text{C}$ for at least one point in the vertical profile, then p-type is determined by the value of I_f .

Case 4a: $I_f > 0.85$, then p-type = ice pellets

Case 4b: $I_f = 1$, then p-type = snow

Case 4c: $I_f < 0.04$ and T_w at surface $< 0^\circ\text{C}$, then p-type = freezing rain

Case 4d: $I_f < 0.04$ and T_w at surface $> 0^\circ\text{C}$, then p-type = rain

Case 4e: $0.04 < I_f < 0.85$ and T_w at surface $< 0^\circ\text{C}$, then p-type = freezing mix

Case 4f: $0.04 < I_f < 0.85$ and T_w at surface $> 0^\circ\text{C}$, then p-type = frozen mix

3.2 ICE ACCRETION MODEL

When precipitation type is diagnosed to be freezing rain, a suitable ice accretion model is invoked (engaged) to predict the amount of ice that accumulates on a structure of interest. For this purpose, IAFS uses [23] SM, a numerical model that assumes that all falling precipitation forms a uniformly thick layer of ice. It determines the ice accretion load by calculating the radial equivalent ice thickness, R_{eq} , from the freezing rain precipitation rate and the wind speed. The model begins by first estimating the liquid water content in the air from the precipitation rate using [79]

$$w = 6.7 \times 10^{-5} P_r^{0.846}, \quad (14)$$

where P_r [$\text{mm}\cdot\text{h}^{-1}$] is the precipitation amount in the i th hour, and w_i [$\text{kg}\cdot\text{m}^{-3}$] is the airborne liquid water content for that hour.

Then, the amount of accumulated freezing rain is computed as the vector sum of the vertical flux of falling rain and the horizontal flux of windblown precipitation

$$R_{eq} = \sum_i \frac{1}{0.001\rho_i\pi} \sqrt{(0.001P_r \cdot \rho_w)^2 + (3600 \cdot V_w \cdot w)^2}, \quad (15)$$

where ρ_i [$\text{kg}\cdot\text{m}^{-3}$] is the density of the ice accretion, ρ_w [$\text{kg}\cdot\text{m}^{-3}$] is the density of water, V_w [$\text{m}\cdot\text{s}^{-1}$] is the wind speed in the i th hour, and Σ represents summation over hours for the duration of the freezing rain storm. In the denominator, $\rho_i\pi$ accounts for the expansion of water as it freezes, and the distribution of the assumed uniform distribution of water as it hits the ice covered cylinder.

A simplifying assumption is made whereby the transmission line subject to icing is assumed to be always perpendicular to the wind direction. Theoretically, this corresponds to a worst-case scenario and provides a conservative estimate appropriate for forecasting hazardous events.

[30] used freezing rain observations from the hourly aviation weather reports METAR to determine when to engage the SM model. However, an NWP-based forecasting system obviously cannot take storm observations into account. Instead, the precipitation type algorithm incorporated into IAFS uses the WRF output variable I_f (fraction of frozen precipitation) and the computed wet-bulb temperature, T_w , to determine the occurrence of freezing rain as described above. When the algorithm diagnoses freezing rain, IAFS engages SM

to calculate the radial equivalent ice thickness from the forecast precipitation amount at the current time step.

A difficulty arises when the precipitation type algorithm diagnoses a freezing mix. Under such circumstances, it is expected that only a portion of the total precipitation will accumulate in the ice accretion. Using a hard threshold at a particular value of I_f provided suboptimal results in the original IAFS [35]. In order to overcome this limitation, a fuzzy engagement function has been incorporated into the precipitation type algorithm to provide a gradual transition between accumulating all precipitation in the ice accretion and ignoring it altogether. In a similar manner, a fuzzy engagement function has been applied to the wet bulb temperature range, so that the amount of accumulated ice diminishes with increasing temperature near the freezing point. This new algorithm is called the fuzzy precipitation type algorithm.

The fuzzy engagement function, denoted by Γ , is a product of two components, described by Equations (16) and (17). One component, Γ_I , focuses on the fraction of frozen precipitation, while the other, Γ_T , on the wet bulb temperature.

$$\Gamma_I = \begin{cases} 1.0 & I_f < I_l \\ \frac{I_u - I_f}{I_u - I_l} & I_l \leq I_f \leq I_u \\ 0.0 & I_f > I_u \end{cases} \quad (16)$$

where I_l and I_u denote the lower and upper boundaries for the gradually decreasing segment of the engagement function. Values of I_f below the lower boundary cause full engagement, $\Gamma_I = 1$, while values above the upper

boundary, I_u , cause full disengagement, $\Gamma_I = 0$. Values of I_f between I_l and I_u produce a gradual transition between full and no engagement.

$$\Gamma_T = \begin{cases} 1.0 & T_w < T_l \\ \frac{T_u - T_w}{T_u - T_l} & T_l \leq T_w \leq T_u, \\ 0.0 & T_w > T_u \end{cases} \quad (17)$$

where T_l and T_u denote the lower and upper boundaries of the gradually decreasing segment for temperature. The temperature engagement operates analogously to Γ_I .

The two components of the engagement function are then combined

$$\Gamma = \Gamma_T \cdot \Gamma_I, \quad (18)$$

and used to reduce the value of R_{eq} computed by SM

$$R_{eq}^* = \Gamma \cdot R_{eq}. \quad (19)$$

In summary, the fuzzy precipitation type algorithm operates as follows. If I_f falls in the range $[0.00-I_l]$, liquid precipitation is diagnosed. If the wet bulb temperature is below T_u at that same time, freezing rain is diagnosed and the SM is partially engaged according to Γ_T and Equation (19). When $T_w < T_l$, the precipitation is considered to be composed entirely of freezing rain and is accumulated in its entirety. If I_f falls in the range $[I_l, I_u]$ and the wet bulb

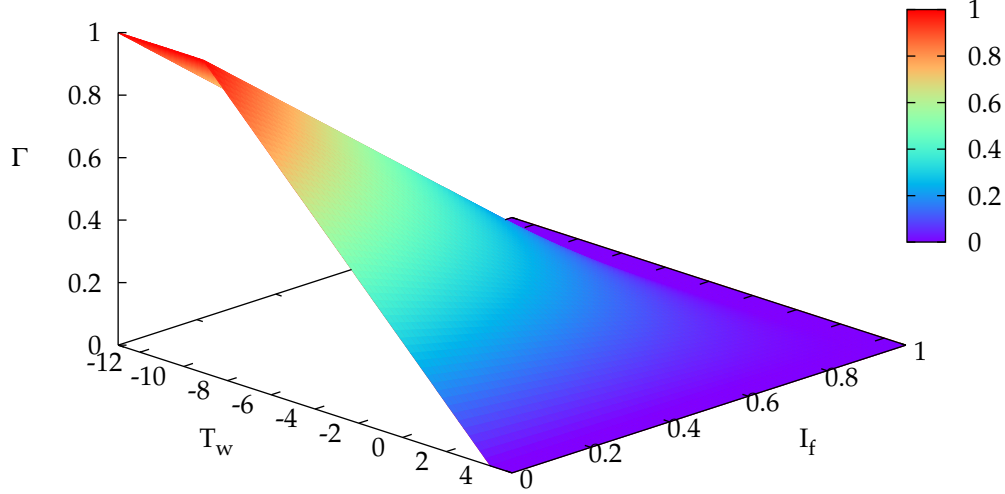


Figure 1: A plot of the IAFS engagement function with respect to wet-bulb temperature and fraction of frozen precipitation.

temperature is below T_u , mixed precipitation is diagnosed and the SM calculated ice load is reduced by a factor calculated by means of the engagement function Γ_I . An additional reduction dictated by Γ_T may also be performed if T_w falls in the range of $[T_l, T_u]$. When either the wet bulb temperature exceeds T_u or I_f exceeds I_u , SM is not invoked because the precipitation type is considered not to be freezing rain or mix. The result of these computations is illustrated by Figure 1.

To determine the total ice load accumulated during a freezing rain event, Γ multiplies the value of R_{eq} computed from SM in each model time step i

$$R_{eq}^{\text{final}} = \sum_{i=1}^N \Gamma_i \cdot R_{eq}^i. \quad (20)$$

In this way, it is possible to partially engage the model at every time step, and to vary the engagement factor from time step to time step.

3.3 EVOLUTIONARY OPTIMIZATION OF MODEL PARAMETERS

The fuzzy precipitation type algorithm used in IAFS relies on four parameters (T_u , T_l , I_u and I_l) to determine when to start and end the gradual transition between icing and non-icing conditions. IAFS [35] uses experimentally determined values that attempt to minimize the error of the icing hindcasts with respect to measured values. However, it is expected that parameters selected using an optimization technique will yield even smaller errors. This section presents a genetic algorithm approach to find parameters for the modified Ramer algorithm that is more generally applicable and can be applied to a wide variety of ice storms.

3.3.1 Data Description

A total of eight storm events were used for training, verification, and testing of IAFS. Initially, the ice storm of December 3-5, 2002 [30] was used to develop the GA-based optimization system and to perform initial training and cross-validation. This way, the same storm was used to train and validate the

A version of this section has been published in [80]. I made a substantial contribution to the material of this publication. I also wrote a major portion of the published manuscript.

system performance across the affected area. This first system, labelled IAFS-GA, was tested using four additional storms and, based on testing results, it was subsequently optimized using using all five storms (including the storm of 2002) and dubbed IAFS-5GA. Finally, performance of the optimized system was tested using three additional storms, entirely independent from the storms used for training.

The first storm (December 3-5, 2002) was documented in detail in [30]. The authors also provided analyzed ice accretion loads obtained from the Automated Surface Observing System (ASOS) ice sensors, and the ice loads diagnosed using two physical icing models with observed meteorological variables as inputs. Engagement of the models was controlled using the hourly aviation weather reports (METAR) to identify times when freezing rain occurred.

Additional storms were selected from the National Climatic Data Center Storm Database [81]. These were chosen because they produced a mix of sleet and freezing rain, to provide a sample of data having a wide range of I_f values, rather than just simple freezing rain events that would be trivial to identify with the original hard threshold engagement function. Furthermore, selection consideration was given to storms causing an appreciable amount of property damage and/or having an impact on the power transmission systems – the types of events that IAFS aims to provide an early warning for. A summary of all storms is provided in Table 1. All storms took place in the general region of Southeastern US (cf. Figure 2), covering an area of about $3,200 \times 900$ km, and including twenty observation stations listed in Table 2. Observations for the December 2002 ice storm were processed by domain experts (to account for other instrument observations and obvious malfunc-

3.3 EVOLUTIONARY OPTIMIZATION OF MODEL PARAMETERS

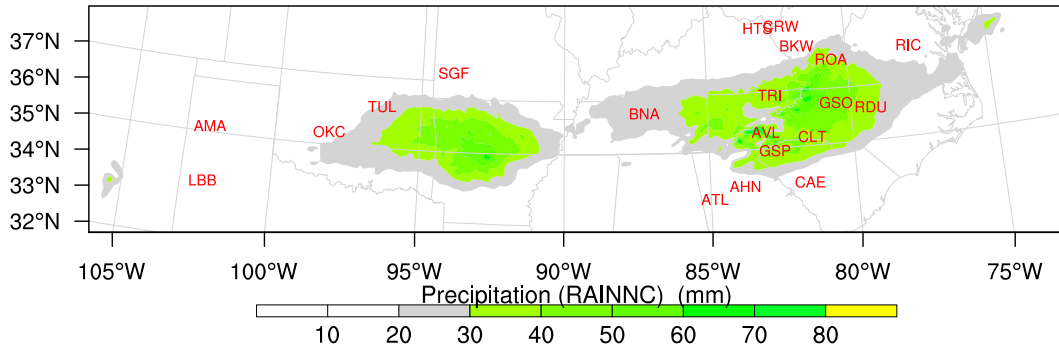


Figure 2: Total precipitation for December 3-5, 2002 as hindcast by the WRF model.

tions and calibration errors of the ASOS ice sensors), while observations for the remaining ice storms come from the raw ASOS sensor readings. Due to missing data, stations AMA, ATL, and CAE were excluded from the subsequent training and testing evaluations for the ice storms of 2008.

Previous studies [30] analyzed ice storms using ASOS and METAR observations. However, in order to forecast ice storms, NWP model variables must be used to drive ice accretion models, rather than observations and weather reports. With this in mind, all five ice storms were hindcast using IAFS. WRF output variables were used to drive the precipitation type algorithm and the SM of ice accretion.

To generate hindcasts for the ice storms, the WRF v3.0 NWP model was used. WRF is an open source, mesoscale, non-hydrostatic NWP model, developed for research and operational weather forecasting [82]. The WRF simulations for the ice hindcasts were performed using three nested grids with resolutions of 10.8 km (D01), 3.6 km (D02) and 1.2 km (D03). The outermost domain (D01) covered an area of about 168,500 km² with a 38×38 points grid. Detailed configuration parameters can be found in Appendix A, in Table 30.

Table 1: Description of storms used for development of the IAFS system; Use of each storm is marked as follows: □ cross-validation training of IAFS-GA, ■ verification of IAFS-GA, △ cross-validation training of IAFS-5GA, and ★ independent testing of both systems.

Event Date	Max. Ice Load [mm]	Impact
□ △ Dec. 3-5, 2002	60	major power outages; significant structural damage
■ △ Jan. 25-26, 2004	19	major power outages; moderate structural damage
■ △ Dec. 22, 2004	25	moderate power outages; minor structural damage
■ △ Feb. 1, 2008	50	major power outages; minor property damage
■ △ 21 Feb. 21, 2008	6	isolated cases of moderate damage
★ Feb. 27 2003	13	minor damage to trees and power lines
★ Dec. 15 2005	13	moderate damage to trees, power lines and property
★ Jan. 21 2007	6	minor damage to trees and power lines

For the purpose of this study, the North American Regional Reanalysis (NARR) historical dataset [83] was used to initialize the WRF model. This dataset comes in the form of meteorological variables defined on a 32-km horizontal grid, derived from NWP forecasts and assimilated weather observations.

For each considered ASOS location, a separate telescoping domain was used, positioning the station in the center of the domain. Because any finite numerical weather prediction model suffers from boundary effects and errors, it makes sense to keep the point of interest as far from the boundaries as possible, namely in the center of the domain. Placing each ASOS station at the central grid point of the domain also negates the need to perform interpolation between adjacent grid locations. This way, the most accurate training data was prepared for training IAFS. This approach is necessary only for tuning the parameters during system development, when exact localization is important. In operational forecasting, a potential small shift in icing localization will not bear as much significance, and a more common approach of setting one large domain over the entire area of interest can be used.

Table 2 lists the station identifiers, the ice loads inferred from the ASOS sensors, and the ice loads estimated based on meteorological observations by [30], using the SM [23] and CRREL models [84] for the December 2002 ice storm. The CRREL model improves upon SM physics by including heat transfer and icicle formation. However, it is not yet established that the model computes ice loads more accurately than SM. As a result, this model was not used in IAFS, especially since it is computationally more demanding. For completeness and ease of comparison, results obtained using the original

Table 2: Radial equivalent ice thickness, R_{eq} , determined by ASOS sensors, the difference of ice thickness modelled using CRREL (C) and SM with observed meteorological input as reported by [30] and using IAFS with hand-tuned and GA optimized parameters (2 variants) for the December 2002 ice storm. In the comparison, the ASOS measured ice accretion amounts are taken to be correct. Alt - altitude, Dist - distance from East coast

Station ID	City	Alt [m]	Dist [km]	Climate Division	R_{eq} [mm]		Difference w.r.t. ASOS [mm]				
					ASOS	C	SM	IAFS	GA	5GA	
AHN	Athens, GA	239.3	310	North Central	1.2	-1.2	0.8	-1.0	2.93	4.07	
ATL	Atlanta, GA	307.8	380	North Central	0.3	0.7	0.7	-0.3	-0.29	-0.19	
AVL	Asheville, NC	645.3	385	Southern Mountains	2.0	-2.0	0.0	-1.9	0.24	1.02	
AMA	Amarillo, TX	1098.5	1920	High Plains	4.5	-1.5	-0.5	-3.7	1.90	3.21	
LBB	Lubbock, TX	991.8	1945	High Plains	4.6	-1.6	0.4	-4.3	-2.38	-1.81	
BKW	Beckley, WV	766.3	420	Central	2.4	-2.4	-2.4	-2.4	-2.18	-0.40	
CRW	Charleston, WV	277.4	510	Southwestern	0.3	-0.3	-0.3	-0.3	0.43	0.59	
HTS	Huntington, WV	251.2	600	Southwestern	6.6	-0.6	0.4	-6.4	-1.33	-0.30	
BNA	Nashville, TN	182.9	700	Middle	2.1	-0.1	-0.1	-2.1	-2.08	-1.97	
TRI	Bristol, TN	457.2	445	Eastern	5.1	2.9	3.9	-4.9	0.44	1.69	
CAE	Columbia, SC	68.6	180	Central	5.8	0.2	3.2	-5.4	0.27	2.41	
GSP	Greer, SC	287.4	320	Northwest	0.8	1.2	1.2	-0.8	-0.73	-0.53	
CLT	Charlotte, NC	221.9	255	Southern Piedmont	0.3	-0.3	-0.3	-0.3	-0.22	0.15	
GSO	Greensboro, NC	271.3	200	Northern Piedmont	3.5	0.5	4.5	-3.5	-1.36	0.43	
RDU	Raleigh, NC	126.8	220	Central Piedmont	4.2	5.8	12.8	-3.7	1.38	3.02	
OKC	Oklahoma City, OK	391.7	1580	Central	1.6	3.4	4.4	-1.6	1.15	2.14	
TUL	Tulsa, OK	198.1	1450	Northeast	0.3	-0.3	-0.3	-0.3	0.21	0.62	
RIC	Richmond, VA	50.0	130	Eastern Piedmont	0.2	0.8	0.8	0.0	2.00	2.93	
ROA	Roanoke, VA	358.1	355	Central Mountain	1.7	1.3	4.3	-1.7	-1.66	1.43	
SGF	Springfield, MO	383.7	1280	West Ozarks	0.6	-0.6	-0.6	-0.6	0.33	3.43	

Table 3: Accuracy of WRF predictions with respect to observations of meteorological variables used by accretion models (BIAS - multiplicative bias, Mean Absolute Error (MAE), Correlation Coefficient R (CORR)).

Variable	BIAS	MAE	CORR
Temperature [$^{\circ}\text{C}$]	1.00	1.87	0.88
Wind speed [$\text{m}\cdot\text{s}^{-1}$]	1.33	1.76	0.51
Precipitation [mm]	0.94	0.77	0.82

IAFS [35] and two IAFS extensions (labelled GA and 5GA) described in this study, are included as well.

The WRF prediction accuracy of meteorological variables used by the accretion models, with respect to observations, is summarized in Table 3, in terms of multiplicative bias, Mean Absolute Error (MAE), and Correlation Coefficient R (CORR).

From Table 2, it is evident that the initial implementation of IAFS [35] underpredicts ice loads, despite a relatively accurate hindcast of total precipitation amount (MAE = 0.77 mm for the 6 hour precipitation amount over the entire data set, i.e. considering observations and forecasts at all twenty ASOS locations). This original system used parameters derived from the Ramer algorithm, i.e. $T_l = T_u = 0^{\circ}\text{C}$, $I_l = 0.04$ and $I_u = 0.85$. It was inferred that the poor performance of the system was possibly caused by incompatibility between the parameters of the precipitation type algorithm and the NWP model output. To resolve this problem, the parameters of the engagement function have been optimized as described in the following section.

3.3.2 Optimization of Ice Accretion Model Engagement Function

To improve the performance of IAFS, the parameters of the engagement function need to be set such that it correctly diagnoses the proportion of the total precipitation that actually freezes onto the accretion. To achieve this goal, the engagement function parameters have been submitted to an optimization process that evaluates correctness of the hindcasts by comparing them to ice accretion observations recorded by ASOS stations during the ice storms selected for this study.

3.3.2.1 *GA Implementation*

To optimize the parameters of the engagement function, a real-valued, GA-based optimization system has been implemented. Each of the four parameters is encoded as one of the genes in an individual chromosome

$$\text{chromosome}_i = \{I_l, I_u, T_l, T_u\}. \quad (21)$$

In order to successfully apply the GA to an optimization problem, an appropriate fitness function must be designed. A combination of four measures have been devised to calculate how well IAFS performs with candidate parameters of the engagement function. First, Root Mean Square Error (RMSE)

is calculated based on the difference between the IAFS hindcast ice accretion (radial equivalent thickness, R_{eq}) and the ASOS measurement

$$\text{rmse} = \sqrt{\sum_i (\text{hindcast}_i - \text{measured}_i)^2}. \quad (22)$$

RMSE is used in preference to mean absolute error in order to promote solutions that provide accurate hindcasts for larger icing events. The error follows a quadratic relationship with respect to the difference between the hindcast and observation, thus placing a much higher weight on large errors that would be of significance for a hazard-forecasting system.

Second, the relative error is calculated,

$$\text{re}_i = \frac{\text{calculated}_i - \text{measured}_i}{\max(\text{measured}_i, 1.0)}. \quad (23)$$

Rather than simply adding it to the fitness value, it is augmented by a negative coefficient when the tested parameters cause IAFS to underestimate the amount of ice accretion,

$$\text{re}_i^a = \begin{cases} \text{re}_i & \text{re}_i \geq 0.0 \\ -2 \times \text{re}_i & \text{re}_i < 0.0 \end{cases}. \quad (24)$$

This favours conservative estimates that slightly overpredict, in comparison with hindcasts with smaller errors that give consistent underprediction. As mentioned earlier, this is appropriate for a hazard-forecasting system such

as IAFS. The resulting error value calculated using this measure is always positive, to ensure that relative errors do not cancel each other when combined for all tested locations in a given training or testing set. This value is then normalized to provide an error of the predicted R_{eq} per millimeter of observed ice, because of the variability among icing loads measured at various locations. The reason for this choice is to balance the contributions of large and small icing events, so that a single large error in a large event would not skew the results in its favour, leaving smaller events ignored. However, if the magnitude of the measured ice thickness is less than 1.0 mm, then normalization is not performed. This is to prevent small errors from having an abnormally large influence on the resulting fitness, due to the asymptotic behaviour of the normalization function as the value of the measurement tends to zero.

Third, to reduce the overall bias of the model so as to minimize the relative error of the total ice hindcast across all locations, the square root of the absolute difference between the total ice hindcast and the total observed ice amount is computed

$$ste = \sqrt{\sum_i |\text{calculated}_i - \text{measured}_i|}. \quad (25)$$

The square root is used to ensure that the magnitude of this error measure is comparable to the previous two measures, and more importantly to take into account the other error measures even when the total error is large. Otherwise, this error would dominate the fitness function.

The final component of the fitness measure is designed to favour solutions that form a fuzzy transition between the icing and non-icing extremes

$$\begin{aligned} \text{bf} = & 0.01 \times [\log(I_l + 1) - \log(I_u + 1)] \\ & + \log(|T_l| + 1) - \log(|T_u| + 1)]. \end{aligned} \quad (26)$$

This is accomplished by incorporating the assumption that for a “good” solution, the values of I_l and T_u will be close to zero while I_u will be closer to unity and T_l will take on some negative value. By the nature of the problem, the optimal value for each parameter is not known, and thus no exact error formula can be written. To provide a means of assessing whether the parameters are “good” or “bad,” a logarithm is taken of each engagement function parameter. A value of unity is added to the magnitude of each parameter to compensate for the fact that for values less than unity, $\log(x)$ is negative. In this manner, when the value of a parameter is close to the expected value, the calculated value is small or slightly negative. However, when the parameter value moves away from the expected range, the value of this term increases. The logarithmic function is used so that when a parameter moves away from its expected range, the value of this measure tapers off.

Because this term potentially introduces human bias as to what the solution should look like, its influence is kept to a minimum by multiplying the four components by a coefficient of 0.01. This prevents the measure from having a significant effect when comparing two genotypes with vastly different error measures. However, the contribution becomes important when two different genotypes with similar error values are evaluated. In such cases, it will favour the individual whose threshold parameters form a smooth and

Table 4: GA parameters used in the IAFS optimization process.

Parameter	Value
Population size	300
Mutation rate	0.15
Crossover rate	0.3
Elite size	10
Number of training trials	30
Minimum number of iterations	500
Minimum of no-fitness-change iterations	10
Maximum number of iterations	10000

gradual transition between icing and non-icing conditions (i.e. a fuzzy range) as opposed to parameters that form a hard threshold (i.e. with identical lower and upper bounds).

For each candidate solution, the components of the fitness measure are summed in order to determine its overall fitness value

$$\text{fitness} = \text{rmse} + \sum_i \frac{\text{re}_i^a}{n} + \text{ste} + \text{bf}. \quad (27)$$

The search space for the GA training process is limited to physically realistic ranges under which freezing rain events are expected to occur. The search space for the wet-bulb temperature is set from -10°C to 10°C , while the search space for the fraction of frozen precipitation is limited to $[0,1]$. These restrictions also speed up the learning process.

The operational parameters for the GA used for IAFS parameter optimization are listed in Table 4.

3.3.2.2 *Development of the Forecasting System*

The initial training and verification of IAFS-GA was performed using the WRF hindcast data for the December 3-5, 2002 ice storm. The analyzed event data collected from 20 separate ASOS stations and presented in [30] was used to compare with the hindcasts provided by IAFS.

Cross-validation [85] was used to train the system, and subsequently to verify its accuracy on the hold-out set. This approach allows the use of a small data set to train, and at the same time to verify the applicability of the model on untrained cases in order to check the generality of the solution. In cross-validation, the training data is separated into two sets. The first, usually much larger, is used to train the system. The second set is to verify the discovered parameters of the system on untrained data, to ensure that the decrease in error of the model is not the result of overfitting the training data at the expense of generality. Thus, when using cross-validation, the system is assessed on multiple independent random samples that are not included in the training process. As a result, this approach is able to provide a more meaningful verification of the developed solution.

Initially, ten-fold cross-validation was performed on the December 2002 ice storm to assess the feasibility of using a GA to optimize IAFS, and to analyze the characteristics of the optimized engagement model. The best set of parameters found using a ten-fold cross validation session has the following values: $I_l = 0.005$, $I_u = 0.776$, $T_l = -7.293$ °C, and $T_u = 1.494$ °C. A statistical summary of the cross-validation sessions is given in Figure 3.

A comparison of IAFS-GA hindcast loads to the results from [30] and [35] is presented in Table 5 and Figure 4. Figure 5 shows the scatter plot of the

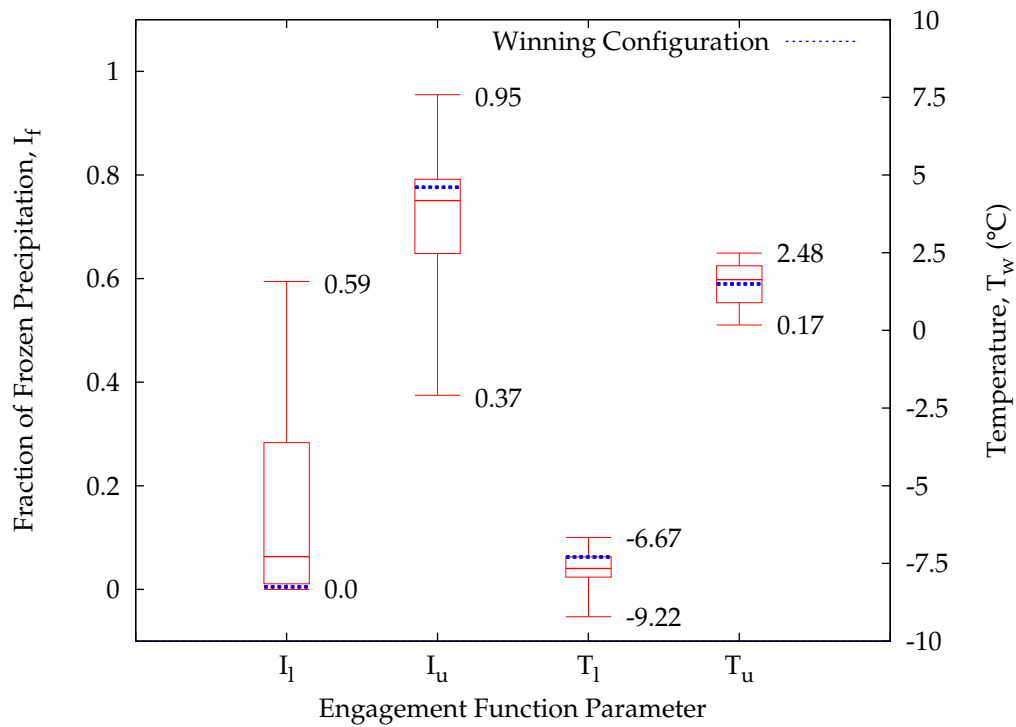


Figure 3: Distribution of the calculated engagement function parameters obtained by the GA using the December 2002 ice storm. The dotted line represents the position of the winning configuration within the range of parameter values, shown by the bars and whiskers, obtained from the cross-validation sessions.

Table 5: Sum of the radial equivalent thicknesses, R_{eq} , for all 20 ASOS stations, and errors relative to the ASOS sensor output for the December 2002 ice storm. (E is the difference of total ice accretion over all stations, AE is the the sum of absolute differences over all stations, and MAE is the mean absolute error over all stations.)

	R_{eq} [mm]	E [mm]	AE [mm]	MAE [mm]
ASOS	48.10	-	-	-
CRREL	54.00	+5.90	27.70	1.39
SM	81.00	+32.90	41.90	2.10
IAFS	30.07	-18.03	23.59	1.18
IAFS-GA	47.17	-0.93	23.54	1.18
IAFS-5GA	70.04	21.94	32.36	1.62

hindcast radial equivalent ice thickness (using IAFS-GA) with respect to the ASOS observations published by [30].

The new parameters slightly underestimate the total hindcast thickness of ice accumulated over all stations, bringing it to within 2% of the accumulated ice thickness recorded by the ASOS stations during the storm. This is a very significant improvement from the total error of -36% obtained in the previous study [35] using the engagement function parameters based directly on the Ramer algorithm. Looking at the individual station predictions, 9 stations had underpredicted values, but only 6 stations had errors greater than 1 mm (ranging between 1.36 mm and 2.38 mm). On the opposite side of the spectrum, 5 stations had overpredicted values by 1 mm or more (ranging between 1.15 mm to 2.93 mm). From a practical perspective, errors on the order of 1 mm do not pose an obstacle to use IAFS as an ice accretion early warning system, especially when larger errors are for accumulated ice amounts significantly less than the power line design criteria for wind and ice load handling. Should IAFS underpredict ice accretion for amounts near the design criteria, the early warning system could miss events that may potentially cause line

3.3 EVOLUTIONARY OPTIMIZATION OF MODEL PARAMETERS

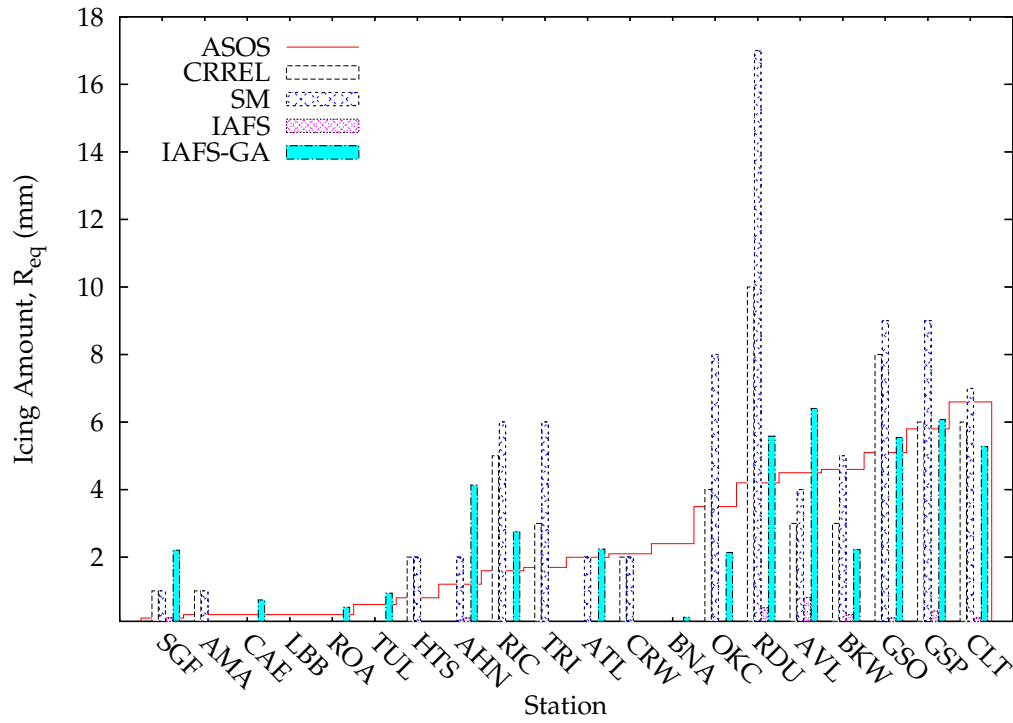


Figure 4: Comparison of icing model accuracy for December 2002 storm with respect to observations from 20 ASOS stations.

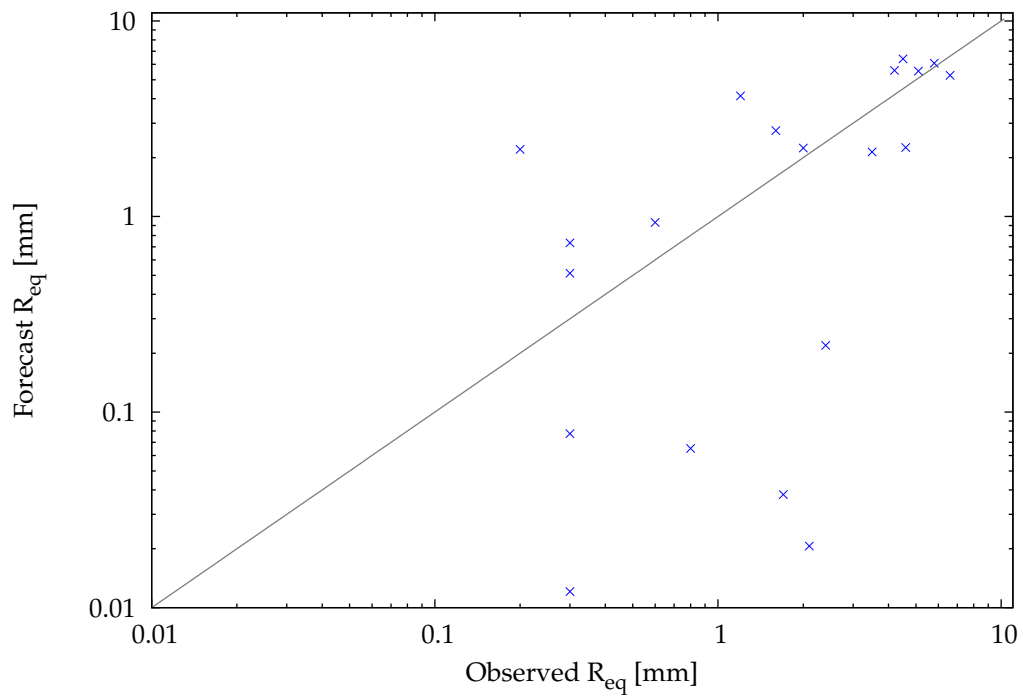


Figure 5: Plot of observed vs. hindcast radial equivalent ice thickness for the December 2002 ice storm, using IAFS-GA; correlation = 0.73.

failure. On the other hand, overprediction of ice accretion carries the risk of having utilities needlessly expend resources in anticipation of potential line failures.

Table 5 illustrates that IAFS-GA outperforms previous systems documented in the literature. It underpredicts the total radial equivalent ice accretion by only 0.93 mm when compared to the observed values, while maintaining an Absolute Error (AE) and MAE nearly identical to the original IAFS implementation.

When examining the distribution of recorded precipitation types and amounts with respect to I_f and T_w , in Figure 6, it is evident that the optimized parameters take into consideration the fact that the majority of the freezing rain occurs when I_f is in the range of $\approx[0-0.18]$ and when the temperature is under about 1.5°C . It is also evident that precipitation in the form of snow is gradually mixed in with freezing rain as T_w decreases, even though the value of I_f from the WRF model indicates that a portion of the precipitation should be liquid.

During ten-fold cross validation, the majority of the discovered parameter values for Γ_I are consistently grouped together. The calculated values for I_u range between 0.375 and 0.955, with the majority centering around a value of 0.751. This upper range for this parameter is similar to that used by Ramer (0.85). However, the optimal value of the engagement function is 0.776. This confirms that when a large proportion of the precipitation is in solid form, it does not contribute to ice accretion growth.

For I_l , six out of ten values were below 0.05. Again, this supports the lower limit of 0.04 for freezing mix used by the Ramer algorithm. It indicates that there is a transition from accumulating all precipitation into the ice structure

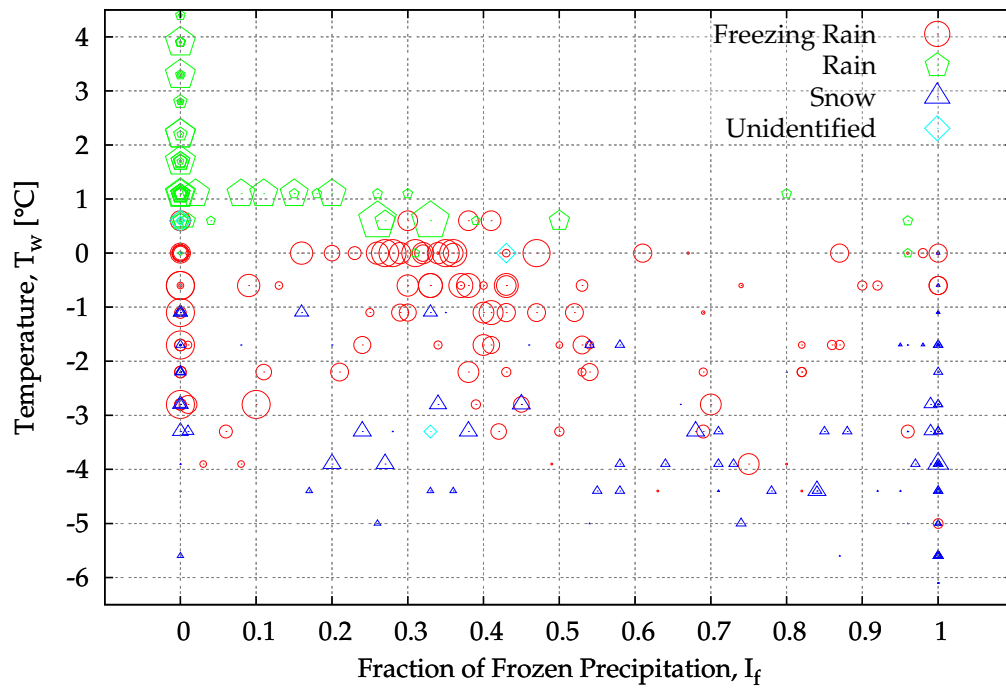


Figure 6: Observed precipitation type as a function of I_f and T_w . The size of the symbols corresponds to the relative amount of the total observed precipitation.

to no ice accumulation, and the best values of the parameter come from this grouping of values. This makes physical sense from the perspective of IAFS. When the majority of the precipitation is in liquid form, it will incorporate into the ice structure and any remaining solid precipitation may stick to the wet surface and freeze to the accreted ice. However, once a greater proportion of the precipitation is in solid form, not all will manage to cling and adhere to the ice structure.

The average value of T_u is 1.47°C , with most instances near 1.6°C . This would suggest that ice accretion tends to cease as soon as the wet-bulb temperature rises to just slightly above 0°C ; however, the optimal parameter takes on a value of 1.50°C . This parameter must be slightly higher than the warmest temperature at which ice accretion occurs, in order to ensure that the engagement function will not have a value of zero at the given temperature, and subsequently exclude this ice accretion from the total accumulation. The discovered parameter value supports the ASOS observations, which showed a number of freezing rain occurrences during non-freezing ambient air temperatures, as previously described. A possible explanation for this could be the fact that the falling liquid precipitation droplets are sufficiently supercooled to freeze to the structure on impact, despite the above freezing values of T_w . It should be noted, however, that at these temperatures, only a small fraction of the ice accretion amount predicted by SM is considered by IAFS. Additionally, as the ambient temperature approaches 0°C , there is a decrease in heat transfer from the ice accretion, which also contributes to a reduction in the amount of accumulated ice relative to that predicted by the SM. The values of T_l range between -9.22°C and -6.67°C among different folds, with the

Table 6: Error statistics of IFAS-GA for five testing storms.

Date (Total R_{eq} [mm])	E [mm]	MAE [mm]	CORR
Dec 3, 2002 (48.10)	-0.90	1.18	0.78
Jan 25, 2004 (23.3)	-19.37	1.04	0.53
Dec 22, 2004 (6.63)	-4.68	0.23	0.98
Feb 1, 2008 (11.32)	-4.29	0.56	0.45
Feb 21, 2008 (11.03)	-9.51	0.62	0.58
All storms (100.42)	-38.75	0.74	0.73

majority of the temperature values grouping near -7.66°C . These values are consistent with Ramer’s hard cut-off temperature for snow at -6.6°C .

IAFS-GA was trained using a single storm, and the cross-validation approach verified its performance only using the same storm. In order to implement a more thorough validation of the model, four additional storms were used to assess its performance. The error statistics of the IAFS-GA hindcast for each storm and all storms combined, are presented in Table 6. Although the overall mean absolute error was only 0.74 mm, the system underpredicted the total ice accumulation for all five storms (100.42 mm) by 38.75 mm, with the single storm of January 25, 2004 contributing about 50% of this error.

3.3.2.3 Optimization of the Forecasting System

As shown in the previous section, IAFS-GA performed well on the storm used for training (December 3-5, 2002), but its performance degraded when applied to other storms. In other words, the system was not capable of generalization. However, a learning system such as GA should be capable of learning a more general solution, and of ignoring and/or learning to compensate for errors present in a subset of the data. To analyze this problem, new training was performed on each storm individually, and on all storms

combined. The optimal engagement function parameters found using 10-fold cross-validation training on individual storms, are presented in Table 7. Indeed, the parameters found using data from different storms mismatch considerably. A closer look at the training data, shown in Figure 7, confirms this observation, and offers an explanation. While the ice storm of December 2002 broadly covered a large area of the engagement function parameter search space, this coverage was not even, i.e. there was a bias in how the storm covered various combinations of T_w and I_f , both in terms of their frequency and the magnitude of the associated accretion (cf. Figure 6). In comparison, the other storms cover with different frequency other areas of parameter space. This can be clearly seen in Figure 7, particularly for the two storms that occurred in 2008. The variation can be attributed, at least in part, to different extent and severity of the storms with total accretion load ranging from 6.63 to 48.10 mm. Additionally, other factors not considered in the training of the engagement function, such as thickness and height of air layers, vertical profile of moisture in the atmosphere, motion of air in the atmosphere, and atmospheric pressure and tendency could potentially help better differentiate the different storms.

From a training perspective, this means that a general solution cannot be found by the GA when training on a single storm with limited coverage of conditions. The GA is unable to evaluate a broad range of alternative choices, because it does not have data to support or reject a given candidate solution.

To overcome this problem, training was repeated using a data set formed by merging data for all five storms (cf. Table 7). To avoid overfitting the data, an alternative cross-validation method of random sub-sampling was used. This approach is suitable for larger data sets, such as the one used for train-

Table 7: The optimal parameters of the engagement function discovered using the GA optimization process for each considered ice storm during a 10-fold cross-validation session.

Event	I_l [-]	I_u [-]	T_l [°C]	T_u [°C]
3 Dec 2002	0.005	0.78	-7.29	1.49
25 Jan 2004	0.84	1.00	-4.85	5.52
22 Dec 2004	0.00	0.16	-10.00	9.75
1 Feb 2008	0.23	0.49	-9.20	3.05
21 Feb 2008	0.19	0.50	-0.20	7.61

ing in this case. As with n-fold cross-validation, this approach splits the data into a training and validation set; however, the sets are formed by randomly selecting (without replacement) the training and testing set for each round. This way, the number of testing rounds that can be performed is not limited by the size of the groups, as in n-fold cross-validation. During each round, a random group of 60% of ASOS station observations were used to optimize the engagement function. Subsequently, the discovered parameters were evaluated on the remaining 40% of observations, which the engagement function parameters had not been trained on.

The best parameter set, labeled IAFS-5GA, has the following values: $I_l = 0.0$, $I_u = 0.93$, $T_l = -9.10$ °C, and $T_u = 4.02$ °C. A statistical summary of the distribution of the ten parameters is presented in Figure 8. It is interesting to note that the newly found ranges show a refinement of those originally obtained from the December 2002 storm (cf. Figure 3). From this, it can be inferred that, given a larger sample of accurate training data, the system could be further refined to improve upon the icing hindcast/forecast accuracy. Additional storms can be added into the training set until the deviation between parameter values from different cross validation sessions converges.

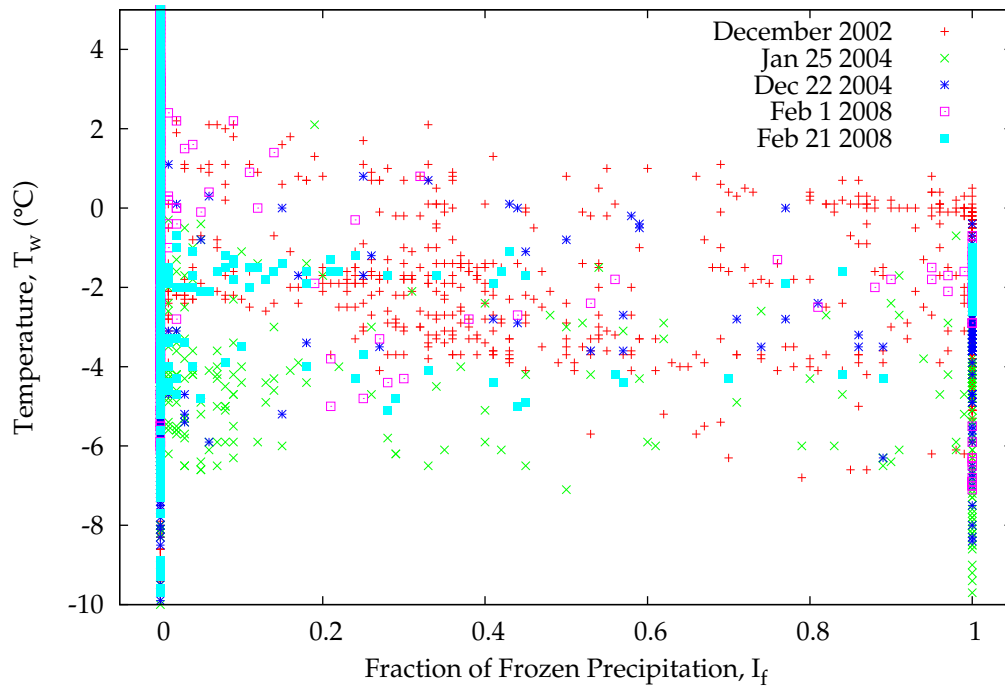


Figure 7: Distribution of the wet bulb temperature and the fraction of frozen precipitation for the five ice storms used for cross-validation training of IAFS-5GA.

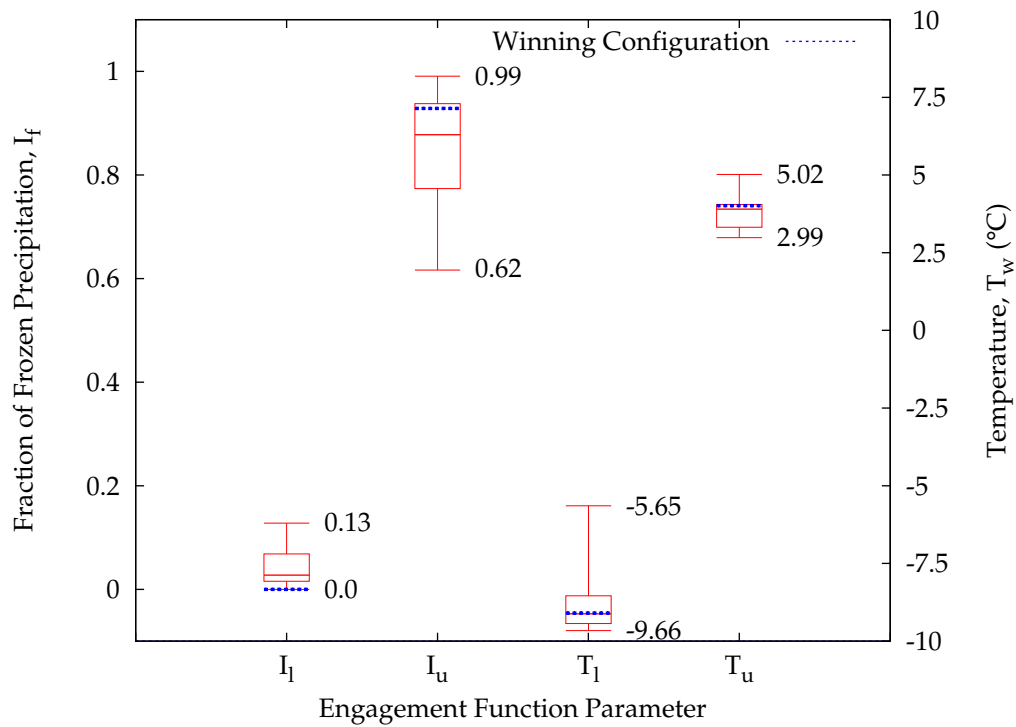


Figure 8: Distribution of the calculated parameters of the engagement function discovered using the five ice storms for cross-validation training of IAFS-5GA. The dotted line represents the position of the winning configuration within the range of parameter values, shown by the bars and whiskers, obtained from the cross-validation sessions.

Table 8: Error statistics of IAFS-5GA for the training set, testing set and all considered stations, and averages of the error statistics for top ten parameters from the random sub-sampling cross-validation session using all five ice storm events (5GA).

Measure	Winning Params			Top Ten Average		
	Training	Test	Full	Training	Test	Full
MAE [mm]	0.92	0.79	0.87	0.85	0.88	0.86
E [mm]	0.00	-2.94	-0.03	0.00	-4.82	-4.82
ME [mm]	0.00	-0.09	1.40	0.00	-0.15	-0.05
CORR	0.67	0.74	0.70	0.71	0.66	0.70

Table 9: Error statistics of IAFS-5GA for each of the five considered ice storms.

Date (total R_{eq} [mm])	E [mm]	MAE [mm]	CORR
Dec 3, 2002 (48.10)	21.98	1.62	0.76
Jan 25, 2004 (23.3)	-17.82	1.00	0.47
Dec 22, 2004 (6.63)	-2.35	0.29	0.98
Feb 1, 2008 (11.32)	5.58	0.81	0.32
Feb 21, 2008 (11.03)	-9.09	0.60	0.53
All storms (100.42)	-1.69	0.88	0.70

The evaluation of the new winning engagement parameter is shown in Table 8. It can be observed that the system provides a mean absolute error of only 0.79 mm on the validation set, which is composed entirely of untrained observations. Furthermore, the total ice hindcast error on all the test set stations is only -2.94 mm, illustrating that the model is relatively unbiased, with a minor tendency to underpredict ice loads. This is confirmed by the mean error of -0.09 mm. The average mean absolute error for the ten parameter sets on each respective testing set rises by just 0.1 mm, while the average total error increases by 1.90 mm with respect to the winning combination. Error statistics for each storm, as hindcast by the IAFS-5GA parameters, are presented in Table 9.

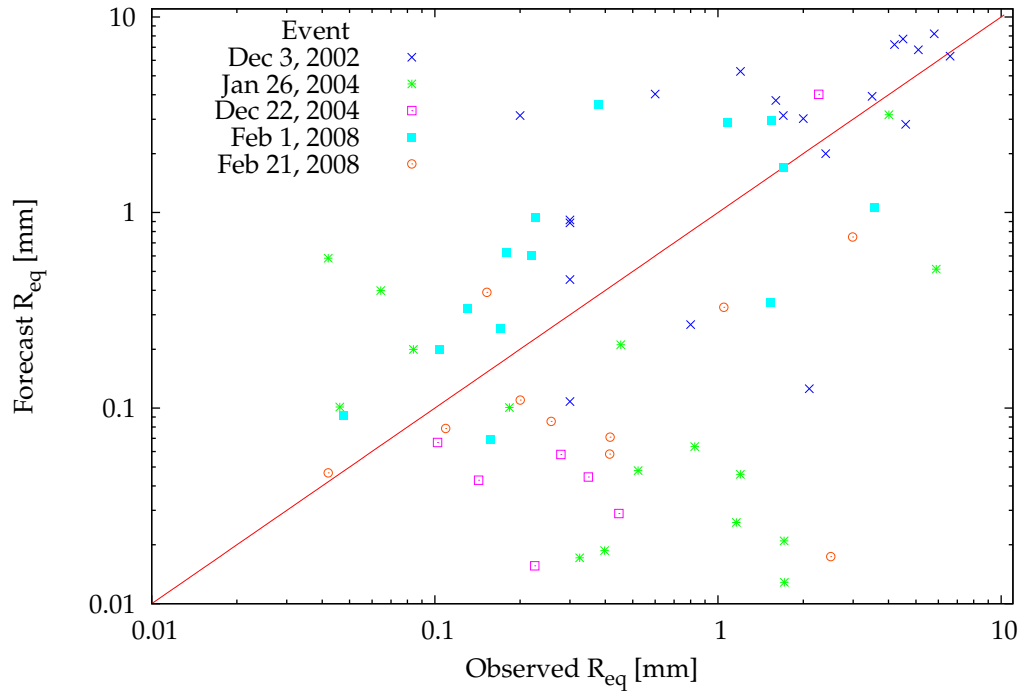


Figure 9: Plot of observed vs. hindcast radial equivalent ice thickness for all five events using the winning parameters based on all five ice storm events considered in this study; correlation = 0.70.

The bias and accuracy of the optimized parameter set for all five storms can be seen in Figure 9. From the scatter plot, it is clear that the IAFS-5GA remains unbiased. It is interesting to note that the majority of underpredicted loads occur for small ice accretion amounts. This is significant on two counts. First, small ice accretion observations are subject to instrument sensitivity and can be easily misdiagnosed. Secondly, and more importantly, IAFS-5GA has a very small error for large ice accretions (> 5 mm). This means that the system will provide much higher accuracy for more significant events, which are of interest to meteorologists, utility operators and the public.

Table 10: Error statistics of IAFS-5GA for each of the three ice storms used for testing.

Date (total R_{eq} [mm])	E [mm]	MAE [mm]	CORR
Feb 27, 2003 (27.19)	2.9	0.97	0.74
Dec 15, 2005 (39.64)	-2.73	0.86	0.86
Jan 21, 2007 (16.34)	-3.3	0.9	0.34
All storms (83.17)	-3.13	0.91	0.77

3.3.2.4 Evaluation of the Forecasting System

The cross-validation training process used to develop IAFS-5GA resulted in an improved prediction across all five ice storms used for training. To establish whether the system will provide improved predictions when applied to completely independent cases, three additional storms have been selected from the Storm Database: February 27, 2003, December 15, 2005, and January 21, 2007. These storms brought 6–12 mm of maximum local icing totalling about 16–40 mm across the ASOS stations in the area of interest, and caused minor to moderate damage to trees and structures.

Error statistics for each storm, as hindcast by the IAFS-5GA parameters, are presented in Table 10. The system provides consistently good results. The total error is -3.13 mm on the three new storms, compared to -1.69 mm using the training storms. Similarly, the mean absolute error is 0.91 mm for the new storms, compared to 0.88 mm. Correlation is also comparable with value of 0.77 for the new storms and 0.70 for the storms used for training.

To evaluate the forecast skill of the new approach, it has been compared to SM with a simple engagement function ($-6.6 < T_w < 0$, $SR < 0.85$), IAFS-11 [35], and to IAFS-GA, using the three storms from Table 10. The results of this comparison in terms of total error are presented in Table 11. IAFS-5GA

Table 11: Icing forecast skill of various IAFS in terms of total error (sum of ice accretions over all station in the area of interest) compared to SM with a simple Ramer-like engagement function ($-6.6 < T_w < 0$, $SR < 0.85$).

Date (total R_{eq} [mm])	Forecast skill			
	SM	IAFS		
		11	GA	5GA
Feb 27, 2003 (27.19)	0	42.6	27.2	82.6
Dec 15, 2005 (39.64)	0	95.9	58.9	93.8
Jan 21, 2007 (16.34)	0	-98.8	-168.3	20.7
Training storms (100.42)	0	29.0	72.4	97.9
Testing storms (83.17)	0	65.3	26.9	94.5

has much improved skill compared to SM. It also outperforms IAFS-11 and IAFS-GA on all three storms individually, as well as on training and testing groups of storms. As can be expected, there is a slight decrease of skill when comparing the system performance on training and testing storms. However, the skill degradation is very small, demonstrating good generalization properties of the system.

3.4 APPLICATION

The development, optimization and validation of IAFS, described in the previous section of this chapter, are based on reanalyzed historical data. In order to evaluate the ability of IAFS to forecast ice accretion amount in operational use, additional simulations were performed using true forecast data. For this purpose, the recent Newfoundland ice storm which took place on March 2010 was selected. The following section describes the use and performance of the

A version of this subsection has been published in [86]. I made a substantial contribution to the content of this publication.

optimized IAFS to predict this ice storm. It compares the simulated meteorological variables to observations and reports, and assesses the ability of the model to predict the ice accretion load for different forecast horizons.

3.4.1 Newfoundland 2010 Ice Storm Event

The Canadian Maritime Provinces and the Northeastern states of the USA are often affected by severe ice storms caused by freezing rain. In March 2010, a severe ice storm struck the island of Newfoundland, leaving many people without power for several days. During this event, the most intense freezing rain occurred overnight on March 4 and throughout March 5. The storm caused extensive power outages affecting about 7000 customers in 32 communities on the Bonavista Peninsula and 22 in the northern Avalon Peninsula. The outages were caused by physical damage to about 250 power distribution lines and support structures that broke under the weight of accreted ice. Media reported that conductors were covered with ice up to 12 cm thick [87]. This shows the potential magnitude of freezing rain storms, and illustrates their technical, economic and societal consequences. It would be highly desirable to model and forecast such icing events, so that the consequent damages can be prevented or mitigated.

3.4.1.1 *Ice Storm Description*

A surface low pressure system formed on March 2, 2010 over the Gulf of Mexico; it started to move towards the northeast, driven by the flow in the middle troposphere. The depression deepened on March 3, while passing Cape Hat-

terras on the US east coast. The minimum sea-level pressure dropped from 1002 hPa on March 2 to 986 hPa on March 3. The storm hit southeastern Newfoundland on March 5, and brought rain and freezing rain to the exposed northeastern coast of the island. The slowly moving storm produced rain for about two days. The highest total precipitation exceeded 110 mm on the Avalon Peninsula.

In terms of its duration and maximum precipitation, this storm is comparable with the Great Ice Storm of January 1998. Another common characteristic was that both storms were slow moving. The major differences were the spatial extent of the icing, and the fact that, luckily, much of the area affected by the more recent storm has a relatively low population density. However, low population density can cause long restoration times due to the prioritization of line repair operations [88].

3.4.1.2 *NWP Model Setup*

Weather simulations for this ice storm study were performed using the WRF model version 3.2. Detailed configuration parameters can be found in Appendix A in Table 31. Three nested model domains were used with grid sizes of 10.8 km (D01), 3.6 km (D02) and 1.2 km (D03), and grid dimensions of 47×52 , 64×79 , 118×163 , respectively. The innermost domain, covered an area of 141.6×195.6 km, and it is shown in Figure 10, along with the main power line on the Bonavista Peninsula.

In order to reproduce the conditions of a real forecast, initial and boundary conditions were obtained from the North American Model (NAM) data products, which are based on global model forecasts. Although this simulation was carried out after the storm occurred, it was initialized and provided

with boundary conditions from NAM forecasts available up to 84 h prior to the main icing event. To determine how far ahead the ice storm could be predicted, forecast horizons of 64, 52, 40, 28 and 16 h relative to the main event were considered. No observation nudging or data assimilation was performed.

3.4.2 Evaluation

Before analyzing the freezing rain ice accretion model, relevant simulated meteorological parameters (precipitation, wind speed and temperature) were compared with surface measurements inside the innermost domain. This domain encompasses five meteorological stations operated by Environment Canada. Most of the stations make only daily observations. Only one station, Bonavista, provides data with hourly resolution, suitable for temperature and wind speed verification. All model values used for the comparison were transposed using bilinear interpolation from the original gridded WRF output to the site of the Bonavista station.

The amount of freezing rain is the most important factor determining the intensity of glaze icing. However, since observations of freezing rain were not available at any of the five stations, instead daily totals of precipitation observed on March 5 and 6 were compared with the total precipitation provided by the NWP model. However, because total precipitation may include rain, freezing rain, ice pellets and snow, this is not an ideal comparison. Nevertheless, it may indicate whether or not the model has a systematic tendency to underestimate or overestimate precipitation in general.

Table 12: Daily total precipitation observed on March 5, 2010, and simulated total precipitation for the same period.

Meteorological station	Elevation [m ASL]	Observed [mm]	Simulated with start at:	
			March 4, 0:00 UTC	March 4, 12:00 UTC
Bonavista	25.6	28.1	12.1	22.0
Brownsdale	10.0	14.0	21.6	27.2
Lethbridge	15.2	15.0	19.3	29.3
Terra Nova	106.7	60.3	19.2	33.7
Whitbourne	58.0	23.0	32.4	23.9
MAE			15.7	12.2

Table 13: Daily total precipitation observed on March 6, 2010, and simulated total precipitation for the same period.

Meteorological station	Elevation [m ASL]	Observed [mm]	Simulated with start at:	
			March 4, 12:00 UTC	March 5, 0:00 UTC
Bonavista	25.6	22.3	5.6	2.4
Brownsdale	10.0	86.0	3.1	10.7
Lethbridge	15.2	8.0	6.1	2.7
Terra Nova	106.7	28.5	4.5	5.4
Whitbourne	58.0	10.6	2.1	13.5
MAE			11.3	10.7



Figure 10: The inner domain of the WRF model (141.6×195.6 km) and the main power distribution line on the Bonavista peninsula (white).

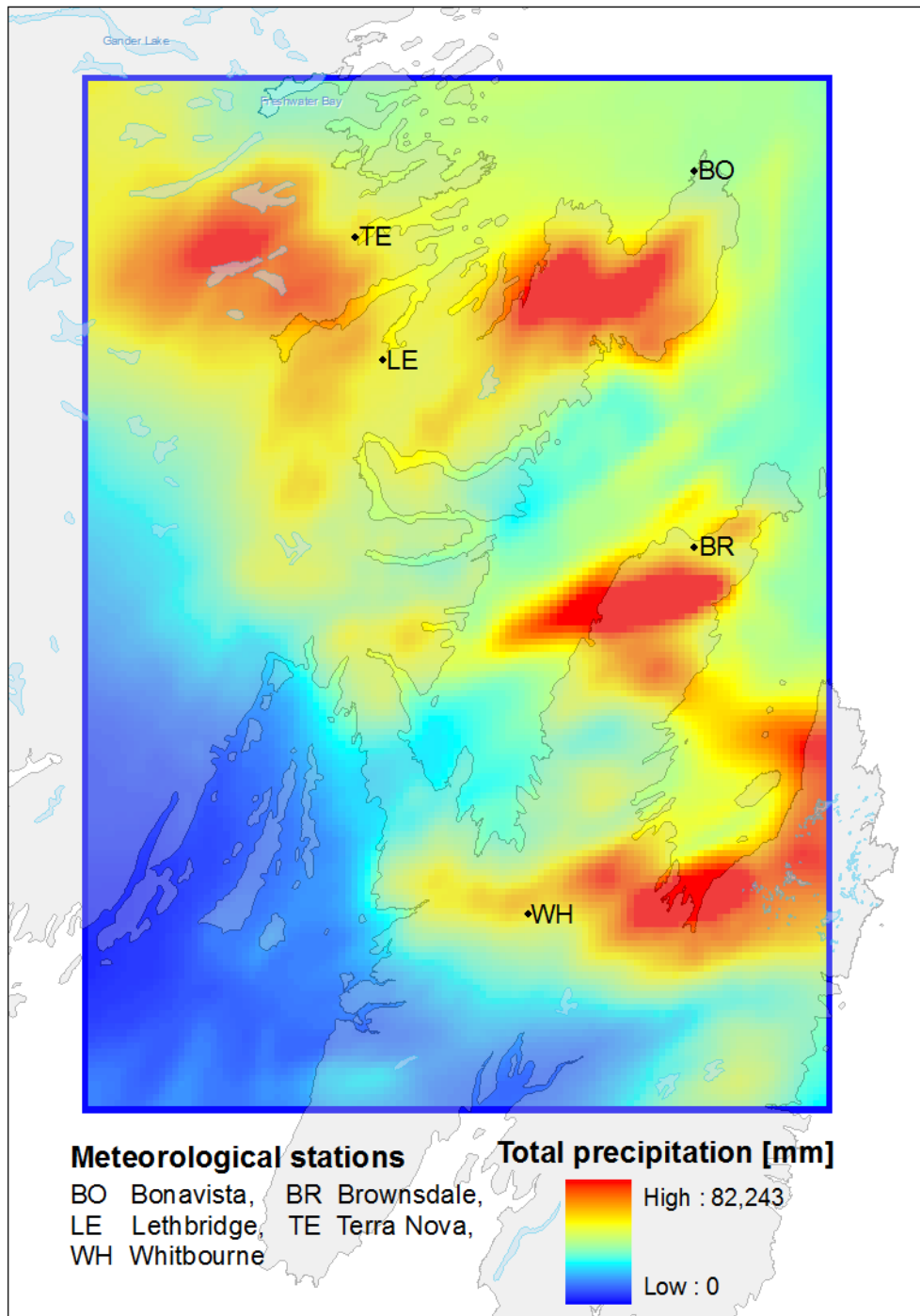


Figure 11: Total precipitation for the entire event (March 5 and March 6) as simulated starting on March 5 0:00 UTC.

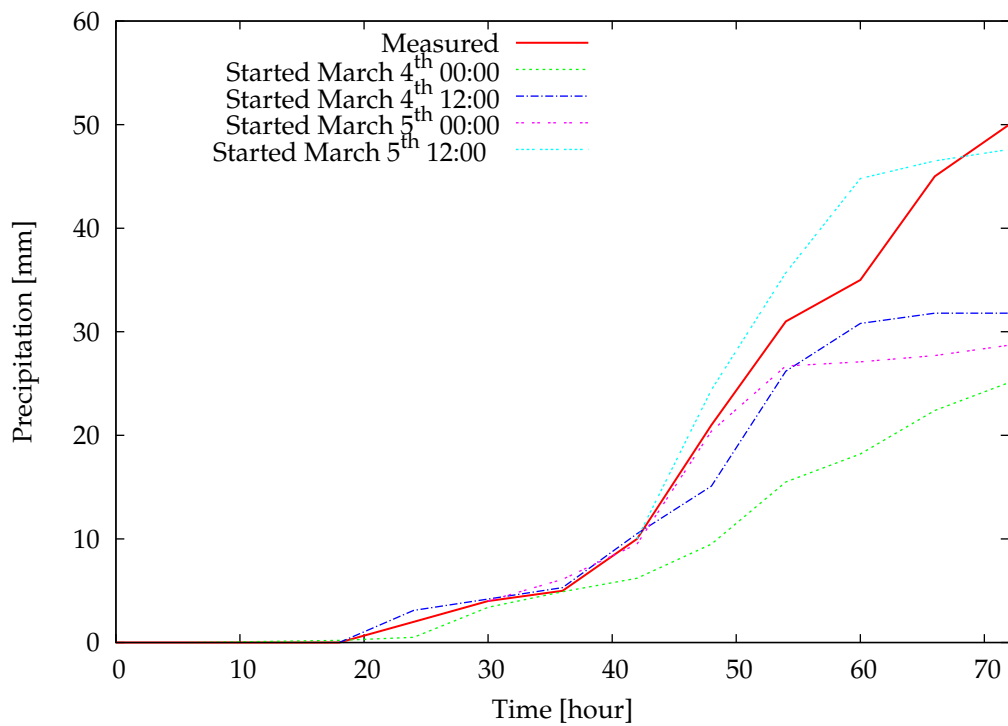


Figure 12: Cumulative observed 6-hour total precipitation amounts at Bonavista and corresponding total precipitation simulated by WRF started on March 4 and 5; time in hours after March 4 0:00 UTC.

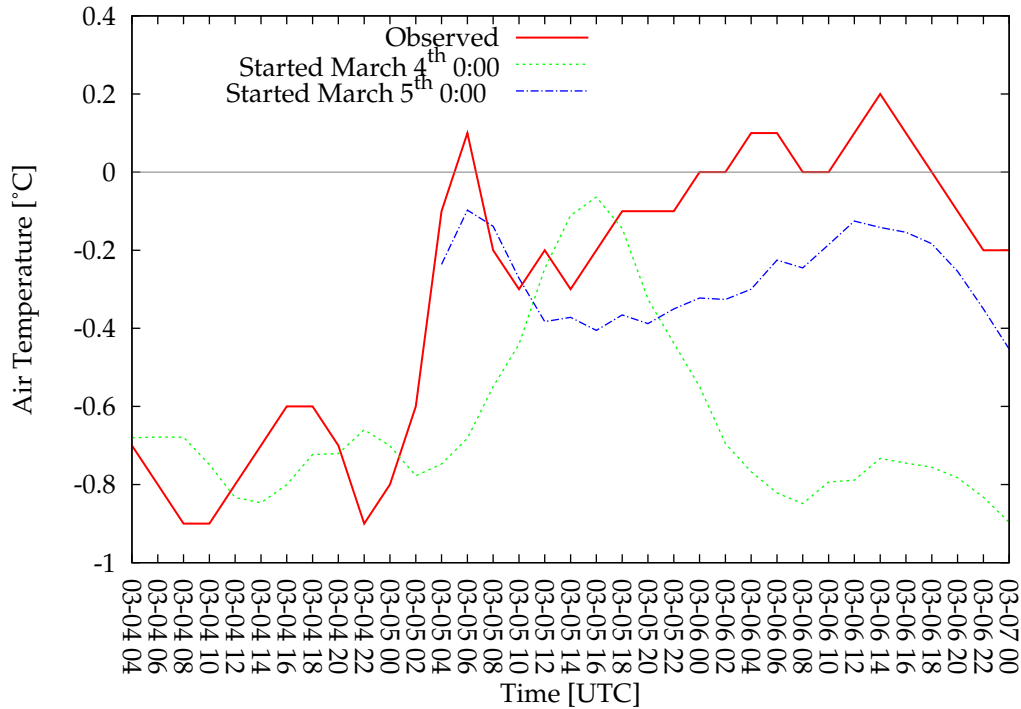


Figure 13: Observed surface air temperature at Bonavista and temperature modelled with WRF at 2 m AGL for simulations started on March 4 and 5 0:00 UTC.

The amounts of total precipitation observed on March 5 and 6 are compared to the values provided by the NWP model in Tables 12 and 13. The tables also evaluate the measured and simulated amounts in terms of MAE, across all meteorological stations. At Environment Canada stations, the climate day at first order or primary observing sites is defined by the 24-hour period ending at 6:00 UTC. However, at volunteer observing sites, the standard rain gauges are read once a day at approximately 8 am local time, which is 11:30 UTC. For consistency, the simulated daily precipitation totals were taken either at 6:00 UTC or at 11:30 UTC depending on the type of station.

The largest errors appear at the Terra Nova station, which reported the highest amount of precipitation on both days. The model's tendency to underestimate total precipitation could be caused by the complex terrain sur-

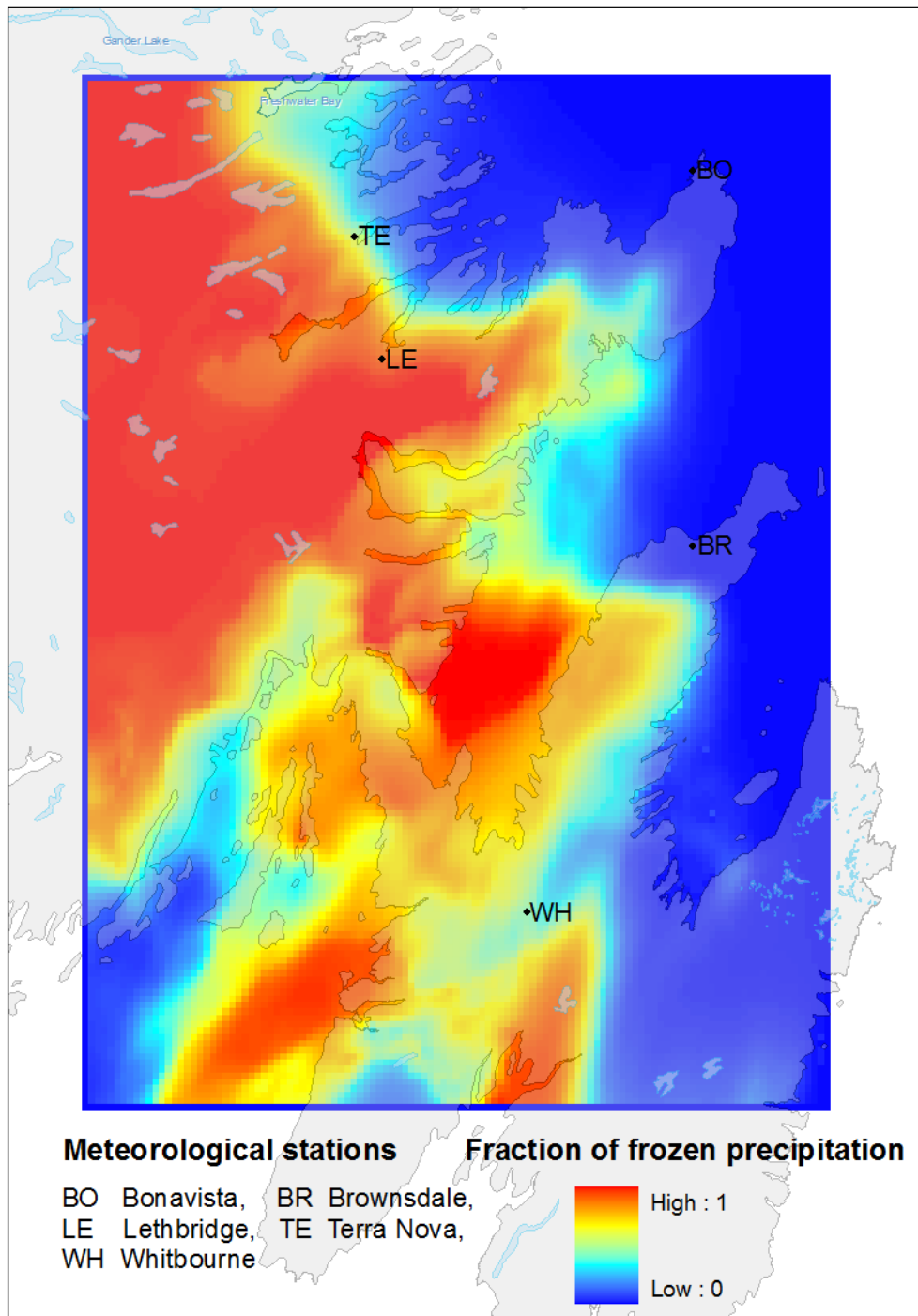


Figure 14: Fraction of frozen precipitation on March 6 0:00 UTC as simulated on March 5 0:00 UTC.

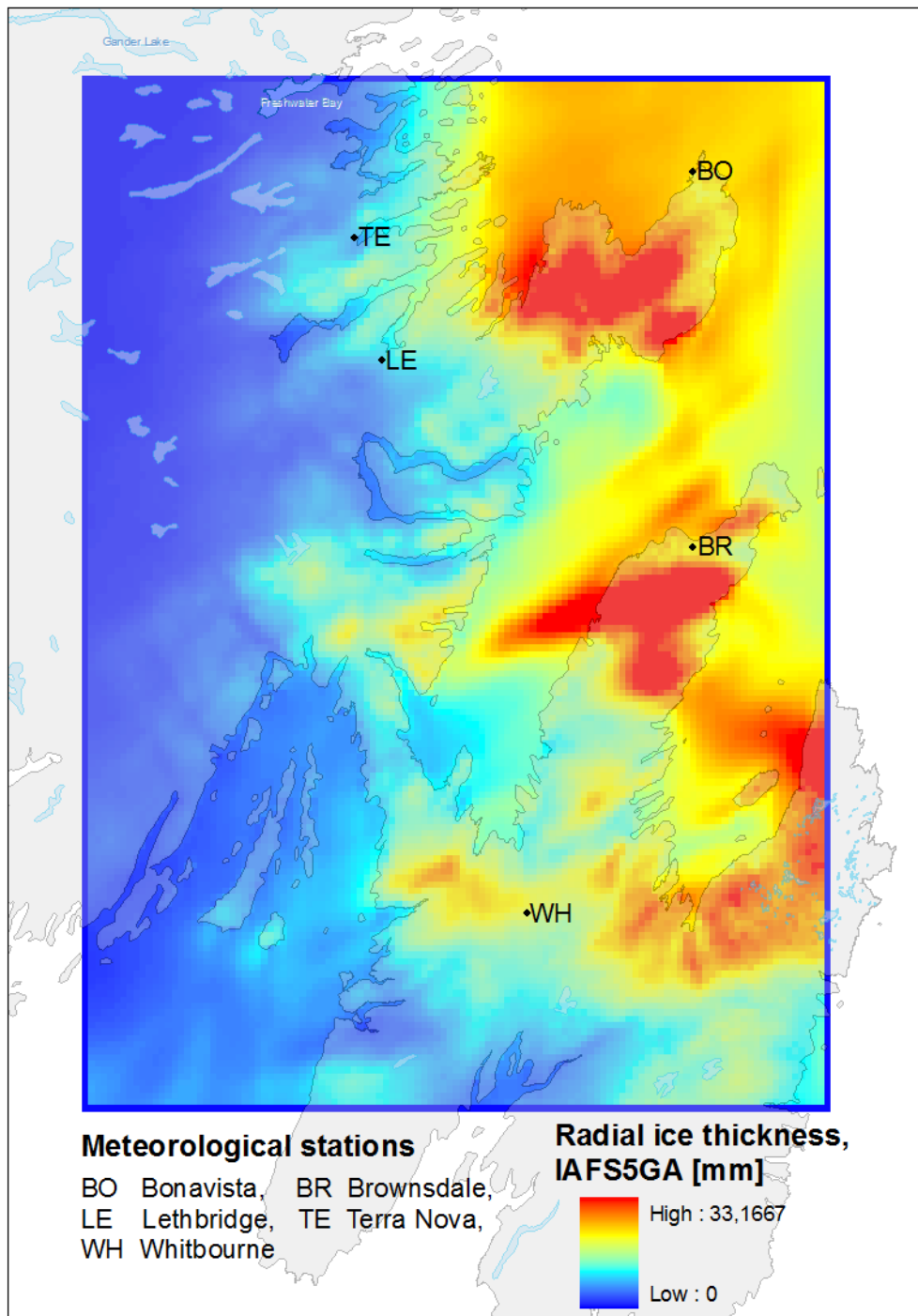


Figure 15: Cumulative radial equivalent ice thickness from March 5 0:00 UTC to March 8 0:00 UTC, as calculated with the optimized IAFS algorithm; simulation started on March 5 0:00 UTC.

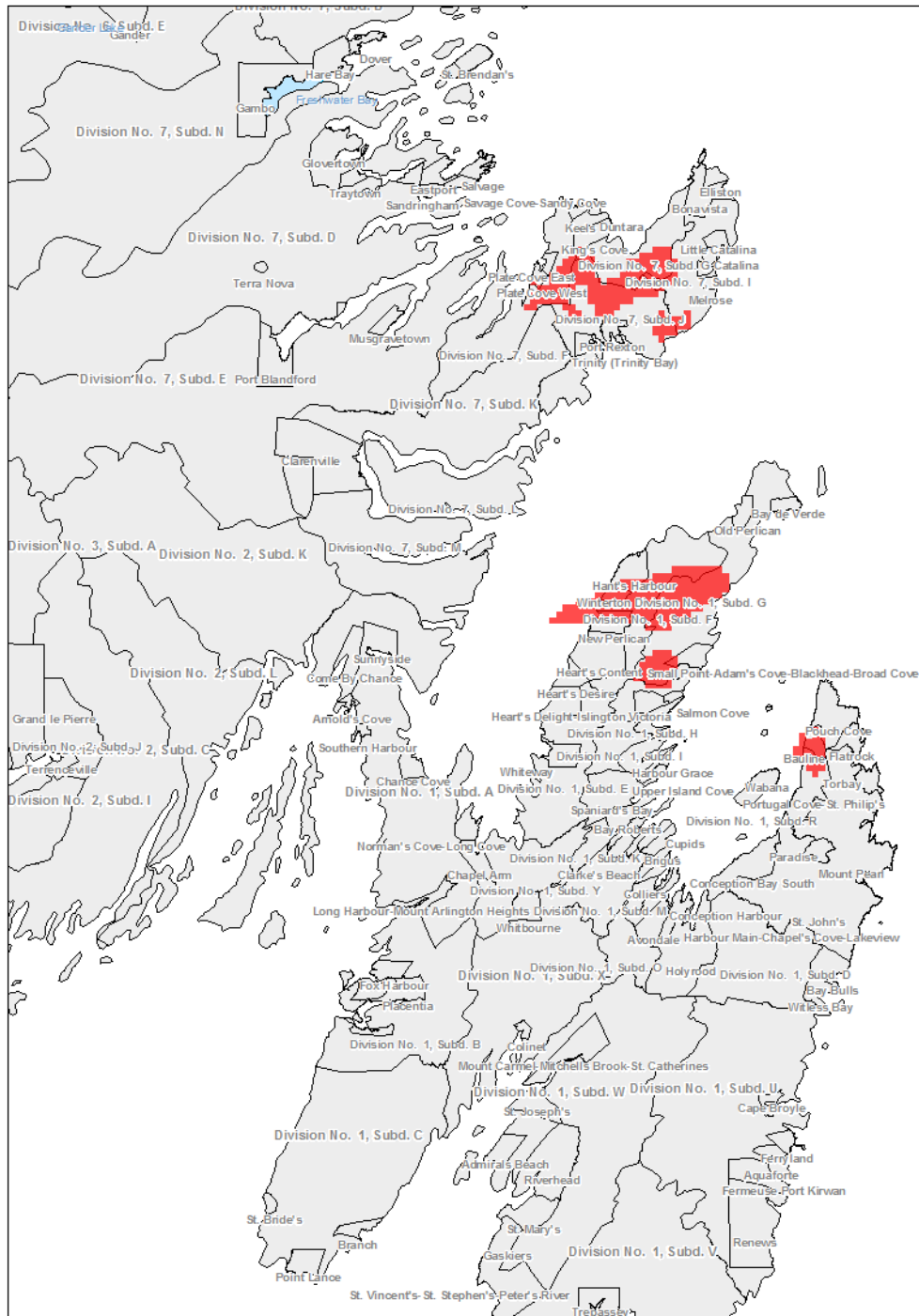


Figure 16: Radial equivalent ice thickness [mm] accumulation over 19 mm, overlaid on a map of Newfoundland municipalities, for March 5 0:00 UTC - March 8 0:00 UTC as calculated with the optimized IAFS algorithm; simulation initialized on March 5 0:00 UTC.

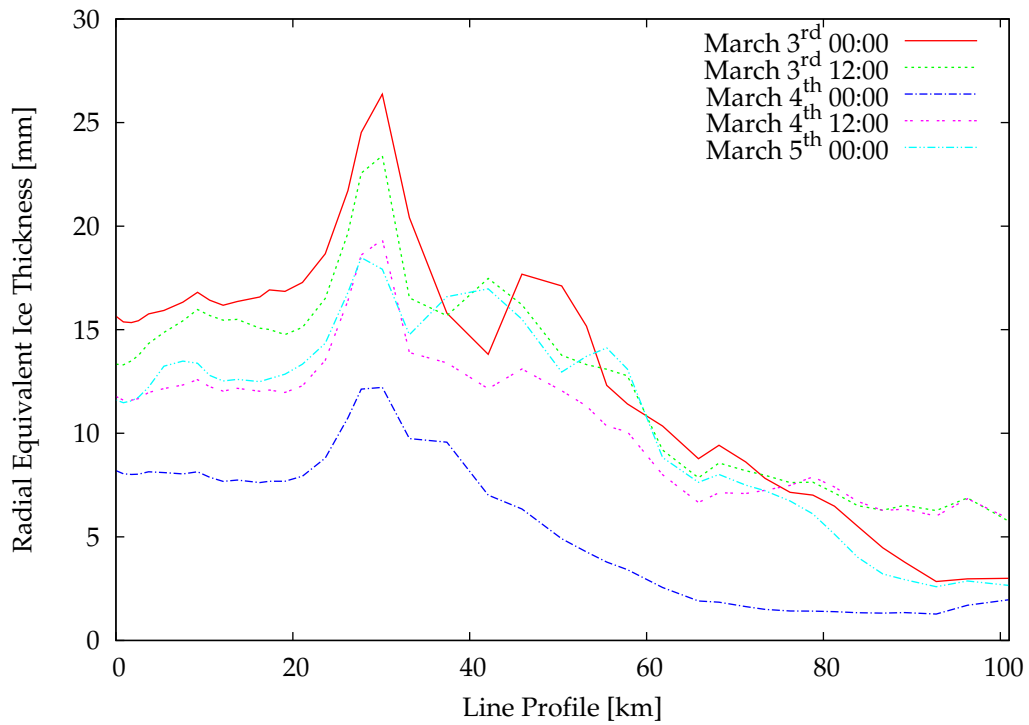


Figure 17: Radial equivalent ice thickness [mm] accumulated on the Bonavista power line over the entire event, as calculated with the optimized IAFS algorithm, for simulations initialized between March 3 0:00 UTC and March 5 0:00 UTC (North to South).

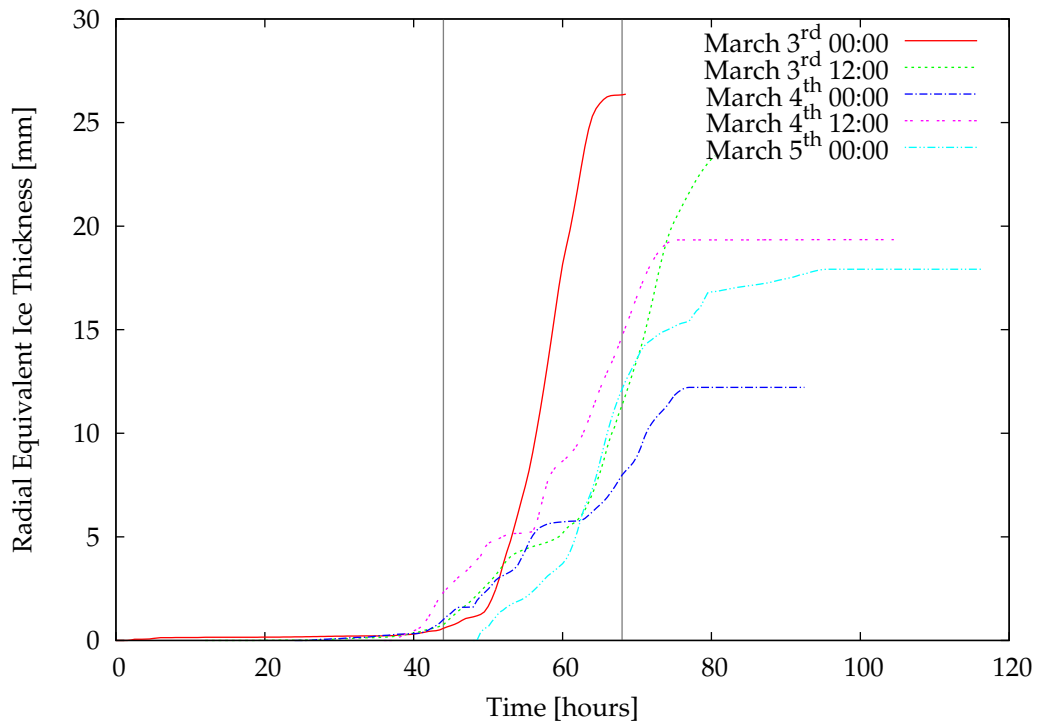


Figure 18: Radial equivalent ice thickness [mm] accumulated at the most exposed point on the Bonavista power line, as calculated with the optimized IAFS algorithm, for forecasts initialized between March 3 0:00 UTC and March 5 0:00 UTC; time in hours after March 3 0:00 UTC.

rounding the station, which is not well resolved at the spatial resolution used. The MAE generally decreases with a shorter forecasting horizon, with one insignificant exception, namely the last simulation for March 5. The model precipitation field, shown in Figure 11, appears to be flattened compared to the observational field, with smaller observed values overestimated by the model and vice versa. Hence, it appears that the model precipitation is underestimated at the most exposed sites. Nevertheless, the maximum total model precipitation (82.2 mm) corresponds well with the maximum total observed precipitation (88.8 mm). Given the patchiness of the model precipitation field, it is possible that some of the local station error may arise from erroneous positioning of the precipitation maxima in the model.

The meteorological station in Bonavista belongs to the network of synoptic stations, and thus precipitation data are available at 6-hour intervals. The comparison of the model and observations is shown in Figure 12. The data are presented as cumulative values starting at 0:00 UTC on March 4. The precipitation graphs for model runs started later than this are initialized with precipitation values observed at their onset. The simulation started closest to the beginning of the icing event is significantly more accurate than the earlier ones. On average, the total model precipitation was about 60% of the observed total precipitation.

For wind speed and air temperature, the only meteorological station that provides hourly data is Bonavista. However, the anemometer was apparently frozen during the main icing event, and so the wind speed data are missing during that period, preventing verification. The modelled 10 m wind speed at the location of the Bonavista weather station increased from about $11 \text{ m}\cdot\text{s}^{-1}$ to about $16 \text{ m}\cdot\text{s}^{-1}$ at the height of the storm and then declined to near $15 \text{ m}\cdot\text{s}^{-1}$ at

the end of the freezing rain. Peak wind speeds as high as $23 \text{ m}\cdot\text{s}^{-1}$ in the model occurred offshore and along Trinity Bay, Placentia Bay and Conception Bay.

The wind direction was predominantly NNW, coinciding with the longitudinal axes of these bays. Since the maximum model precipitation rate was only a few $\text{mm}\cdot\text{h}^{-1}$, the strong winds made a very substantial contribution to the overall icing rate in the model. They may also have contributed significantly to the overall load on the lines, although this study did not attempt to calculate the wind load. Air temperature observations are available, and their comparison with modelled values from two simulation runs can be found in Figure 13. The first run was initialized at 0:00 UTC on March 4, well before the event started. The resulting simulated temperatures are significantly lower than observed in the second part of the event, and the peaks in the time series are also shifted by about 6-10 hours. The simulation initialized at 0:00 UTC on March 5 performed much better, with no time shifts and errors of $0.3 \text{ }^{\circ}\text{C}$ or less.

The enhanced IAFS algorithm, whose optimization was described in the previous section of this chapter, was applied throughout the domain to calculate the glaze ice accumulation due to freezing rain, based on the values that were derived from the outputs of the WRF model. The results of the simulation initiated at 0:00 UTC on March 5 are shown in Figure 15. The most affected areas, the Bonavista Peninsula and Conception Bay North, are well captured by the model. The maximum model radial equivalent ice thickness exceeds 33 mm. This value is lower than values reported in the media (up to 60 mm), but it is important to note that the total precipitation is underesti-

mated by a similar factor. It is also possible that values reported in the media are exaggerated because of icicle formation and ice accretion asymmetry.

This affected area of eastern Newfoundland belongs to the severe icing category according to the overhead systems design standard [89], and the lines in this category are supposed to be designed for 19 mm of radial equivalent ice thickness. The spatial extent of the area with simulated radial equivalent ice thickness exceeding 19 mm is overlaid on a map of Newfoundland municipalities in Figure 16. All three regions with reported heavy damage on power lines, the Bonavista Peninsula, the northern Avalon Peninsula and Conception Bay North, contain simulated ice loads exceeding the design threshold.

Figure 17 shows the radial equivalent ice thickness along the main transmission line on the Bonavista Peninsula (the position of the line is shown in Figure 10). The values at the beginning of the profile, corresponding to the northern part of the line, do not change because the line follows the coast at relatively low elevations. Further along, the line crosses an exposed area, which corresponds to the peak of the simulated icing load. The icing load then decreases toward the interior of the island. The largest icing loads are simulated for the longest forecast horizon, initialized on March 3. The run initialized at 0:00 UTC on March 4 (forecast horizon of approximately 40 hours relative to the main event) produces smaller loads than the other runs. However, all forecasts would be useful in alerting the power utilities about the approaching storm, because they predict maximum ice loads approaching or exceeding the design limit.

Time series of radial equivalent ice thickness at the point with maximal values are shown in Figure 18. The simulation initialized on March 3 at 0:00 UTC produced an earlier onset of the icing than the other simulations,

by about 10 hours. The simulations with later starts agree better with the observation that freezing rain was reported throughout March 5. The timing and duration of the storm are consistent with reports from Environment Canada. For the Bonavista peninsula, the report states that, "The precipitation fell mainly as freezing rain overnight Thursday and all day Friday". This time period corresponds, approximately, to the time window from 44 to 68 hrs in Figure 18.

3.5 SUMMARY

This chapter presented a novel approach to tuning parameters of IAFS using Evolutionary Computing (EC). The system aims to accurately forecast the amount of ice accumulated on structures during periods of freezing rain, using forecast data obtained from a high resolution, mesoscale NWP model. It relies on a fuzzy engagement function to determine when to apply the ice accretion model and to what degree, based upon a set of four operational parameters.

The modified IAFS has been successfully trained and tested using data collected from twenty ASOS weather observing stations during eight ice storms of various severity that occurred in the Southeastern US between 2002 and 2008. The improved IAFS offers a substantial increase in accuracy over SM and the unoptimized IAFS.

The results show a significant improvement in consistency, accuracy, and skill of the optimized IAFS. The methodology described is not limited to ice

accretion modelling. It provides a general approach for setting operational parameters of data processing algorithms in order to achieve interoperability of NWP models with add-on applications based on empirical observations.

Using the optimized IAFS in simulated true forecast operation showed very promising results. The duration and timing of the freezing rain event that occurred between the night of March 4 and the morning of March 6 was simulated well in all model runs. Total precipitation amounts in the model, however, differed by up to a factor of two from the observations. The accuracy of the model air temperature strongly depended on the forecast horizon, but it was acceptable for all simulation runs. The simulated accretion loads were also compared to the design values for power delivery structures in the region. The results indicated that the simulated values exceeded design criteria in the areas of reported damage and power outages.

4

DYNAMIC THERMAL RATING

This chapter presents a significant enhancement to the IEEE Std. 738-2006 standard to improve its accuracy. It also provides guidance on the optimal configuration of a weather-based DTCR system. Finally, it presents solutions to support transmission industry in planning and maintaining power transmission lines.

4.1 PRECIPITATION COOLING OF OVERHEAD CONDUCTORS

In order to improve the accuracy of weather-based DTCR system, described in Section 2.1.5, this section proposes an extension to the generally adopted power line thermal model, described in Section 2.1.3.2. The increase in accuracy is achieved by the inclusion of conductor cooling caused by falling precipitation. To assess the real-world performance of the new model, it is used to predict the conductor temperature of an actual power line in operation. The modelled temperatures are compared with measurements from a sensor on a live transmission line. This section also presents an assess-

A version of this section has been published in [90]. I made a substantial contribution to the material of this publication. I also wrote a major portion of the published manuscript.

ment of the potential gains in transmission capacity that can be achieved by using the precipitation cooling thermal model. These potential gains in ampacity are assessed using real meteorological conditions recorded during actual precipitation events, rather than estimates based on average or typical meteorological/climatological conditions during periods of rain.

4.1.1 Enhanced Dynamic Thermal Model

The thermal model used by the IEEE Std. 738-2006 includes a number of simplifications. One of these is neglecting the cooling effect provided by precipitation falling on and then evaporating from the conductor. The standard even identifies this as a potential “major factor”; nevertheless, due to its sporadic nature along a span of transmission line, it was not included in the standard’s thermal model computation. As a result, conservative ampacity estimates are computed that ignore precipitation. For static ampacity ratings, the omission is fully justified; however, when incorporating the standard’s ampacity calculations for DTCR, potentially significant gains in available capacity are discarded.

To account for conductor cooling due to impinging precipitation, the heat loss arising from precipitation warming and subsequent evaporation is calculated as described below.

The convective heat transfer coefficient under non-precipitating conditions h is calculated. Since IEEE Std. 738-2006 does not explicitly define this coef-

ficient, it must be extracted from the convective cooling term. The standard provides three formulations. The first applies to natural convection,

$$q_{cn} = 0.0205\rho_f^{0.5} (1000D)^{0.75} (T_c - T_a)^{0.5}, \quad (28)$$

where q_{cn} [$\text{W}\cdot\text{m}^{-1}$] is the convective heat loss rate, D [m] is the conductor diameter, ρ_f [$\text{kg}\cdot\text{m}^{-3}$] is the density of air, T_a [K] is the air temperature, and T_c [K] is the conductor temperature. Since the time step between successive ampacity and conductor temperature calculations is typically greater than one minute, the cross-sectional conductor temperature is assumed to be uniform. This approximation is made as the internal time constant of the conductor is typically between 10–20 s [37].

Equations 29 and 30 apply to forced convection based on McAdam's equation [91]:

$$q_{c1} = \left[1.01 + 0.0372 \left(\frac{1000D\rho_f V_w}{\mu_f} \right)^{0.52} \right] \cdot k_f K_{angle} (T_c - T_a) \quad (29)$$

$$q_{c2} = 0.0119 \left(\frac{1000D\rho_f V_w}{\mu_f} \right)^{0.6} k_f K_{angle} (T_c - T_a), \quad (30)$$

where q_{c1} and q_{c2} [$\text{W}\cdot\text{m}^{-1}$] are the convective heat losses for low and high wind speeds, respectively, V_w [$\text{m}\cdot\text{s}^{-1}$] is the speed of the undisturbed air stream at the conductor, μ_f [$\text{Pa}\cdot\text{s}$] is the dynamic viscosity of air, and k_f [$\text{W}\cdot\text{m}^{-1}\cdot\text{K}^{-1}$] is the thermal conductivity of air at temperature T_{film} [K].

To compensate for reduced convective cooling under non-perpendicular airflow, the convective cooling is multiplied by a compensating factor K_{angle} :

$$K_{angle} = 1.194 - \sin(\beta) - 0.194 \cos(2\beta) + 0.368 \sin(2\beta), \quad (31)$$

where β is the angle between the wind direction and a plane perpendicular to the axis of the conductor.

The formula for q_{c1} is valid at low speeds (i.e., for small values of the Reynolds number) while q_{c2} is valid at high wind speeds. Both of these IEEE standard values are computed and the larger of the two is used in subsequent heat transfer equations. As a result of this approach, a first order discontinuity in the convective heat transfer coefficient is avoided, although there is still a second order discontinuity (in the slope of the curve).

The thermal conductivity of air is calculated using the formulation provided by IEEE Std. 738-2006,

$$\begin{aligned} k_f = & 2.424 \times 10^{-2} \\ & + 7.477 \times 10^{-5} \cdot (T_{\text{film}} - 273.15) \\ & - 4.407 \times 10^{-9} \cdot (T_{\text{film}} - 273.15)^2. \end{aligned} \quad (32)$$

T_{film} is calculated as the average of the conductor and ambient air temperatures,

$$T_{\text{film}} = \frac{T_c + T_a}{2}. \quad (33)$$

To extract the implied heat transfer coefficient in the IEEE Std. 738-2006 formulation, the forced convection equations are compared with Newton's Law of Cooling [92],

$$\dot{Q} = hA_s\Delta T, \quad (34)$$

where \dot{Q} [W] is the heat transferred per unit time, A_s [m²] is the heat transfer area of the surface, h [W·m⁻²·K⁻¹] is the convective heat transfer coefficient and ΔT [K] is the temperature difference between the conductor surface and the ambient air stream. Hence, the heat transfer coefficient is calculated from

$$h = \frac{\max(q_{c1}, q_{c2})}{\pi \cdot D (T_c - T_a)}. \quad (35)$$

In order to calculate precipitation cooling, the flux of liquid impinging on the conductor must be determined. The mass flux of liquid precipitation is calculated by first estimating the airborne liquid water content from the precipitation rate [79],

$$w_r = 6.7 \times 10^{-5} P_r^{0.846}, \quad (36)$$

where w_r [kg·m⁻³] is the liquid water content of the precipitation in the form of rain, and P_r [mm·h⁻¹] is the precipitation rate.

If the precipitation is in the form of snow, the liquid water content in the air can be estimated using a power regression function fitted to observations of the equivalent liquid water content of snow flakes provided in [93],

$$w_s = 1.4 \times 10^{-4} P_r^{0.9165}, \quad (37)$$

where w_s [$\text{kg}\cdot\text{m}^{-3}$] is the liquid water content of the precipitation in the form of snow.

The formula used to calculate the liquid water content w in the precipitation cooling model is selected based on the falling precipitation type.

$$w = \begin{cases} w_r & \text{p-type} = \text{rain} \\ w_s & \text{p-type} = \text{snow} \end{cases}. \quad (38)$$

Equations 36 and 37 represent the typical amount of liquid water present in a unit volume of air containing falling precipitation, based on the expected distribution of hydrometeor size. Liquid water content of falling precipitation can also be obtained directly from NWP model output, thus avoiding regression function errors.

The liquid mass flux density m_{af} [$\text{kg}\cdot\text{m}^{-2}\cdot\text{h}^{-1}$] impinging onto the conductor is the vector sum of the downward and windblown mass flux. Since rain droplets are relatively large, the collision efficiency is assumed to be unity, i.e., all droplets moving toward the conductor impinge on its surface. Moreover, a collection efficiency of unity is assumed, i.e., all impinging liquid remains on the conductor and there is no splashing or shedding. This is based on the

assumption only a thin film of water forms on the surface of the conductor, and the water rapidly evaporates from it. Hence,

$$m_{af} = \sqrt{(0.001P_r \cdot \rho_w)^2 + (3600 \cdot V_w \cdot w)^2}, \quad (39)$$

where V_w [$\text{m} \cdot \text{s}^{-1}$] is the wind speed.

The mass flux rate of liquid water striking the exposed conductor surface is

$$m_a = \frac{m_{af} \cdot D}{3600}, \quad (40)$$

where m_a [$\text{kg} \cdot \text{s}^{-1} \cdot \text{m}^{-1}$] is the mass flux rate of water striking the conductor surface and D [m] is the diameter of the conductor.

The increased conductor perimeter from multiple strands forming the outer surface of the conductor is estimated to be

$$P_c = n_s \pi d_s \left(0.5 + \frac{1}{n_s} \right), \quad (41)$$

where P_c [m] is the conductor perimeter, d_s [m] is the strand diameter, and n_s is the number of strands in the outer layer of the conductor.

The evaporative mass flux m_e [$\text{kg} \cdot \text{s}^{-1} \cdot \text{m}^{-1}$] should the entire conductor surface be wetted, is

$$m_e = P_c \cdot \frac{hk}{c_p \rho_a} (e_c - \text{RH} \cdot e_a), \quad (42)$$

where k is 0.62, the ratio of the molecular weights of water vapour and dry air, e_c [Pa] is the saturation vapour pressure of water at the conductor temperature, e_a [Pa] is the saturation vapour pressure of water at the air temperature, p_a [Pa] is the ambient air pressure, c_p [$\text{J}\cdot\text{kg}^{-1}\cdot\text{K}^{-1}$] is the specific heat of air at constant pressure, and RH is the relative humidity expressed as a fraction in $[0, 1]$.

The saturation vapour pressure of water at a given temperature is calculated using the Antoine equation [94],

$$e_s(T) = 133.322 \cdot 10.0^{8.07131 - \frac{1730.63}{T - 39.724}}, \quad (43)$$

where e_s [Pa] is the saturation vapour pressure of water, and T [K] is the water temperature.

Should the mass flux from precipitation be less than the potential flux of water evaporating from the conductor surface when the entire conductor surface is covered in water, then the smaller flux is used,

$$m_c = \begin{cases} m_a & m_a < m_e \\ m_e & \text{otherwise} \end{cases}, \quad (44)$$

where m_c [$\text{kg}\cdot\text{s}^{-1}\cdot\text{m}^{-1}$] is the actual mass flux evaporating from the conductor surface.

The conductor may be heated to temperatures exceeding the boiling point of liquid water. The boiling point is first calculated using a formulation derived from the Clausius-Clapeyron equation [95],

$$T_b = \left[\frac{1}{373.12} - \frac{R \log(p_a \cdot 9.8692 \times 10^{-6})}{H} \right]^{-1}, \quad (45)$$

where T_b [K] is the boiling point, R [$\text{J}\cdot\text{K}^{-1}\cdot\text{mol}^{-1}$] is the universal gas constant, H [$\text{J}\cdot\text{mol}^{-1}$] is the enthalpy of vapourization of water, and p_a [Pa] is the air pressure.

The temperature at which the water evaporates is computed by taking the minimum of the conductor temperature and the boiling point temperature,

$$T_e = \min(T_c, T_b), \quad (46)$$

where T_e [K] is the evaporation temperature.

The precipitation heat loss due to evaporation is calculated as follows

$$q_e = m_c [L_e(T_e) + c_w \cdot (T_e - T_a)], \quad (47)$$

where L_e [$\text{J}\cdot\text{kg}^{-1}$] is the specific latent heat of evaporation of water, T_a [K] is the ambient air temperature, c_w [$\text{J}\cdot\text{kg}^{-1}\cdot\text{K}^{-1}$] is the specific heat capacity of liquid water, and q_e [$\text{W}\cdot\text{m}^{-1}$] is the evaporative heat loss.

When performing the above calculations on precipitation in the form of snow, the heat loss must also account for the latent heat of fusion and the

specific heat capacity of ice for ambient air temperatures below the freezing point of water. Hence the heat loss for snow precipitation is

$$q_e = m_c [L_e (T_e) + c_w (T_c - 273.15 \text{ K}) + L_f (273.15 \text{ K}) + c_i (273.15 \text{ K} - T_a)], \quad (48)$$

where L_f [$\text{J}\cdot\text{kg}^{-1}$] is the specific latent heat of fusion of water at 273.15 K, and c_i [$\text{J}\cdot\text{kg}^{-1}\cdot\text{K}^{-1}$] is the specific heat capacity of ice.

The specific latent heat of evaporation is calculated by using an empirical formula fitted to data provided in [96],

$$L_e (T_s) = 0.0000614342 (T_s - 273.15)^3 - 0.00158927 (T_s - 273.15)^2 + 2.36418 (T_s - 273.15) - 2500.79, \quad (49)$$

where T_s [K] is the water surface temperature.

The updated heat balance in the ampacity thermal model for steady-state and transient conditions, respectively, becomes

$$q_c + q_r + q_e = q_s + q_j, \quad (50)$$

$$q_c + q_r + q_e + mC_p \frac{dT_c}{dt} = q_s + q_j. \quad (51)$$

4.1.2 Available Measurements

To verify the precipitation cooling model, observational data were obtained from an industrial partner. The partner operates an on-site meteorological station and an on-conductor current and temperature sensor is installed on a live transmission line. The line thermal model was provided with the meteorological data from these instruments in order to calculate the conductor temperature. The calculated conductor temperature was then compared with the measured conductor temperature.

4.1.2.1 *Conductor*

The Indian Arm crossing transmission line is a 230 kV circuit that uses an Aluminium Alloy Conductor Steel-Reinforced (AACSR) conductor with the characteristics described in Table 14. Since the conductor was installed over 40 years ago, the coefficients of absorption and emissivity were set equal to those of a typical “old” conductor.

4.1.2.2 *Sensor Instruments*

The weather observations at the line location were made using an FTS Meteorological Monitoring station, depicted in Figure 19. This station has a number of automated instruments to measure ambient atmospheric conditions. These include a tipping bucket precipitation gauge, an ultrasonic wind speed anemometer, a thermistor ambient air temperature thermometer, a photo-diode solar pyrometer, a capacitive relative humidity sensor, and a solid-state transducer pressure sensor. Line temperature and line current

Table 14: Conductor type and physical parameters used to configure the IEEE Std. 738-2006 ampacity thermal model for the precipitation based conductor cooling study.

Description	Value
Material	AACSR
Strand Diameter	3.2258 mm
Overall Diameter	35.4838 mm
Number of Outer Strands	22
Coeff. of Emissivity	0.82
Coeff. of Absorption	0.91
Strand Heat Capacity	1095.9 J·m ⁻¹ ·K ⁻¹
Core Heat Capacity	1155.9 J·m ⁻¹ ·K ⁻¹
Resistance @ 25 °C	6.8471 × 10 ⁻⁵ Ω·m ⁻¹
Resistance @ 75 °C	8.0052 × 10 ⁻⁵ Ω·m ⁻¹
Ground Elevation	105 m (at sensor site)
Line Elevation	60.7 m (varies)
Line Bearing	133.2°N

Table 15: Description of the Artech SMT sensor unit installed at the Indian Arm crossing.

Sensor	Value
Min Current	100 A
Max Current	1500 A
Max Temperature	150 °C

were measured by a clamped-on Artech SMT sensor unit, depicted in Figure 20. Its measuring limits are described in Table 15.

4.1.2.3 Preprocessing

Initialization data for the thermal model include both meteorological observations and line current and temperature measurements. Before the data could be used to predict the conductor temperature to verify the precipitation cooling model, it required substantial pre-processing. Sensor measurement records for the period between February and December 2010 were obtained and the relevant variables for the thermal model were extracted. Obvious

4.1 PRECIPITATION COOLING OF OVERHEAD CONDUCTORS



Figure 19: The FTS Meteorological Station installed at the BC Indian Arm crossing transmission line. Photo courtesy of BC Hydro R&D.

Table 16: Description of the sensors present in the FTS meteorological station installed at the Indian Arm crossing.

Sensor	Measurement	Range		Resolution	Accuracy
		Lower	Upper		
RG-T-TRI	Total accumulated rainfall	0.00 mm	16645.89 mm	0.254 mm	$\pm 2\%$ at 50 mm·h ⁻¹
SDI-UWS-GILL-2	10 min average wind speed	0 ms ⁻¹	60 ms ⁻¹	0.01 m s ⁻¹	$\pm 2\%$
THS-3-1	10 min average wind direction	0°	359°	1°	$\pm 3\%$
	Air temperature	-40 °C	60 °C	0.1 °C	± 0.1 °C
	Relative humidity	0%	100%	1%	$\pm 2\%$
SDI-B1-S	Barometric pressure	600 hPa	1100 hPa	0.01 hPa	± 0.5 hPa
SDI-SR-PYR	Solar Radiation	0 Wm ⁻²	1800 Wm ⁻²	1 Wm ⁻²	$\pm 5\%$

4.1 PRECIPITATION COOLING OF OVERHEAD CONDUCTORS



Figure 20: The Artech SMT sensor unit clamped onto the BC Indian Arm crossing transmission line. Photo courtesy of BC Hydro R&D.

4.1 PRECIPITATION COOLING OF OVERHEAD CONDUCTORS

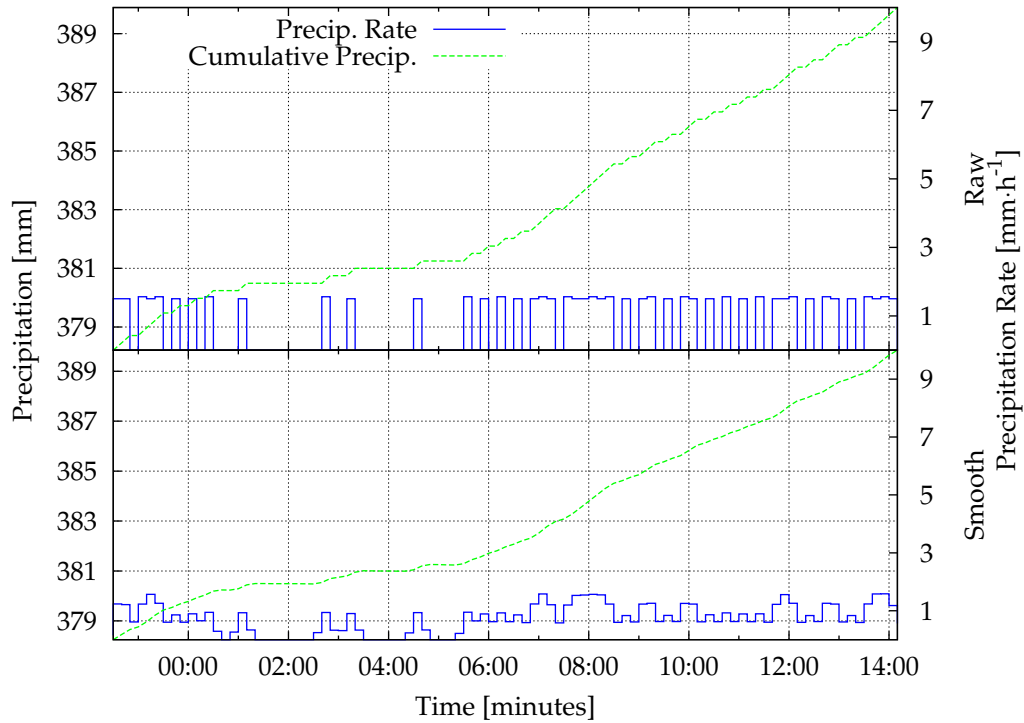


Figure 21: Observed cumulative precipitation and precipitation rate before and after smoothing (February 24, 2010).

sensor errors were eliminated. This included current and temperature readings from the SMT sensor when the line current was below the minimum required for correct operation of the unit. Instances that substantially deviated from the norm were discarded from the comparison as outliers. Very short periods of missing data (i.e. less than one hour) were filled in with the most recent observations and their duration was adjusted accordingly. To reduce the impact of the resolution of the tipping bucket precipitation gauge, spline smoothing of cumulative precipitation observations was performed. This removed discrete steps in the precipitation record. The impact of this procedure on cumulative precipitation amount and precipitation rate is illustrated in Figure 21.

4.1.3 Evaluation

4.1.3.1 *Results*

The line thermal model based on IEEE Std. 738-2006 was used to compute line temperature using the observed meteorological conditions from the FTS station and the line current measured by the SMT sensor. To verify the real-world performance of the precipitation cooling model, two sets of tests were performed. The first set involved quantitative statistical analysis of the model temperature and the temperature sensor readings. The measured line temperature was compared with the modelled temperature using the IEEE Std. 738-2006 model with (PC) and without (NoPC) the precipitation cooling extension. The calculated values were compared against temperature readings made by the SMT sensor and three error measures were computed. These are presented in Table 17. The table illustrates the accuracy of the two model temperature estimates for a range of precipitation rates observed, from light showers to heavy rainfall events.

The second set of tests involved a qualitative analysis of selected rainstorm events occurring during the period with available data. These included a visual assessment of the correlation between predicted and measured line temperatures. To illustrate the relative performances of the precipitation cooling model and the standard thermal model, three separate rain-fall events are presented. All three events incurred substantial total precipitation and produced sustained periods of continuous precipitation. The selected periods did not contain any missing sensor data. Sample time series of observed and modelled line temperatures are shown in Figures 22, 23 and 24. These

Table 17: Mean Absolute Error (MAE), Mean Error (ME), and Root Mean Square Error (RMSE) of the line thermal model with and without the precipitation cooling extension.

Precipitation Range [mm·h ⁻¹]	Number of Samples	IEEE 738 Thermal Model			With Precipitation Extension		
		MAE	ME	RMSE	MAE	ME	RMSE
All Data	17981	1.29	0.97	1.83	1.23	0.89	1.79
(0:1]	677	1.24	1.20	1.45	0.46	0.16	0.64
(1:2]	309	1.39	1.35	1.57	0.52	0.27	0.72
(2:3]	167	1.29	1.28	1.46	0.50	0.34	0.73
(3:4]	119	1.29	1.28	1.45	0.47	0.33	0.64
(4:5]	71	1.42	1.42	1.61	0.38	0.24	0.54
Only Precip.	1427	1.29	1.26	1.48	0.47	0.24	0.66
No Precip.	16554	1.30	0.94	1.86	1.30	0.94	1.86

figures show a significant improvement in the fit of the modelled conductor temperature using the enhanced precipitation cooling thermal model to the measured conductor temperature, over the IEEE Std. 738-2006 model.

For periods with recorded precipitation, the modelled conductor temperature is within a fraction of a degree of the measured conductor temperature. It is important to keep in mind that the small difference in temperature between the two models is attributed to the overall light loading of the transmission line at the Indian Arm crossing. Should the transmission line be more heavily loaded, the potential temperature difference between the IEEE Std. 738-2006 and the actual line temperature can be substantially greater during periods of precipitation.

In order to estimate how much additional capacity precipitation cooling could provide, the ampacity of the conductor was determined using the observed weather conditions. The current needed to raise the conductor temperature to 75 °C was computed using the IEEE Std. 738-2006 model and the

4.1 PRECIPITATION COOLING OF OVERHEAD CONDUCTORS

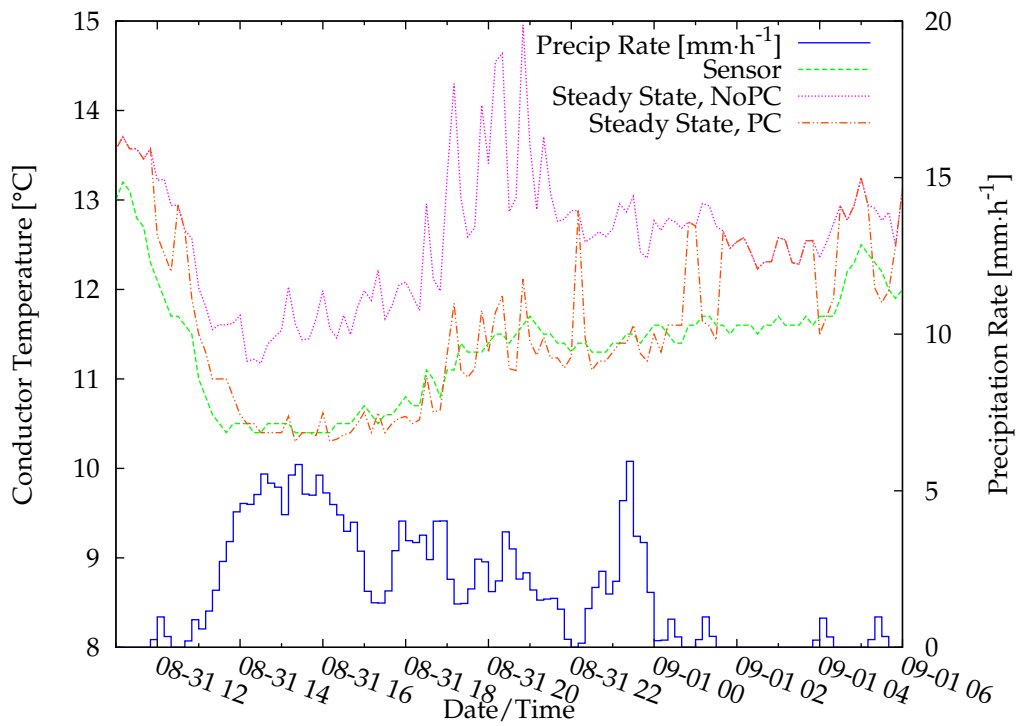


Figure 22: Observed and modelled conductor temperature for the Indian Arm Crossing transmission line, for the period between August 31 and September 1, 2010.

4.1 PRECIPITATION COOLING OF OVERHEAD CONDUCTORS

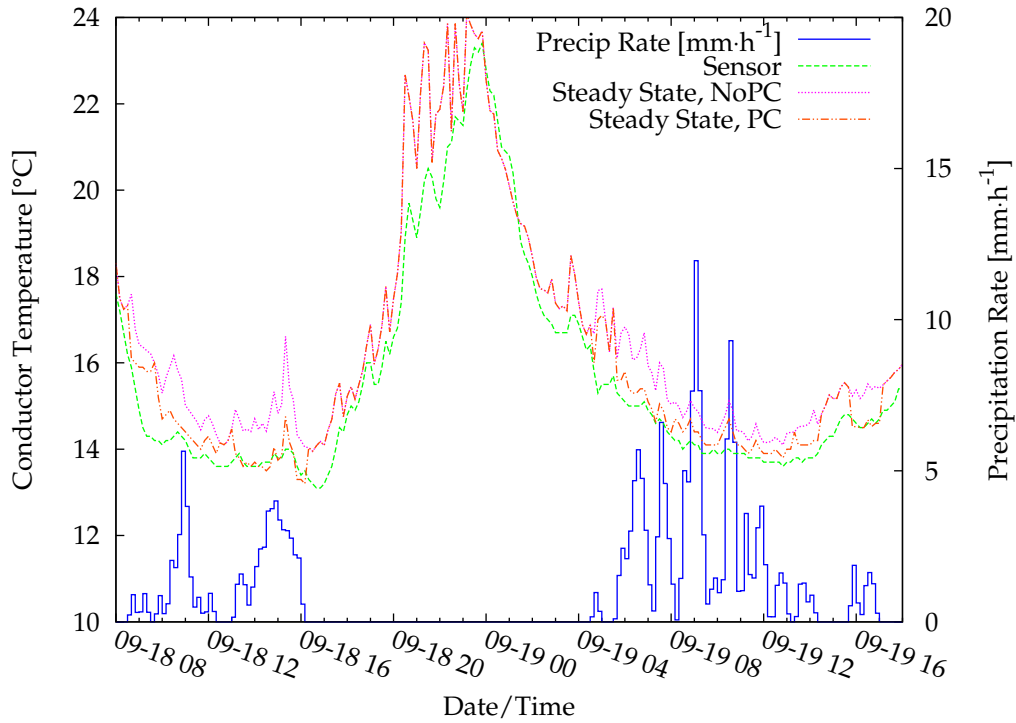


Figure 23: Observed and modelled conductor temperature for the Indian Arm Crossing transmission line, for the period between September 18 and 19, 2010.

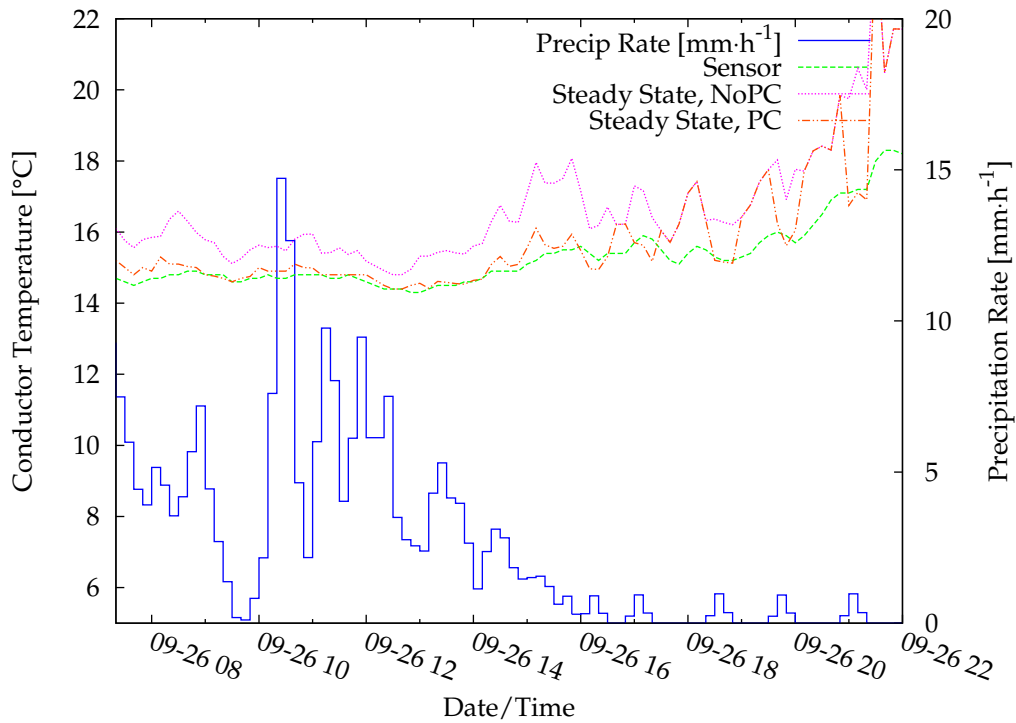


Figure 24: Observed and modelled conductor temperature for the Indian Arm Crossing transmission line, for September 26, 2010.

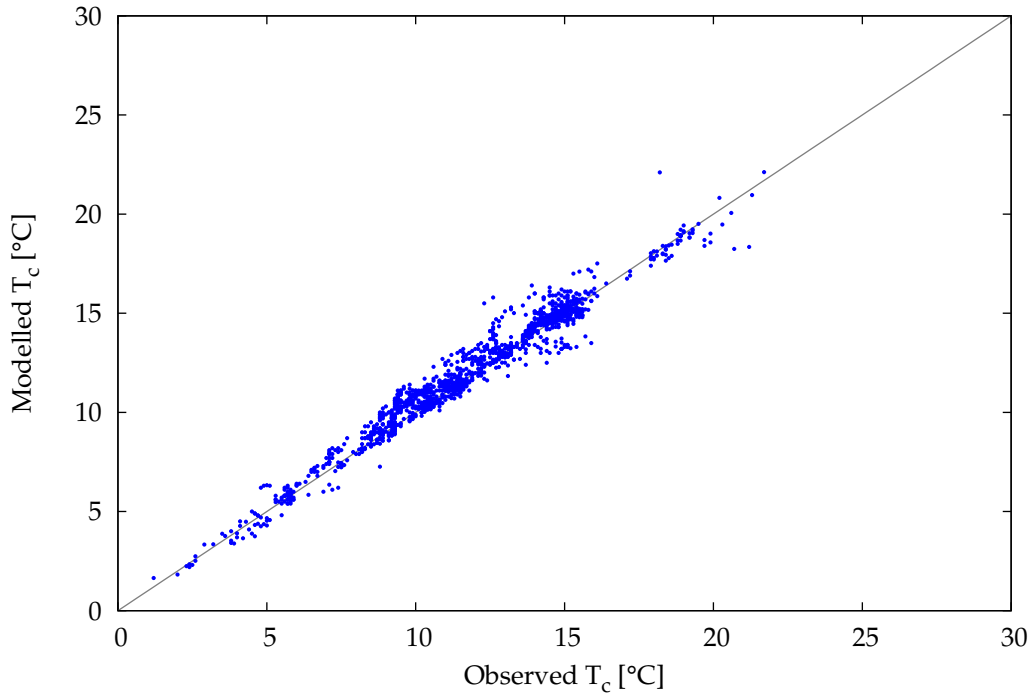


Figure 25: Observed and modelled conductor temperature using the precipitation cooling model, for all data samples with non-zero precipitation rate.

model with the precipitation cooling extension. The gain in ampacity is taken to be the difference in required current between the two models. Assuming a power factor of 0.9, the modelled line capacity gain with increasing precipitation rate is illustrated in Figure 26. The frequency of occurrence of the gain in capacity for the period of available data is presented in Figure 27. To illustrate the gain in ampacity during a single rainfall event, a time series of the line ampacity estimate calculated by the two models is shown in Figure 28.

4.1.3.2 Discussion

The precipitation cooling model showed a substantial improvement in accuracy of calculated line temperatures, compared with the temperatures calculated by the IEEE Std. 738-2006 model without the precipitation cooling extension. In all cases, the precipitation cooling model decreases the simple

4.1 PRECIPITATION COOLING OF OVERHEAD CONDUCTORS

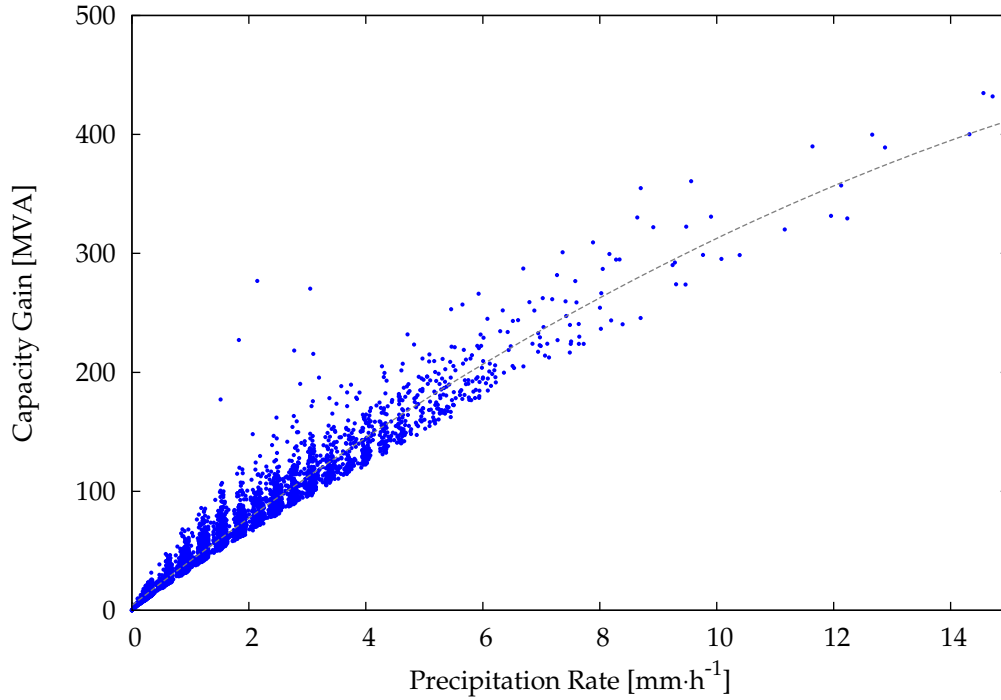


Figure 26: Increase in computed line capacity, as estimated using the precipitation cooling extension.

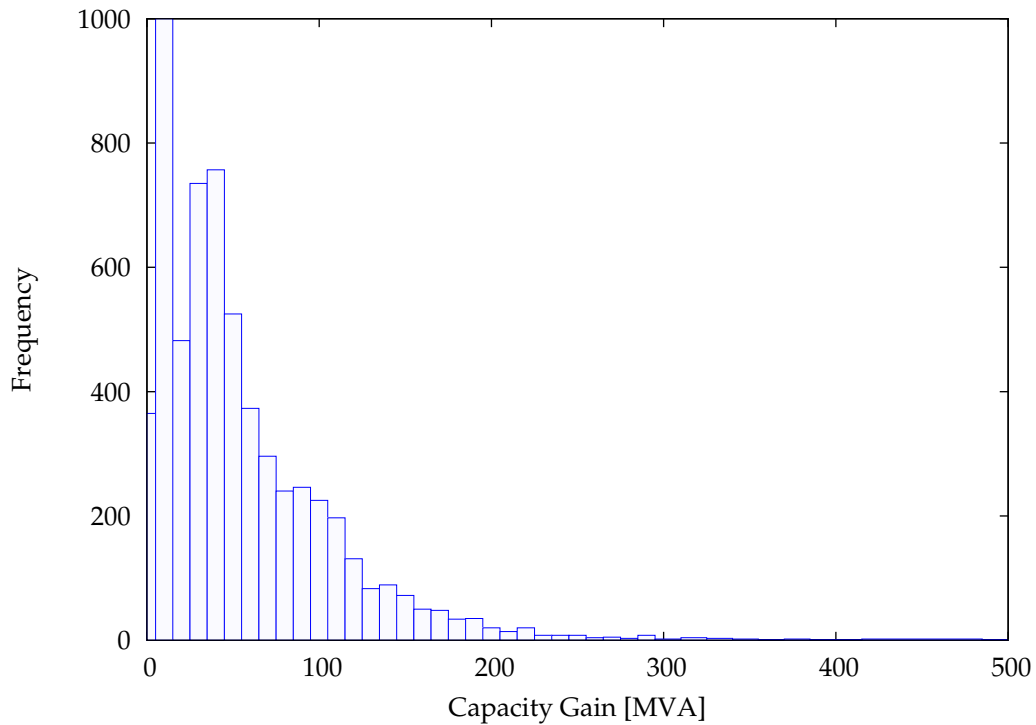


Figure 27: Increase in computed line capacity, as estimated using the precipitation cooling extension.

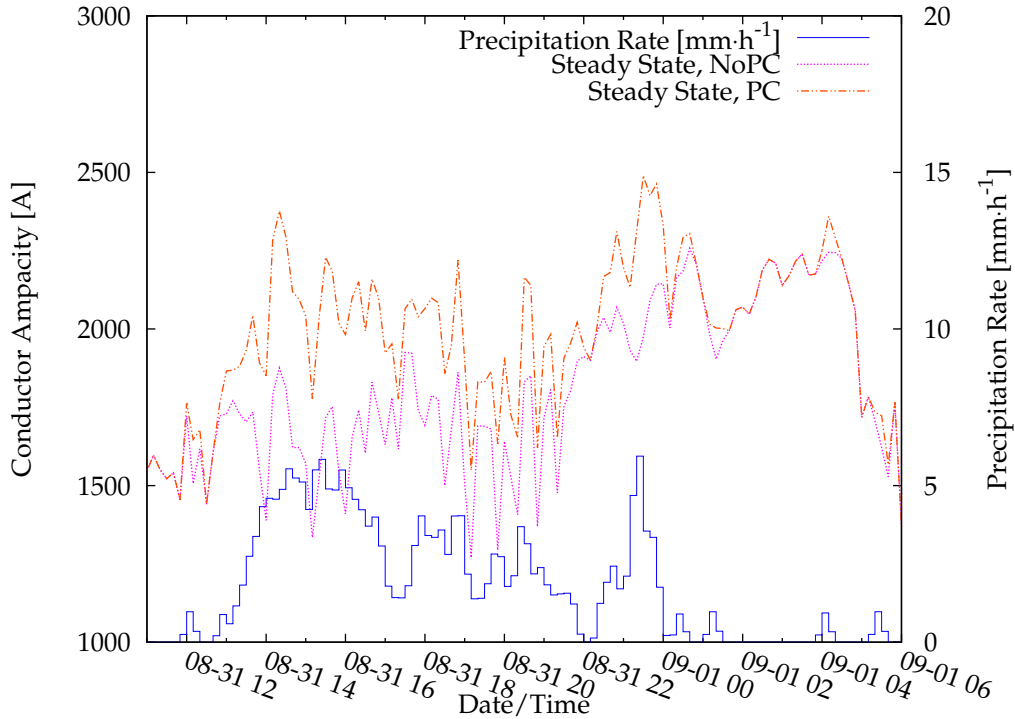


Figure 28: Indian Arm Crossing estimated transmission line ampacity, for the period between August 31 and September 1, 2010.

bias of the predicted line temperature. Very small precipitation rates (under $1 \text{ mm}\cdot\text{h}^{-1}$) are almost unbiased, while higher precipitation rates show a significant decrease in the tendency of the original IEEE Std. 738-2006 model to over-predict the line temperature. When considering samples with precipitation, a decrease in bias of $1.02 \text{ }^\circ\text{C}$ is achieved. This results in a mean error of $0.24 \text{ }^\circ\text{C}$. To verify that the results are statistically significant, a paired t-test was performed on the line temperatures estimated by the two models for samples with precipitation. The resulting P-value of 6.9×10^{-308} confirms that the line temperatures modelled with the precipitation cooling model are indeed statistically different from the original IEEE Std. 738-2006 model.

The scatter plot in Figure 25 confirms that the model is unbiased. In all cases the MAE and RMSE of the modelled conductor temperature decreased

when line cooling by precipitation was accounted for. The significant differences increase with increasing precipitation rate. This occurs because the contribution of precipitation cooling increases with precipitation rate and cooling by precipitation is not accounted for in the IEEE Std. 738-2006 model.

Time series graphs of the modelled and measured conductor temperature, along with the precipitation rate, illustrate the reliance of the thermal model on accurate meteorological variables. The precipitation rate is calculated from the accumulated precipitation in the rain gauge, and its accuracy is limited by the relatively coarse resolution of the measurements. The sensing instrument uses a tipping bucket that requires a minimum of 0.25 mm of precipitation to accumulate before it is registered. Unfortunately, smoothing of this input cannot compensate for periods of very low precipitation rates which require a prolonged time period until an increase in collected precipitation is observed.

Ampacity calculations using the thermal model with precipitation cooling show the potential for a substantial amount of additional capacity. The same precipitation rate can be accompanied by a variety of alternative meteorological conditions, such as different ambient air temperature and wind speed. This causes a spread in line capacity values for a given precipitation rate (Figure 26). For the extracted data with any precipitation, the average ampacity gain for the transmission line was 163.2 A with a standard deviation of 139.6 A. Assuming a power factor of 0.9, this translates into an average capacity gain of 58.5 MVA with a standard deviation of 50.0 MVA.

The increase in line capacity with precipitation rate can be seen clearly in Figure 26. The overall trend shows a diminishing return on the capacity gain as the precipitation rate increases. This can be attributed partly to the maximum evaporation rate of the water on the conductor surface. Further-

more, it is clear that during the observed period the precipitation rate rarely exceeded $7 \text{ mm}\cdot\text{h}^{-1}$ at the test site. This precipitation rate corresponds to a capacity gain of just over 200 MVA. In most instances, the gain during periods of precipitation will be less than 100 MVA. This is a very substantial amount of additional capacity.

Additional cooling of the conductor not represented by the precipitation cooling model can potentially be explained as follows. Due to the slope of the installed conductor, additional water is present on the conductor surface where the sensor is clamped onto the line. Water may run down the conductor surface and cool lower sections of the conductor more than sections near the top of the towers. Further cooling may result from an increased heat transfer coefficient not accounted for in the extracted heat coefficient variable. Complex boundary layer effects due to impingement and splashing are not accounted for in the model. These potential sources of cooling would require the installation on the transmission line of more elaborate sensor equipment such as a high speed camera. Such equipment would provide visual evidence of how impinging water behaves as it hits the conductor under various atmospheric conditions. Even without these factors, the current model provides sufficient representation of the evaporative cooling process and accurate line temperature estimates (less than one degree Celsius error).

Verification of the precipitation cooling model during winter conditions was not possible due to lack of sensor observations. Equations for the liquid water content used in the model were based on published experiments; however, the assumption that collection efficiency is unity may need to be revised. Unfortunately, observations necessary to perform such a verification are very scarce, and they were not available. The data obtained from the industry part-

ner was collected at a location where precipitation is predominantly in the form of rain. This section of transmission line is critical to the power utility due to line sag constraints, and thus contains a number of installed instruments. Other sections of the transmission network do lie in areas with colder regimes, but these do not have any sensors installed that could be used to further verify the model.

4.2 OPTIMAL DTCR CONFIGURATION

To take advantage of using NWP systems to deliver DTCR forecasts, a large number of calculations must be performed simultaneously, for a number of points along a transmission corridor, and for a number of time horizons. The internal time step of high-resolution NWP models is usually on the order of tens of seconds. Although the required meteorological parameters could be output at this time scale, processing and storage of such a large amount of data would require an undue amount of computing resources. On the other hand, using meteorological variable values sampled every 30 or 60 minutes of simulation time may not be sufficient for DTCR calculations. To discover the optimal tradeoff, this section examines the effects of the time resolution of meteorological inputs on the accuracy of DTCR computations, and it provides recommendations for the optimal design and operation of weather-based DTCR systems.

A version of this section has been published in [97]. I made a substantial contribution to the content of this publication.

4.2.1 Sampling Interval Data

For a DTCR study, wind speed and temperature measurements should be made at a height above ground comparable to the height of transmission lines, and with a sampling interval as short as possible. However, data satisfying such requirements are relatively scarce. Measurements that satisfy these requirements are typically made for wind energy assessment purposes; consequently, they are carried out at windy sites. In contrast, thermally critical segments of transmission lines are usually located in areas with relatively low wind speeds. As a result, such measurements may not be representative for a typical power transmission line.

Nevertheless, assuming that the statistics of the wind speed are similar in both instances, data collected at wind energy sites can be safely used for the purposes of the following analysis. The validity of this assumption is confirmed by comparing the frequency distribution of the measurements to the shape of a Weibull distribution, as shown in Figure 29.

The measurements used for the simulations described in this paper were made at Dlouha Louka in the Ore Mountains, Czech Republic. This mountain range extends from southwest to northeast, along the border with Germany. The most frequent and strongest winds come from the west and northwest. The elevation of the site is 890 m above sea level, and the terrain opens to the south with an aspect of approximately 190° . The slope at the site is about 4° , and it increases to 32° down the hill. A view of the measurement site is shown in Figure 30.

The measurements were originally taken for wind energy assessment purposes, as this site is one of the windiest in the country. The long-term average

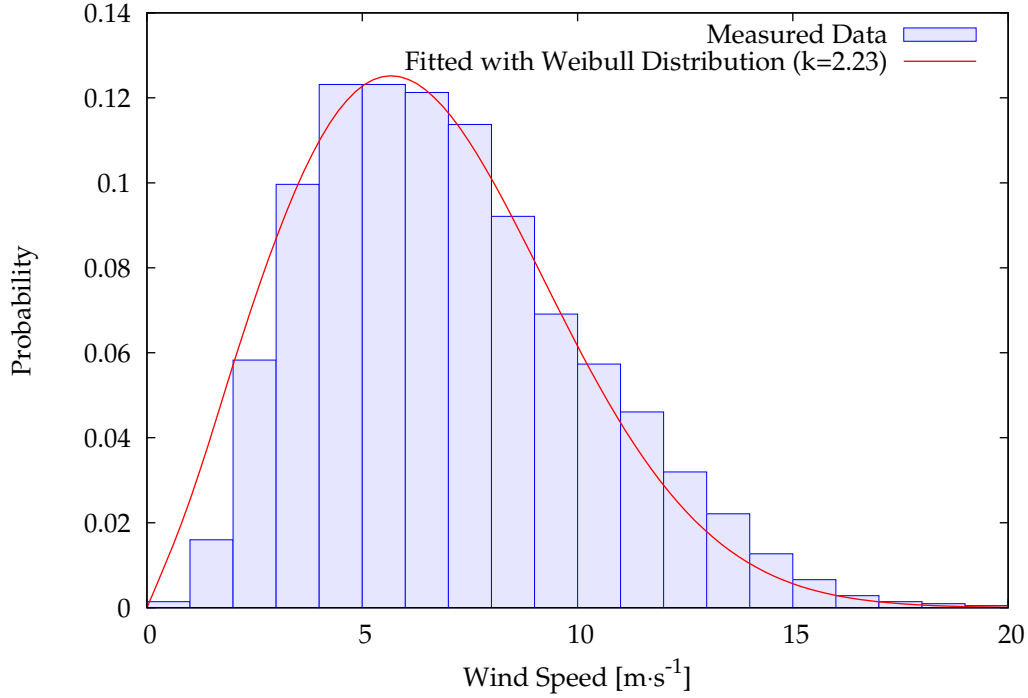


Figure 29: Normalized frequency distribution of the data used in the sampling interval study.

wind speed, in the period 1994 to 2004, was $7.04 \text{ m}\cdot\text{s}^{-1}$. The wind measurements used in this study were made at the top of the meteorological mast, 50 m above ground. The sensor used was an ultrasonic anemometer, METEK USA-1, which provides all three components of wind velocity and temperature. The data used for this study were collected during the period from June 18, 1999 to October 2, 1999. This covers the least windy and warmest season of the year, making the data suitable for this DTCR study. Over the selected time period, the average wind speed was $6.54 \text{ m}\cdot\text{s}^{-1}$.

In comparison, the typical average wind speed in the Czech Republic at 50 m above ground is $4.05\text{--}5.40 \text{ m}\cdot\text{s}^{-1}$ [98]. The availability of data was about 87.6%, with a total of 135,112 1-minute records. To illustrate the variability



Figure 30: A view of the meteorological mast at Dlouha Louka.

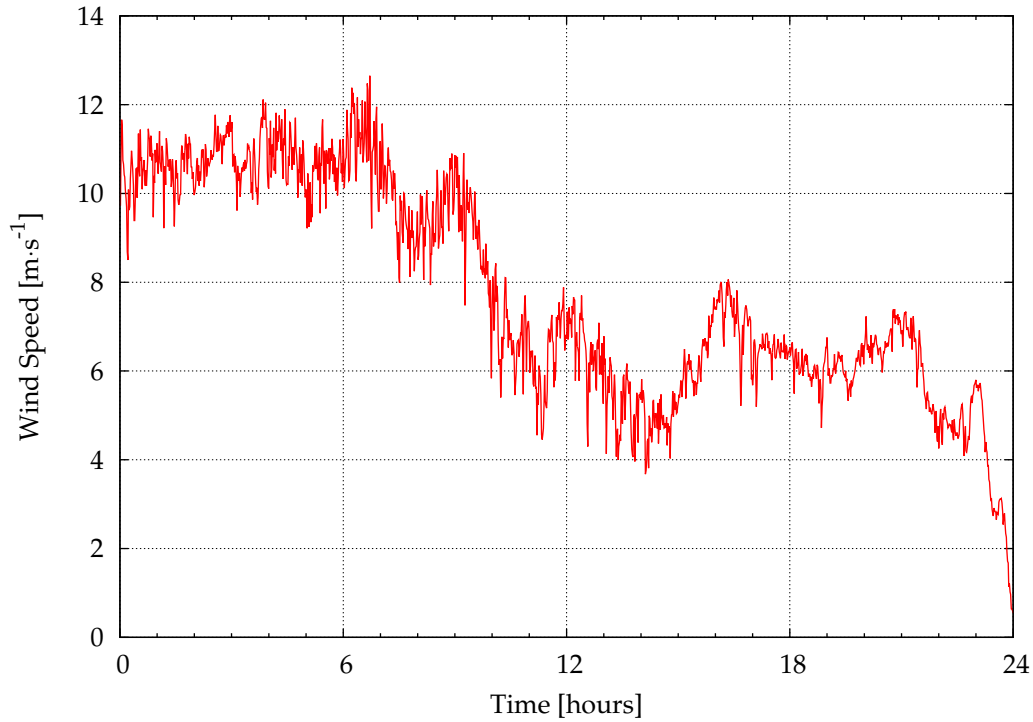


Figure 31: Sample of the 1 min averaged wind time series used in this study (June 19, 1999).

of the data on different timescales, a 24 h sample of the time series, with measurements averaged over 1 min intervals, is shown in Figure 31.

Although the mean wind speed is higher than average, the quality of the distribution fit is more important than its parameters. As our purpose is to assess the update time interval, turbulent properties of wind speed are all important. The shape of the turbulence spectra (i.e. the variability of wind speed) depends mainly on surrounding terrain roughness and stability of the atmosphere, whereas the absolute wind speed is only a scaling parameter [99]. By the same token, inter-annual changes typically affect only the mean wind speed, not the variability of the wind at the studied timescales.

4.2.2 DTCR Simulation

For the purposes of this study, the DTCR model was executed using time series of meteorological variables sampled and averaged over various time intervals. The average values were obtained by taking the mean of all regularly sampled observations within a given time interval. The shortest time interval used was 1 minute. A shorter interval would require modelling of the heat transfer inside the conductor, not considered in [37]. In addition to the base 1 min intervals, the calculations were also carried out using instantaneous and averaged data at intervals of 10, 30 and 60 min. The conductor temperature and ampacity calculations were performed for two common steel-reinforced aluminium conductors: Aluminium Conductor Steel-Reinforced (ACSR) Finch and Linnet. The Finch conductor is larger, with an outside diameter of 33 mm and a nominal ampacity of 1110 A. The smaller conductor, Linnet, has an outside diameter of 18 mm and a nominal ampacity of 530 A. These static ampacity ratings are specified for 75 °C conductor temperature, 25 °C ambient air temperature and 0.61 m·s⁻¹ wind speed [100]. Detailed conductor specifications can be found in Table 34 of Appendix B.

The wind speed measurements were taken at 20 Hz and saved to a data logger. The effect of using instantaneous against averaged values for conductor temperature calculations is examined in this section. The instantaneous values were sampled from the original raw 20 Hz data at specified time intervals (1, 10, 30 and 60 min). Averages of the 20 Hz data were also determined over the same time intervals and recorded as occurring at the end of the interval. The thermal model was then run for each of the two data sets – instantaneous and averaged – and the transient conductor temperature was

computed. These computations were performed only for the Finch conductor. This conductor is assumed to carry its nominal current of 1110 A.

An example of the results of using the instantaneous and averaged data sets is shown in Figure 32. It is apparent that the use of instantaneous values of the meteorological inputs causes significantly higher variability of the computed conductor temperature, compared to the use of averaged values. In addition, the use of instantaneous input variables induces significant changes in amplitude and occasional phase shifts of the conductor temperature signal. The results obtained using the 1 min resolutions are quite similar in both cases.

Using the averaged meteorological inputs, the transient temperature of the Finch conductor carrying its nominal current, was calculated. As before, the 1 min calculations were considered to represent the truth. There are similarities to the instantaneous results, inasmuch as longer averaging of the inputs results in a change of variability and phase shifts. However, the effects on the amplitude are different; the averaged inputs produce reasonable values of the simulated conductor temperature, but with substantial smoothing. This smoothing is significant, especially for the longest averaging interval (60 min), for which occasional errors of more than 10 °C occurred. The 10 min averaging interval, on the other hand, produces errors of less than a few degrees Celsius. The overall statistics of the transient calculations, driven by the averaged inputs, can be found in the second part of Table 18.

Table 18: Statistics of conductor temperatures calculated using averaged and instantaneous values, compared to 1 min series sampled using the same approach for the Finch conductor.

Sampling Approach	Statistic of Tc [°C]	Sampling Rate [min]			
		1	10	30	60
instantaneous	MAE	0.00	1.41	2.26	2.87
	99 th %-ile	61.64	62.95	63.61	64.31
averaged	MAE	0.00	0.40	0.88	1.30
	99 th %-ile	62.61	63.22	62.75	60.82

4.2.3 Analysis

A qualitative comparison of the results obtained using instantaneous and averaged inputs confirms that the averaged values provide a higher accuracy of ampacity calculations. In order to quantify this improvement, we used standard statistical techniques. The two sampling approaches have been compared to the base case of 1-min intervals (for the purpose of this study taken to be the truth), in terms of the MAE and the 99th percentile of the sample of calculated conductor temperatures. These statistics are summarized in Table 18. They were determined for the entire data set, not simply for the example period shown in Figure 32. For the averaged inputs, the values of the 99th percentiles naturally decrease with averaging interval because of smoothing effects. For instantaneous values, the 99th percentile increases, because the random extremes used as the thermal model input are maintained for an entire update interval. This can cause higher calculated conductor temperatures, especially for long sampling periods. In addition, the MAE with respect to the most detailed simulation is significantly higher in the instantaneous cases.

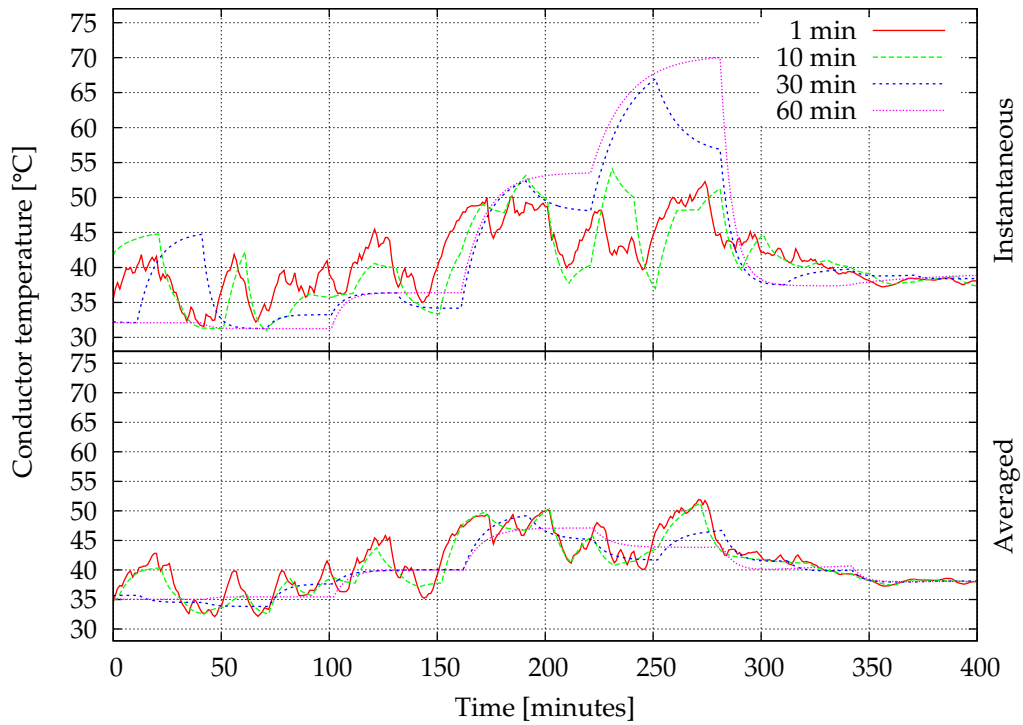


Figure 32: Example of transient conductor temperatures, computed by the thermal model for the Finch conductor, and driven by instantaneous (top) and averaged (bottom) inputs updated over the indicated periods.

4.2.4 Time Resolution Effects on Transient Conductor Temperature

Owing to its thermal capacity, a conductor filters out very short-term variability of wind speed. Hence, the cooling effect of gusts is effectively filtered out, and the conductor temperature responds primarily to wind and temperature timescales beyond several minutes. In order to demonstrate this effect, the spectral density of the de-trended time series of wind speed and conductor temperature was calculated using Welch's averaged modified periodogram method [101]. In this process, the time series was divided into eight sections and windowed using Hanning's method. This method is often applied for wind time series analysis [102]. The resulting spectra, normalised with frequency, are shown in Figure 33, for timescales of minutes to hours. For conductor temperature, the amplitudes are significantly reduced for frequencies higher than approximately 2×10^{-3} Hz, which corresponds to about 8.3 min. This result is consistent with the relatively small apparent differences between the time series of conductor temperature calculated with 1 and 10 min averages, as shown in the bottom part of Figure 32.

4.2.5 Time Resolution Effects on Ampacity

Ampacity series were obtained for both conductors, using steady-state calculations with the thermal model, and using the averaged values (there is no need for a transient approach when the temperature is fixed).

The results for the Finch conductor show that, during the studied period, the line could transmit, on average, about 2070 A with a standard deviation

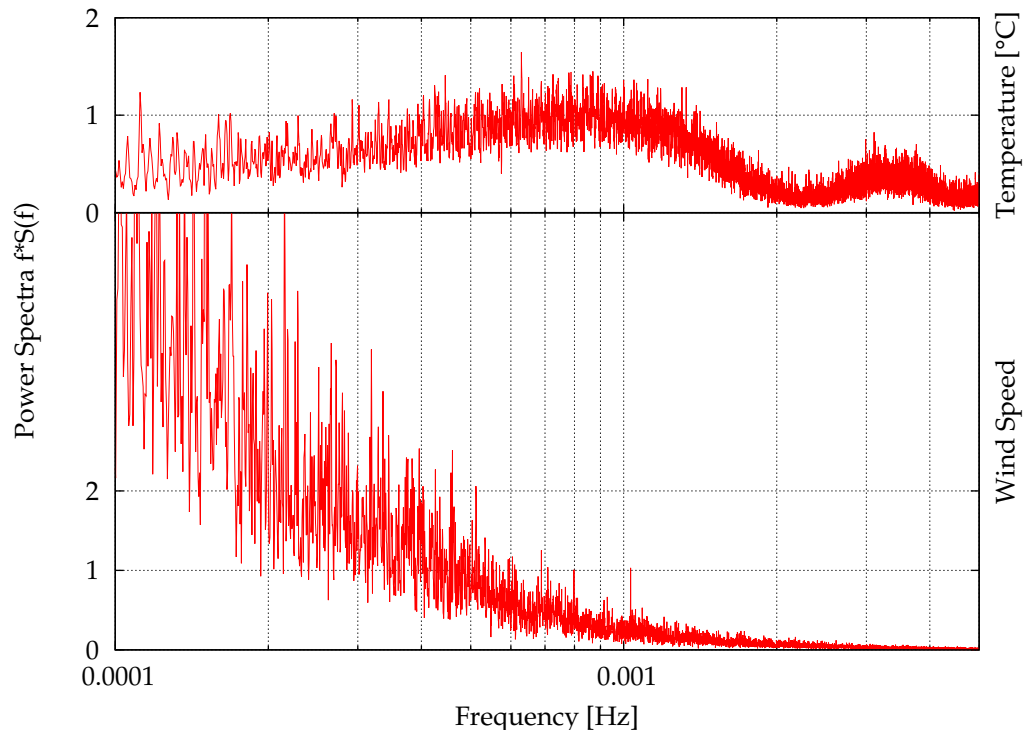


Figure 33: Spectral density, normalized with frequency, of time series of conductor temperature (top) and wind speed (bottom) for frequencies between 1×10^{-4} Hz and 5×10^{-3} Hz (logarithmic scale).

of 424 A, that is, 86% more than the static rating. More than 99% of the time, the computed ampacity exceeded the static rating threshold. This does not imply that 2070 A could be transmitted over the line continuously. At the same time, it should be noted that the rating temperature used to obtain this figure is 75 °C. In other words, it is 20 °C lower than the temperature at which ACSR conductors begin to undergo permanent damage. This provides a substantial safety margin to ensure that the risk of conductor thermal overload is minimized. Similar values were obtained for the smaller conductor, Linnet, for which the average ampacity gain was 82%, and the higher-than-static ampacity rate of occurrence was also around 99%. The very high probability that dynamic ampacity exceeds the static rating is likely caused by the windiness of the site. Our experiments in a real-world transmission line setting indicate about 56% average ampacity gain, and a higher-than-static ampacity rate of occurrence around 97% [103]. The statistics of the ampacity calculations for all averaging intervals are summarised in Table 19. As expected, the Mean Absolute Percentage Error (MAPE) increases with the length of the averaging interval. This increase is independent of conductor size. For both considered conductors, the value of MAPE is more than 60% higher for hourly averages compared to 10 min averages.

The errors in thermal calculations using time-averaged inputs cause the computed ampacity to be lower than the actual value more often with increasing averaging interval. Using the statistical distribution of the errors, the computed ampacity can be shifted down in such a way that the risk of the computed value being smaller than the actual ampacity (here assumed to be the 1 min values) is minimized. If the 99th percentile of the corresponding differences were subtracted from the computed ampacity, this risk would be

Table 19: Mean Absolute Percentage Error (MAPE) of calculated ampacities compared to 1 min averaged series, and the 95th and 99th percentiles of the corresponding differences.

Conductor	Statistics of Ampacity [A]	Sampling Rate [min]		
		10	30	60
Finch	MAPE	3.01	4.04	4.85
	diff 95 th %-ile	139.18	184.83	220.37
	diff 99 th %-ile	255.20	334.35	398.00
Linnet	MAPE	3.04	4.08	4.90
	diff 95 th %-ile	65.08	86.42	102.96
	diff 99 th %-ile	119.29	156.36	186.59

of the order of 1%. Hence, if hourly averages are used for the Finch conductor, about 40% of the potential ampacity gain is not realized. With the 10 min averages, the use of this safety margin would cause a 26% loss of the potential gain. A detailed view of the distribution of ampacity errors caused by various averaging times of the meteorological inputs is provided in Figure 34 for the Finch conductor.

The errors in ampacity were calculated with respect to values based on 1 min averaging (considered to represent the true values). This is a reasonable assumption since one minute is likely smaller than the conductors' thermal time constants. In order to demonstrate this, the thermal time constants for both conductors were calculated using Equation 5. The initial current was set to the nominal ampacities of the conductors: 1100 A for Finch and 530 A for Linnet. The final current was set to the nominal ampacities increased by the mean absolute error of the shortest (10 min) interval. For the Finch conductor, the corresponding initial and final currents and temperatures produced a thermal constant of 13.7 min, whereas for the Linnet conductor, the constant was 18.6 min.

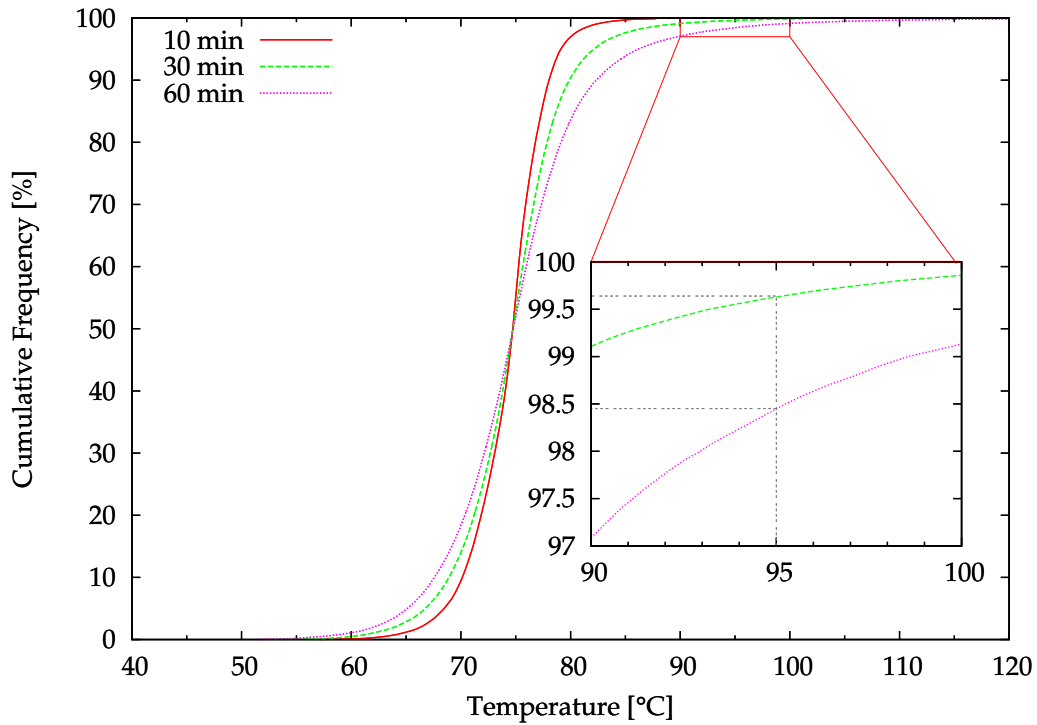


Figure 34: Cumulative frequency distribution of the conductor temperature, calculated with various average and update periods for the Finch conductor (insert shows an enlarged portion of the full graph).

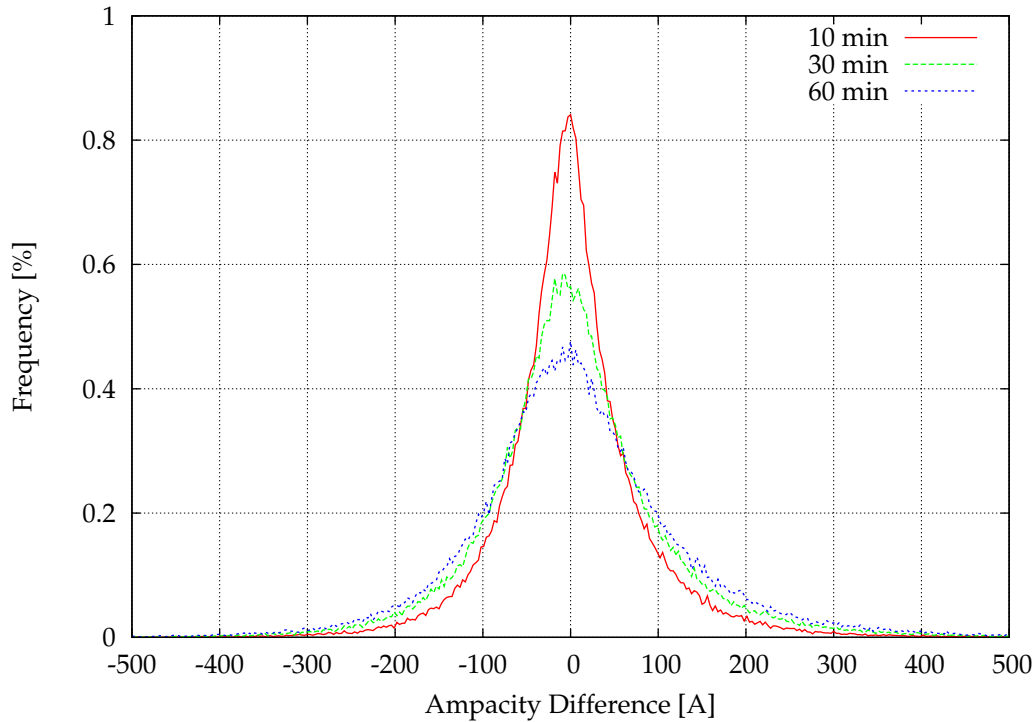


Figure 35: Distribution of differences in ampacity between 1 min updated-and-averaged time series and those with longer update periods for the Finch conductor.

It is clear that the thermal capacity of a conductor significantly affects how the calculated error in ampacity translates into the error of the calculated temperature. In order to examine this effect, the simulated line was loaded with a current based on the computed ampacities for 10, 30 and 60 min averaging intervals. The transient temperature was calculated for the Finch conductor, using the 1 min series of wind and temperature measurements. Subsequently, the difference between the computed conductor temperature and the threshold of 75°C was calculated, in order to gauge the error induced by the reduced time resolution of the ampacity input. The cumulative frequency distribution of the calculated conductor temperatures is shown in Figure 35. As expected, the largest differences appear when using ampacities calculated based on 60 min intervals.

Further analysis of these results provides an insight as to how much residual risk of conductor thermal overload there is, when ampacity is determined for the 75 °C maximum allowable temperature. The thermal overload threshold temperature, at which aluminium strands start to become brittle and lose their tensile strength, is usually considered to be 95 °C [104]. Using the temperature series calculated for the 75 °C threshold, the probability of exceeding the 95 °C temperature can be determined. This probability expresses how much the ampacity calculation errors affect conductor aging [36]. Using 60 min ampacity averages, line temperatures above 95 °C occur with a frequency of almost 1.6%. Using 10 min ampacity averages, this probability drops to only 0.01%, providing a large margin for safe operation of the conductor.

4.3 ACCURACY OF DTCR FORECASTS

This section provides an assessment of the accuracy and risk of using NWP models to estimate a transmission line's ampacity. NWP models provide meteorological variables on a spatial grid. This allows for the estimation of the ampacity corresponding to the thermal bottleneck of an entire transmission line. Furthermore, these models can also forecast the values of meteorological variables with a forecast horizon of up to 84 hours. Short-term (several hours) prediction of ampacity can be used in real-time operations and contingencies, while the medium-term (several days) prognostications are important for planning outages, maintenance, and market operations. Moreover, hav-

ing the capability to forecast line ampacity ratings in the future can open new opportunities for utility companies to make strategic market decisions. Using NWP models to estimate line ampacity has the potential to significantly reduce the cost of deploying DTCR systems for power transmission utility companies. It eliminates costs related to sensor procurement and installation, communication networks and maintenance.

The following study evaluates the accuracy of NWP-based DTCR ratings. An extensive set of simulated forecasts were performed and used to estimate the ampacity of a transmission line. The results were compared against those obtained from an on-site meteorological station. Additionally, a risk assessment study was performed to gauge the potential for conductor degradation from excessive operating temperatures.

4.3.1 Forecast Simulation Setup

To evaluate the accuracy of using high resolution NWP forecasts to calculate ampacity, a series of simulated forecasts were carried out. The Indian Arm crossing location was again selected for this study, as it has a high accuracy meteorological station installed on one of the transmission pylons found at this site. For a detailed description of this location, see Section 4.1.2.

WRF model v3.3 was used to generate the required forecasts for this study. A telescoping grid configuration was used, and centered over the location of the Indian Arm crossing FTS station. As sensor observations were only available for the year 2010, the same time period was chosen to generate forecasts for. The model configuration parameters for the forecasts can be found in Ta-

ble 32 of Appendix A. No grid nudging was performed during any forecast simulation. This was done to simulate an operational forecast, where future reanalysis data would not be available ahead of time. 84-hour simulated forecasts were performed using NAM data to initialize the domain and update the boundary conditions. Ideally, four forecast runs would have been performed for every day in the period under study. Unfortunately, this would require significant computational resources, both to perform the forecast runs and to subsequently process and analyze the resulting data. Therefore, only a subset of the 84-hour cycle runs was considered. Care was taken to ensure that the entire time span in the study was completely covered by the same number of forecasts, and that these were initiated at different times.

Using the generated forecast data, ampacity time-series were calculated using the thermal model, presented in Section 4.1.1. For each data sample obtained from the forecast, an ampacity value was calculated for the BC Hydro transmission line situated at the Indian Arm crossing location. The calculations were based on the same AACSR conductor used in the precipitation cooling model verification study, with the characteristics described in Table 14.

To evaluate the accuracy of the NWP-based DTCR forecasts, a series of statistical analyses were performed. First, error measures were calculated between ampacity calculations obtained from the on-site FTS meteorological station, described in Section 4.1.2.2, and the computed NWP ampacity forecasts.

Second, an analysis was performed to estimate the risk associated with using the NWP-based DTCR values. This risk assessment was based on estimating the operating line temperature using the forecast line ampacity as the operating line current, and modelling the conductor temperature using the

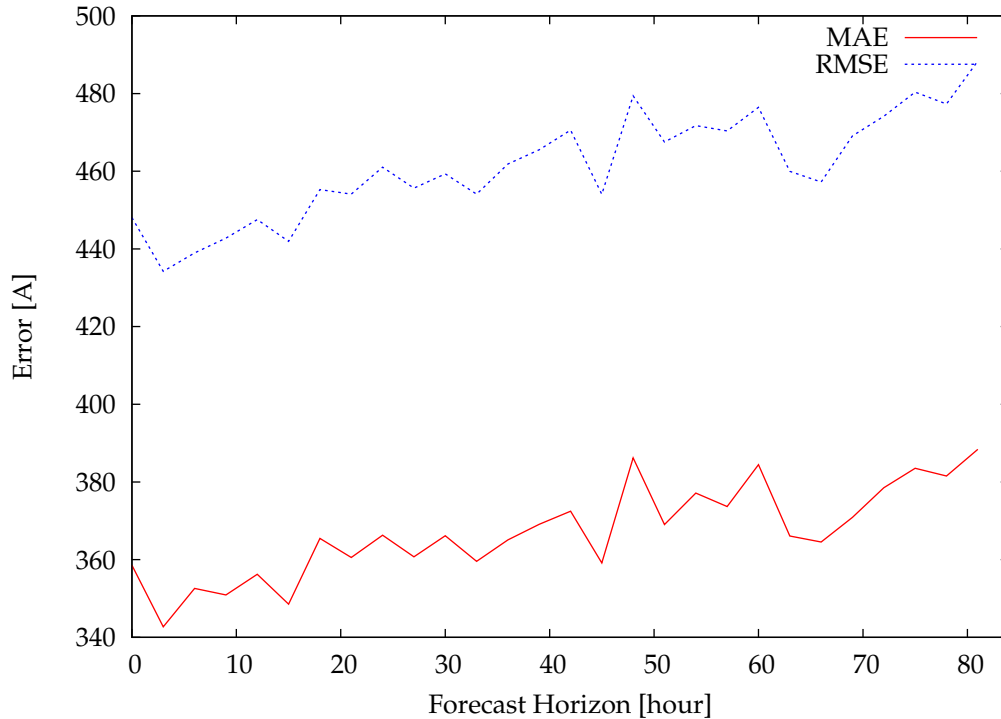


Figure 36: NWP DTCR ampacity error statistics (MAE & RMSE) with respect to the forecast horizon.

weather observations made by the FTS instruments. Steps taken to quality control the FTS data are described in Section 4.1.2.3.

4.3.2 Evaluation

The error statistics, calculated at regular forecast horizon intervals, are presented in Figure 36. While it is evident from the ampacity time series, shown in Figure 37, that the NWP-based DTCR can in fact forecast ampacities, they come with potentially significant errors. Because of this, the overall line temperature, shown in Figure 38, is above the desired 75°C mark, averaging between 80 and 85°C .

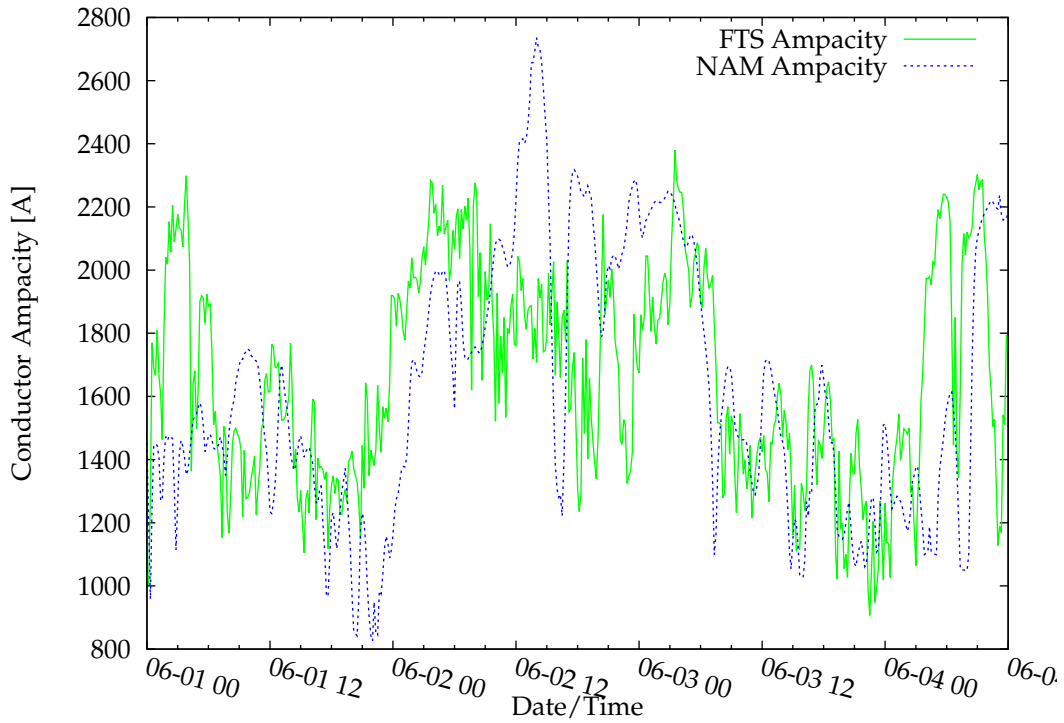


Figure 37: A sample NWP-based DTCR ampacity time series output for the BC Indian Arm crossing transmission line.

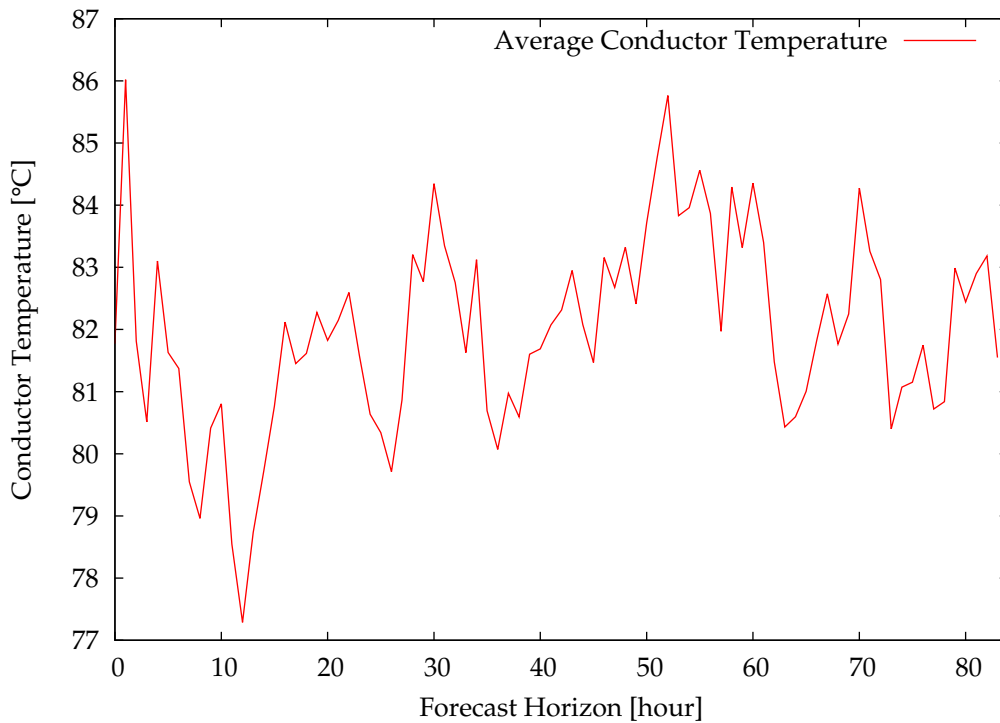


Figure 38: Average conductor temperature for all forecast ampacities with respect to the forecast horizon.

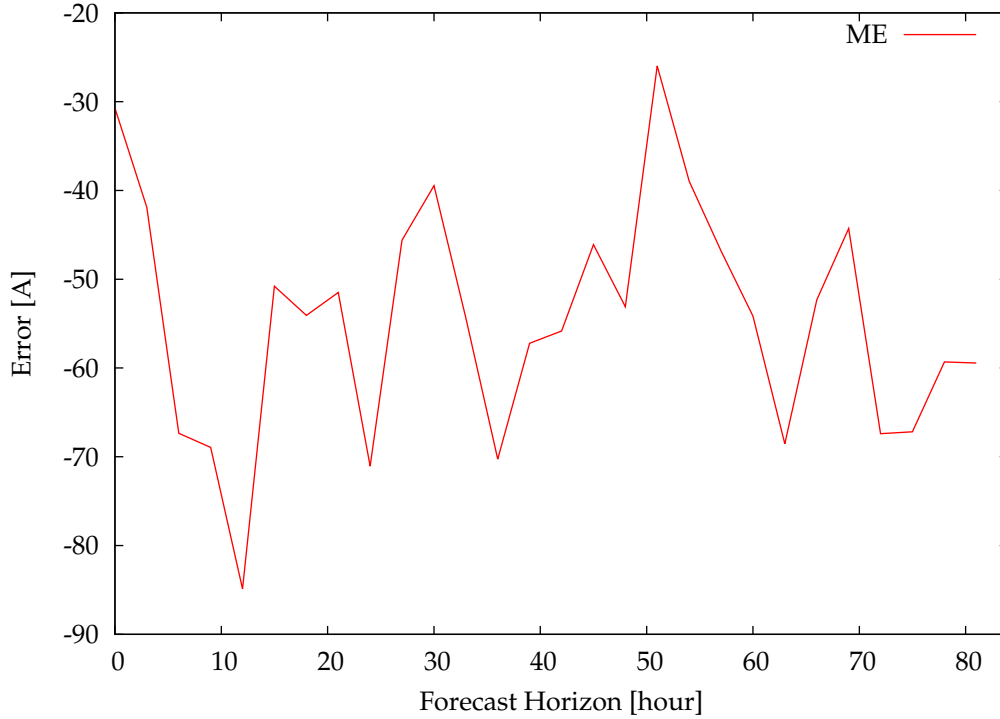


Figure 39: Mean Error (ME) of for the NWP-based ampacity forecast with respect to the forecast horizon. This figure shows the negative bias of the NWP forecast ampacity values.

Nevertheless, Figure 39 illustrates that the model is slightly biased to underpredict ampacity by approximately 50 A. For the purpose of ampacity forecasts, this is advantageous, in order to reduce the risk of overheating the conductor. However, additional steps are required to identify the cases where excessive ampacities are forecast. Otherwise, the slightly underpredicting bias does not provide any operating advantage.

From Figure 36, we can also see the increase in error as the forecast time horizon progresses forward. This is to be expected, given the fact that NWP accuracy diminishes with increasing forecast horizon [105]. This contributes to an additional MAE error of up to 66 A. The increase in error with respect to forecast horizon can also be seen in the trend of the `pred(25)` indicator with respect to the forecast horizon, shown in Figure 40.

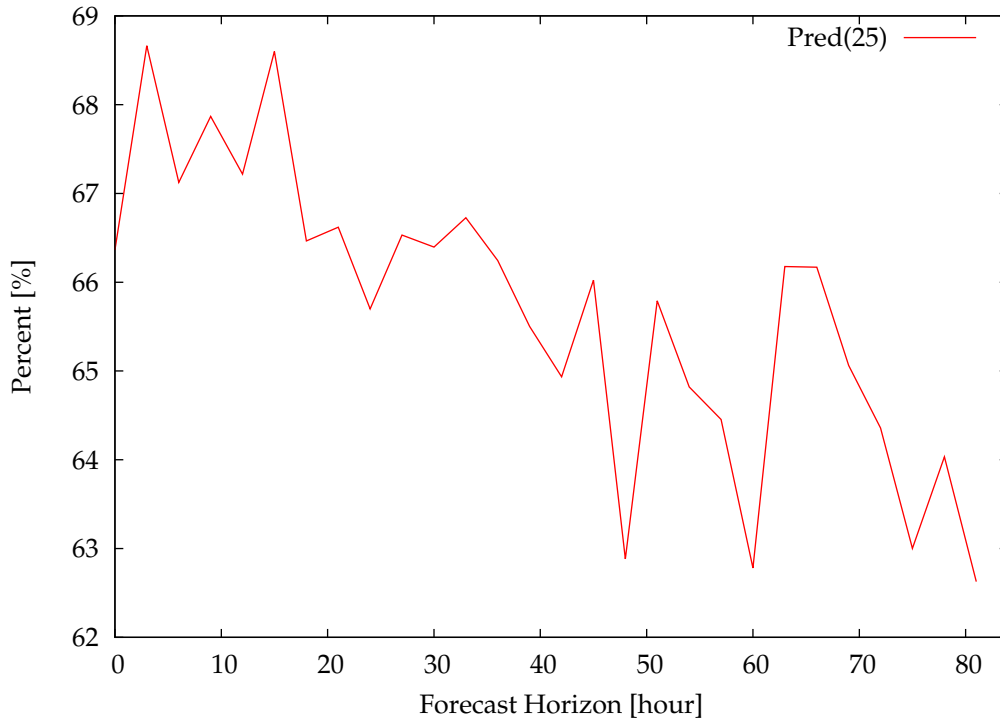


Figure 40: Pred(25) indicator of NWP forecast ampacity accuracy with respect to the forecast horizon.

To assess the risk associated with the ampacity errors, histograms of the conductor temperature were created. These are shown in Figures 41 to 45. The figures show the frequency of instances where the estimated conductor temperature, operating at the forecast ampacity value, exceeded the desired operating temperature of 75°C , and exceeded the maximal allowable operating temperature of 95°C , at which ACSR conductors begin to become irreversibly damaged. The histograms confirm that the majority of forecast ampacities slightly underutilize the capacity of the transmission line. They also show the fat tail of the distribution of cases exceeding the acceptable operating temperature limit.

The risk assessment data can be visualized in a Cumulative Distribution Function (CDF) plot, as shown in Figure 46. This figure can be used to assess

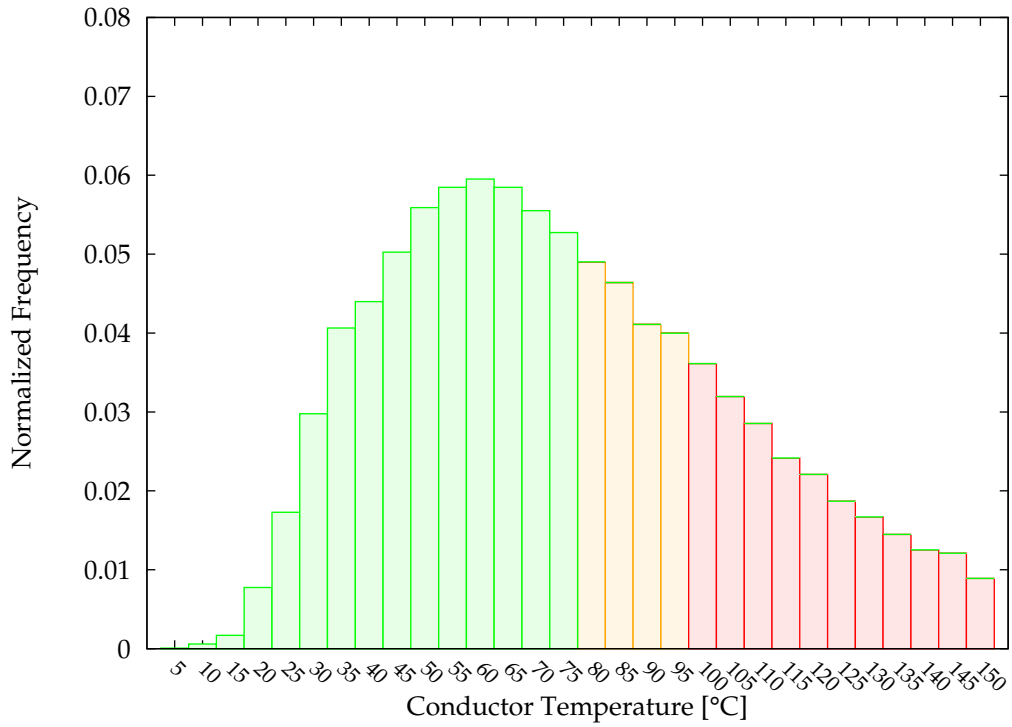


Figure 41: A temperature histogram for the BC Hydro Indian Arm Crossing transmission line for a 0-6 hr forecast horizon.

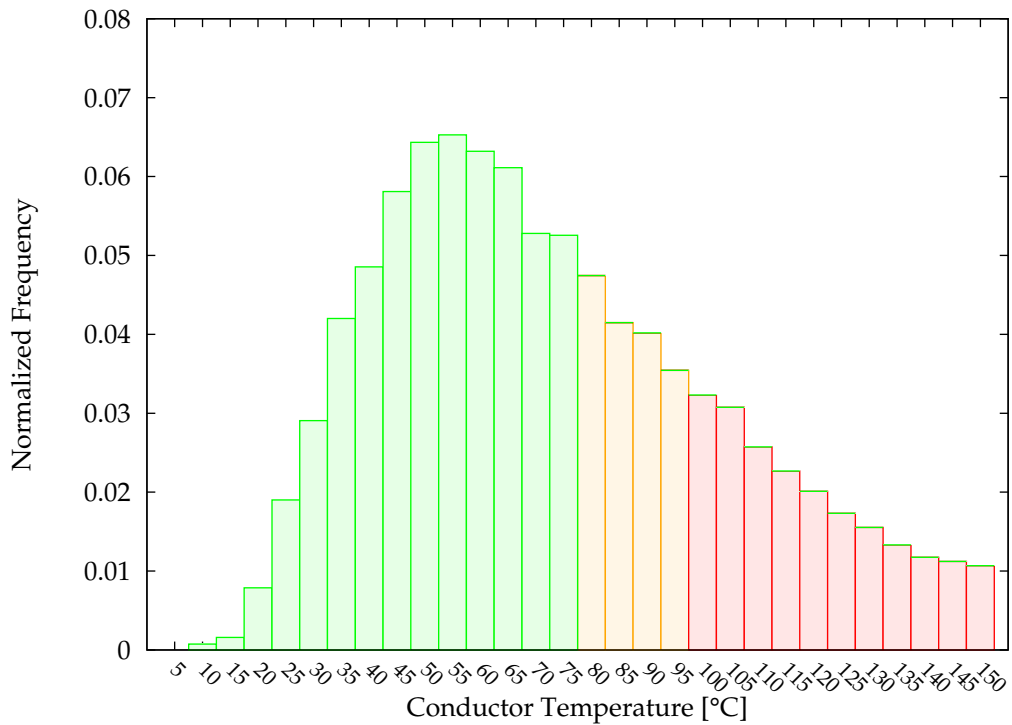


Figure 42: A temperature histogram for the BC Hydro Indian Arm Crossing transmission line for a 6-12 hr forecast horizon.

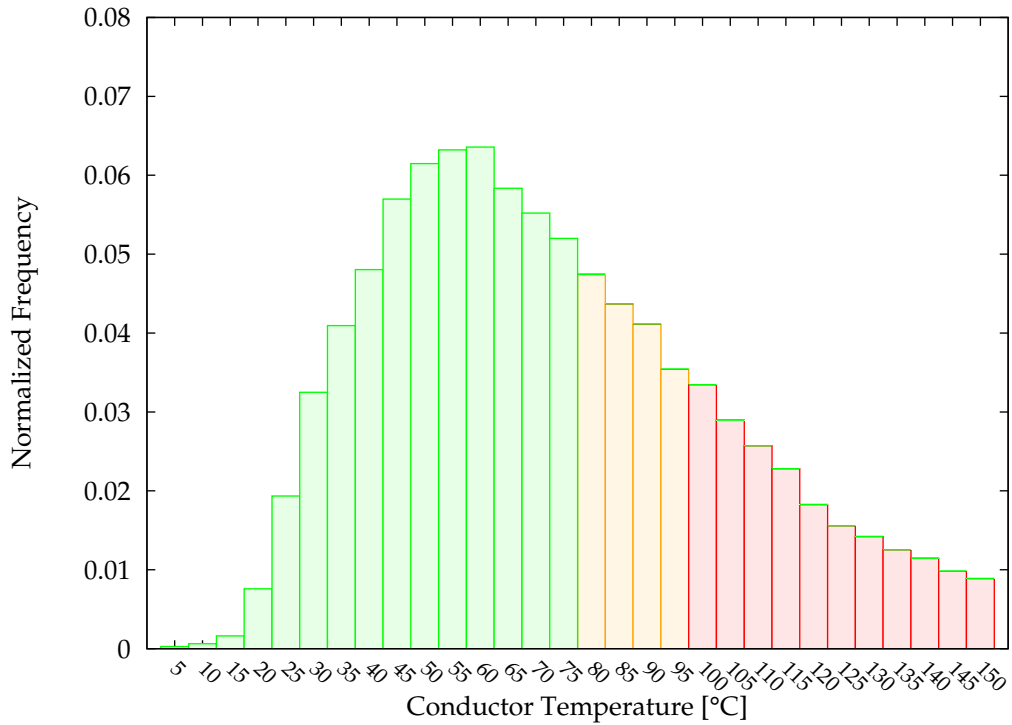


Figure 43: A temperature histogram for the BC Hydro Indian Arm Crossing transmission line for a 12-24 hr forecast horizon.

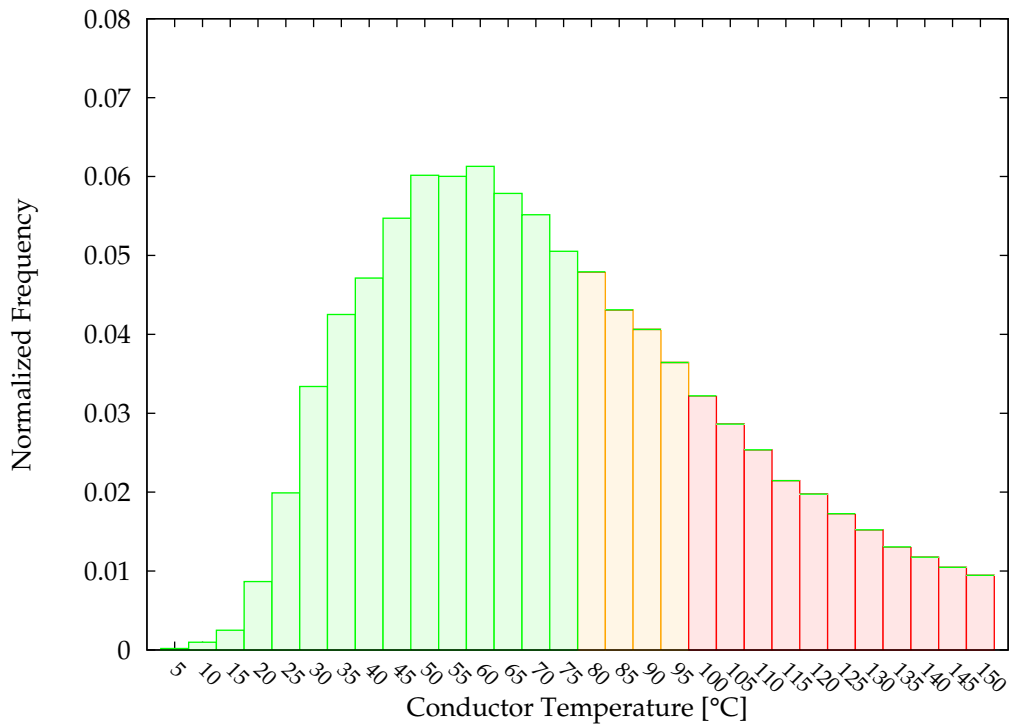


Figure 44: A temperature histogram for the BC Hydro Indian Arm Crossing transmission line for a 24-48 hr forecast horizon.

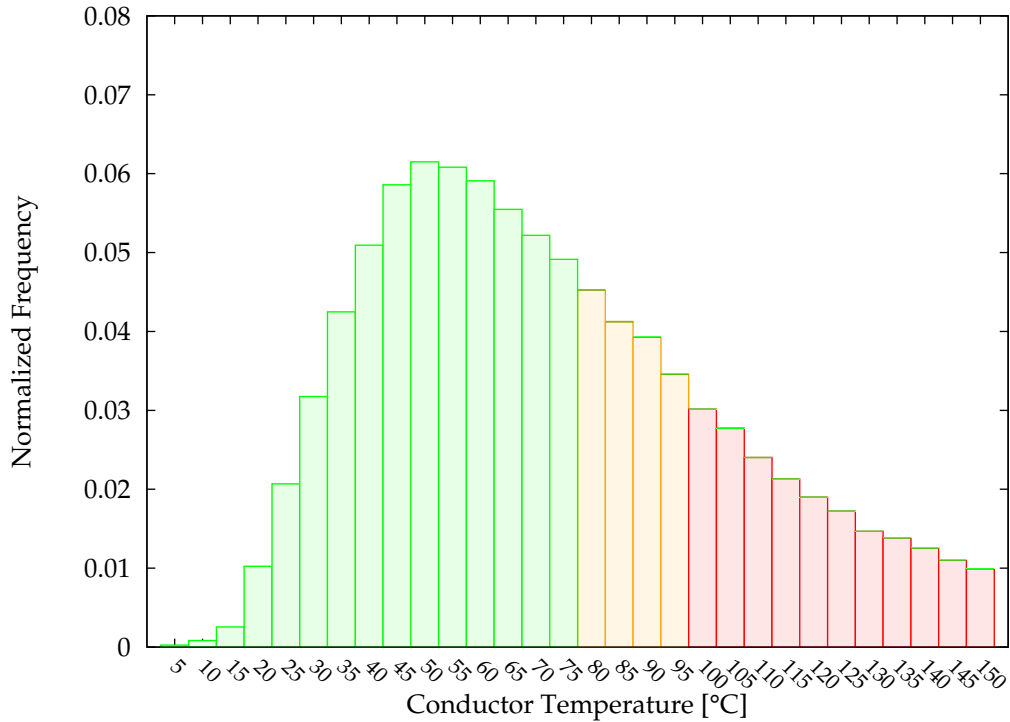


Figure 45: A temperature histogram for the BC Hydro Indian Arm Crossing transmission line for a 48–84 hr forecast horizon.

the risk of overheating the transmission line, if it was energized to the full forecast ampacity value.

For a significant majority of forecast ampacity values (75%), the line temperature does not exceed 95 °C. This suggests that it should be possible to use a fraction of the forecast ampacity to achieve gains in line capacity while mitigating excessive conductor temperatures.

By only partially utilizing the forecast ampacity values, gains in line capacity can also be achieved at a reduced risk of overheating the conductor. As shown in Figure 47, conductor overheating risk is substantially reduced when the line is only energized to 75% of the forecast rating.

In this configuration, the first two days of forecast ampacity introduce a risk of overheating the conductor to temperatures exceeding 95 °C of only

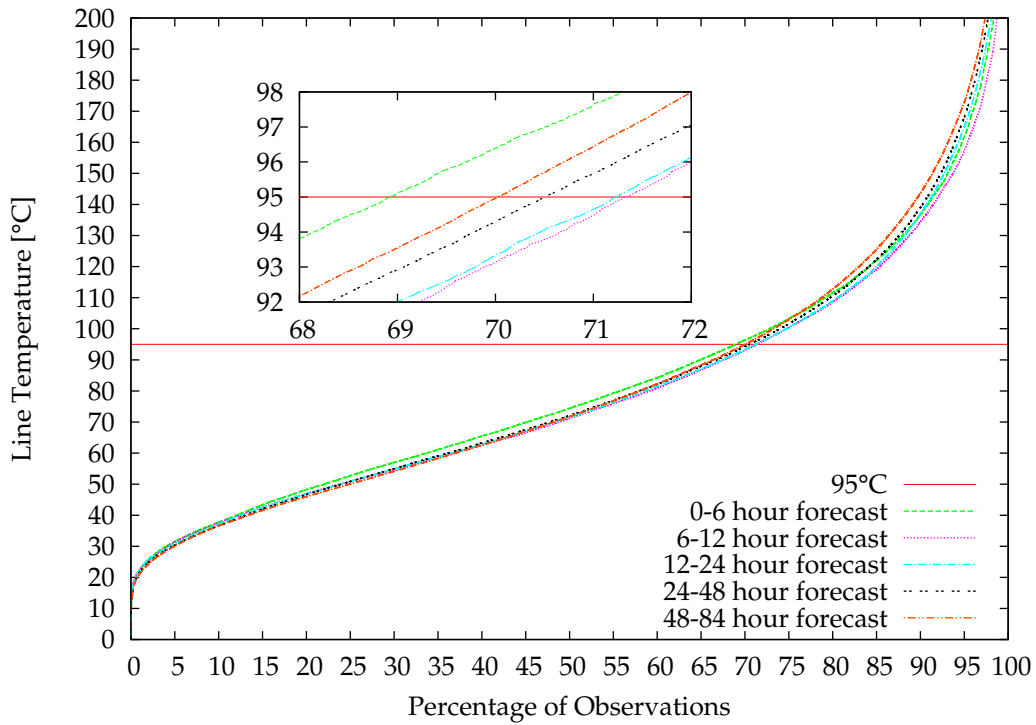


Figure 46: A CDF of conductor temperature calculated using the FTS weather observations and line current based on the forecast line ampacity (insert shows an enlarged portion of the full graph).

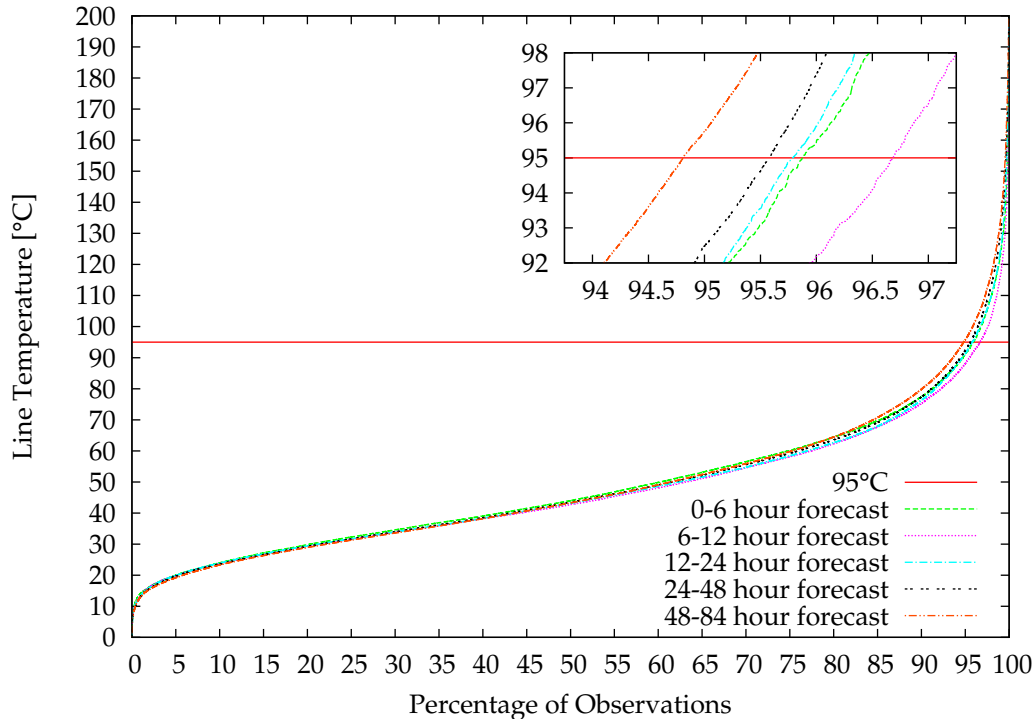


Figure 47: A CDF of conductor temperature using only 75% of forecast line ampacity (insert shows an enlarged portion of the full graph).

5%. This is substantially lower, compared to the 25% risk of causing permanent damage if the full forecast ampacity were used. This way, the risk of overheating the transmission line is reduced, while additional capacity is still capitalized upon. Despite a reduction in line capacity, the line ampacity is still substantially greater than the nominal static rating. On average, an additional 296.65 A can be carried by the transmission line when using 75% of the NWP forecast ampacity rating.

It is evident from the results obtained, that ampacity can be forecast using NWP systems; however, additional corrections to the modelled data are required before they can be safely and effectively used in the operation of power transmission systems.

The major shortcoming of the NWP-based line ampacity forecast is a result of WRF's prediction inaccuracy of wind velocity at the Earth's surface. While for many applications using NWP models, accurate speed and direction forecasts are not critical, it is absolutely essential for real-time thermal rating of power lines. The reason for this is the fact that a 90° shift in wind direction can result in the difference between maximum forced convective cooling and minimum convective cooling. In most operating cases, convective cooling is the single most important factor determining line ampacity, and hence, operating temperature.

Another limitation of using NWP for DTCR prediction lies in the inability of NWP models to correctly localize weather systems. The effect of errors in temporal localization can be observed in the ampacity time series sample, show in Figure 37. While a human observer can clearly see a strong correlation between the ampacity trend produced by the on-site FTS station and the NAM-based weather forecast trend, the instantaneous ampacity carries a significant error of a few hundred amperes.

For typical weather forecasting purposes, predicting meteorological events that happen an hour ahead or behind does not carry severe consequences or penalties. The exception to this is the use of NWP for specialized fields, such as air traffic and military planning. However, for DTCR purposes, the forecast must be localized correctly, both spatially and temporally, to take advantage of the full available capacity and to avoid the risk of conductor damage.

Furthermore, the location of the transmission line under study poses additional challenges. The Indian Arm Crossing is sandwiched between the Pacific Ocean and the Coast Mountains. This location has a two-fold detriment to the NWP accuracy. First, limited observations are available for areas

covered with bodies of water. This results in less accurate initialization and boundary conditions. Second, the complex terrain due to the mountainous region introduces sharp gradients into the NWP fields, and this results in numerical stability challenges. However, transmission lines situated in inland areas will not be subject to these limitations. Hence, it can be reasonably assumed that the DTCR accuracy of these regions may be significantly higher compared to coastal regions.

Finally, before an NWP model can begin to output usable forecast data, it must be “spun up”. This is to allow for an equilibrium to be established between the hydrometeors and the temperature, wind, and moisture fields. Should the NWP model be cold-started for a given forecast, depending on the application, the first day of the forecast output may be of undesirably low quality. This time period would be, of course, the most critical time for an NWP-based DTCR system. To mitigate the problems associated with model spin-up, operational forecasting is typically carried out by “restarting” the model from a saved state snapshot. This snapshot is saved from a previous run, and then merged with up-to-date observations, through a process known as data assimilation.

4.4 APPLICATIONS OF DTCR TECHNOLOGY

Aside from using DTCR calculations to calculate the current capacity of transmission lines or estimating the conductor temperature, they can also be used in decision support systems to assist utility operators in making important

decisions regarding the infrastructure. DTCR methods can be used to assist in planning and routing new transmission lines, as well as supporting upgrading and maintenance decisions. DTCR can also be used to construct larger plants near existing transmission lines, and incorporate green, low emission energy during periods that are favourable both for power generation and large transmission capacity.

4.4.1 Optimal Routing of Power Transmission Lines

Construction of new power transmission lines is a costly and time consuming endeavour. In order to maximize the return on investment in the construction of new power transmission lines, this process should be supported by information on the climatological conditions in the planned area, and their effect on the power line operating conditions and aging.

To address this deficiency, a novel approach is presented in this section that makes it possible to objectively incorporate the meteorological factors affecting power transmission lines into the construction planning process. The system analyzes the different ambient conditions that are present across spans of potential locations for a given transmission line and then computes an optimized route to meet the desired criteria, such as maximizing the transmission capacity. It selects way-point coordinates for the transmission line using an algorithm that attempts to minimize the line temperature by avoiding locations that are prone to cause temperature hot-spots. This, in turn, provides gains in additional transmission capacity when coupled with DTCR

A version of this subsection has been published in [106]. I made a substantial contribution to the content of this publication. I also wrote a major portion of the published manuscript.

technology, allowing utility companies to increase the return on investment even further.

4.4.1.1 *Approach*

The intelligent line routing system utilizes the heat balance equation described in Section 2.1.3.2, along with high-resolution meteorological data, to compute the line operating characteristics for all locations in the area of interest.

In heat balance Equation 1, the q_c , q_r , and to a certain extent q_s terms vary spatially because of meteorological conditions induced by terrain features. By solving the heat balance equation using the meteorological variables, the conductor's ampacity, operating temperature or resistance can be found for a set of candidate routes. Thus, the impact of the line placement can be estimated and subsequently used to select the best location for the line routing to satisfy the user-selected criteria. To attain maximal utility of the resulting optimal placement, the transmission line should employ a DTCR system.

The line placement algorithm finds an optimal line positioning based on a process involving four major steps.

1) *Preparation of weather data.* In order to compute the climatological impact of weather on power transmission lines, a high-resolution data set containing meteorological observations must be obtained. For the purpose of this study, the NARR historical dataset [83] was used. The historical weather data for an area covering the entire region of interest is extracted and then further interpolated to a higher grid resolution. The interpolation is done by utilizing the state-of-the-art WRF [82] mesoscale NWP model. WRF generates a high-resolution hindcast from the original initialization data. This is done to allow

for finer control of the line routing and, in particular, to ensure that significant small-scale meteorological features are considered in the routing process. Should the original NARR data set be used directly, the terrain impact on the local weather conditions at the power line locations would be neglected due to the coarsely spaced nature of the data set (32 km grid spacing).

2) *Simulation of operating conditions.* From the post-processed historical weather, the relevant meteorological variables required to solve the heat balance equation are extracted, and the necessary intermediate values are computed. The conductor ampacity rating, operating temperature and resistance are computed for each position in a grid spanning the region of interest, over the entire time period of the extracted meteorological data. To simplify the optimization process and to relax the computational requirements, the system was configured to allow for a maximum of eight possible directions that a segment of line can take to a neighbouring node, giving a total of four possible line segment orientations. This significantly reduces the computational challenges of finding paths with a large number of degrees of freedom in how the line can be positioned.

3) *Weight evaluation.* To assess which areas are best suited for the line construction, statistical measures of the ampacity, temperature, and resistance values are computed for each grid point in the region of interest. This provides the search algorithm with a measure to differentiate between alternative route selections, and to provide the user with an assessment of the quality of the discovered routing. These measures are incorporated into a graph structure, representing all the possible way-points that can be used to form a line route. The measure used for the presented line routing study estimates how much the ampacity of each potential line segment differs from the average of the

entire grid. The line routing system first computes how much each grid point ampacity deviates from the average ampacity at time t

$$D_i(t) = A_i(t) - \frac{1}{N} \sum_N A_n(t), \quad (52)$$

where D_i is the difference between the line point ampacity A_i and the mean transmission line ampacity, and N is the total number of line segments in the grid. From this, the overall cost function (weight), W_i , for a line segment i connecting two adjacent nodes is found

$$W_i = Dist(i) \times \left[\max_{N,T} \left(D_i(t) \right) - \frac{1}{T} \sum_t D_i(t) \right], \quad (53)$$

where $Dist(i)$ is the physical distance of the line segment connecting two points in the grid.

4) *Route finding.* Finally, a transmission line routing that maximizes the user's objective is found using a graph search procedure based on Dijkstra's algorithm [75], which searches for a minimal path in a weighted graph. For the purpose of the presented system, the procedure aims to find a set of edges in the graph which translates to a line routing with the maximum average transmission capacity possible.

4.4.1.2 Case Study

To assess the performance of the proposed line routing system, a region connecting two major urban centres in the province of Alberta, Canada was se-

lected. The hypothetical power line was configured to use an ACSR “Finch” conductor, having a nominal ampacity rating of 1093 A at a maximum operating temperature of 75 °C. The conductor’s physical parameters, used by the routing system, are listed in Table 34 of Appendix B. Meteorological data from the summer months of 2008 were used to generate the required input data set for the line positioning system. The meteorological variables were interpolated using WRF to a spatial resolution of 3.2 km. The line conductor operating state was computed for every four hour interval in the period spanning the extracted data. This sampling period was selected to reduce the storage costs associated with saving high resolution meteorological data for the entire region, and to reduce the subsequent computational costs of performing the routing optimization.

The overall cost function for each node in the considered region is presented in Figure 48. The figure depicts the average ampacity deviation for the four different conductor orientations from the overall average ampacity. This illustrates the ampacity variations that occur across the entire grid, pointing out how certain areas have a significantly lower potential ampacity rating over other regions, independent of the angle of the wind with respect to the conductor axis. Should the constructed line pass through one of these minima, its ampacity will be limited by this bottleneck.

The resulting operating statistics for the optimized power transmission line placement, compared with a routing found using a simple weighting function based solely on the distance between adjacent nodes, is presented in Table 20. The optimized routing allows, on average, 28.4 A more current to be transmitted with a 9 km longer transmission line. Based on transmission line construction costs described in Table 22 in the following section, the addi-

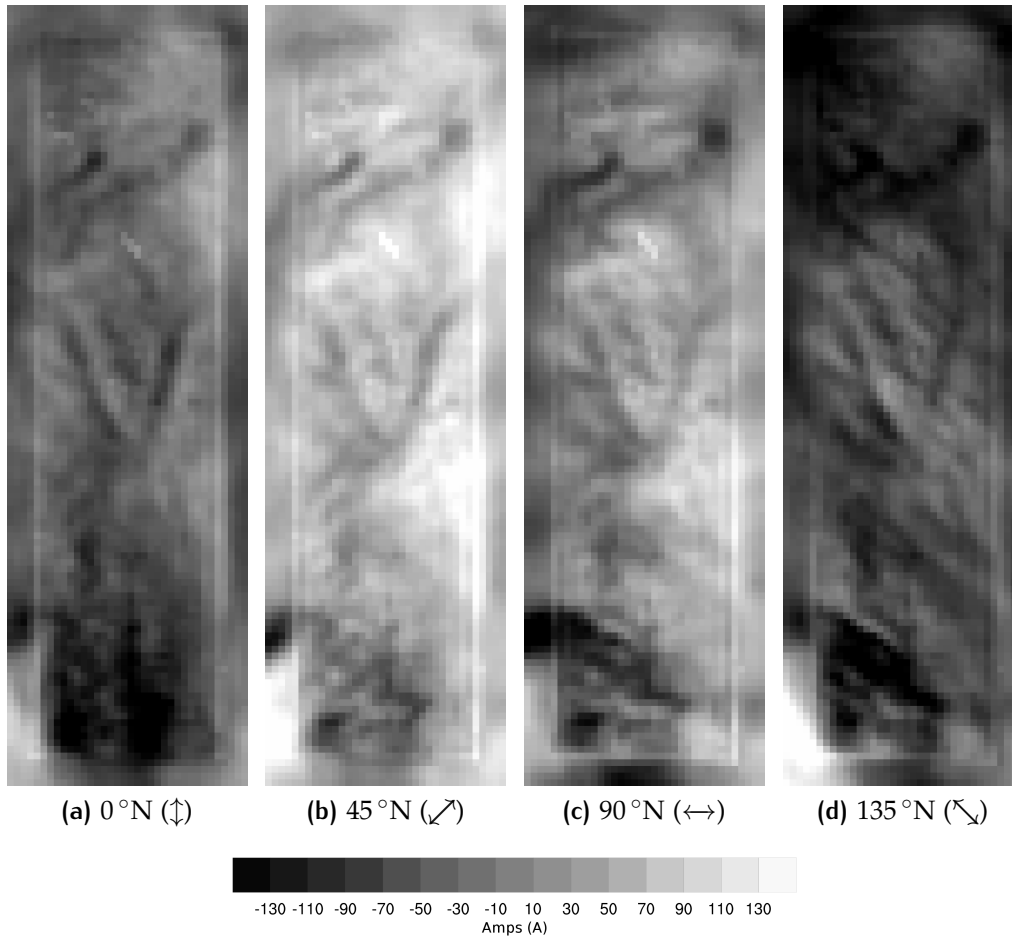


Figure 48: Average ampacity deviation for each of the four possible conductor orientations across the considered region.

tional length of transmission line incurs an approximate construction cost of \$263,815.00. This price assumes a uniform construction cost across the entire considered region.

4.4.1.3 Analysis

While the initial results of the line placement system provide an ampacity improvement only on the order of a few percent, it is important to keep in mind how much additional power this translates into. The increase of 28.4 A in the average ampacity for the “Finch” conductor used in the optimally placed line,

Table 20: Operating characteristics of the hypothetical transmission line placed using the line routing system. The presented values assume that the power line is operated at a temperature of 75 °C or that 1100 A is passed through the conductor.

Measure	Minimal Distance	Best Ampacity
Line Length [km]	297.3	306.3
Average Line Ampacity [A]	1162.5	1190.9
Average Node Ampacity [A]	1621.8	1677.9
Average Resistance [Ω]	21.0838	21.7683
Average Power Loss [MW]	25.51	26.34

translates to an additional transmission capacity of 14.2 MW of power for a 500 kV transmission line. This provides the opportunity to connect many renewable energy sources, whose generation capacity is often comparable or smaller to this gain. Furthermore, even if the power line is not operated at its maximum capacity, the optimized placement translates into lower operating temperatures, which, in turn, extends the lifespan of the conductor. This is due to the fact that the line must pass through regions that provide better cooling in order to raise the line ampacity.

Additionally, it is important to keep in mind that the system faces a challenging benchmark in the comparison; a real world line positioning would never follow a strict shortest path routing without regard to other, more dominant factors selected in the routing process. As such, a real-world line routing will not have the efficiencies associated with lowest ohmic resistance (due to the shortest conductor length possible) going in its favour. Consequently, this approach leads to better opportunities for the identification of more optimal placement of transmission lines, in comparison with those selected by traditional planning approaches.

Comparing the optimal line placement, shown in Figure 49, with the ampacity deviation plots, shown in Figure 48, illustrates how the line routing

system attempts to place and orient the transmission line to pass through regions which provide the best operating conditions. This transmission line routing minimizes sections with suboptimal placement and orientation in as much as possible, while at the same time keeps the line short. Furthermore, it is evident from the deviation plots that the greatest factor limiting the ampacity is the area surrounding the southern city (Calgary). While the upper two thirds of the grid provide opportunities to place the line in an optimal position, the area surrounding the southern destination poses a bottleneck. No matter which routing position is selected, the capacity will be limited by the final stretch. To overcome this bottleneck, an additional procedure needs to be performed that would provide an alternative conductor strategy, either using various conductor types or multiple circuits, to raise the line ampacity.

Finally, it is important to note that the topography between the two cities selected in this study is composed of predominantly flat plains and it does not vary significantly. Consequently, this example does not provide an opportunity to demonstrate the full potential that could be attained if a line passed through widely varying geographical regimes. Routing a line through regions that have rapidly changing features should result in an even greater benefit as a result of the optimal routing generated by the proposed system, compared with routing a line between two points on generally homogeneous topography. For example, avoiding all regions with predominantly still air, or a regions with wind typically parallel to a transmission line could, in the best case scenario, double the capacity of it. This factor is important to keep in mind when evaluating the system's performance, because many renewable energy sources are likely to be situated in remote locations whose geography and climatology will likely vary to a far greater degree than in this example.

4.4.2 Identifying Line Segments for Upgrading

As described in Section 2.1.5, to overcome line capacity problems, some utilities have began incorporating DTCR technologies into their existing transmission lines to harness underutilized line capacity. However, capacity gains that can be obtained from DTCR technologies may be hampered by certain segments of a given transmission line if they have an overall lower transmission capacity compared to the remaining parts of the line. If such bottlenecks exist, the overall ampacity rating of the entire line is decreased. Furthermore, if short sections of transmission line with a below average ampacity rating are undetected, they will undergo accelerated aging and irreversible degradation. This can eventually lead to premature failure of the conductor through loss of tensile strength; in the worst case scenario, it can become a major safety hazard.

The following section presents a novel system to allow the power transmission industry to analyze an existing power transmission line, based on meteorological factors affecting transmission lines, and then identify which segments pose the greatest bottleneck. Subsequently, these segments can be upgraded by reconductoring or increasing the number of conductors per bundle to increase the overall line capacity. This section also presents a study that evaluates an intelligent power line upgrading system's performance on three existing power transmission lines.

A version of this subsection has been accepted for publication in [107]. I made a substantial contribution to the content of this publication. I also wrote a major portion of the published manuscript.

4.4.2.1 Approach

To discover weak links in a transmission line, the intelligent line upgrading system obtains and analyzes ambient conditions that are present along the line, based on a high-resolution meteorological data set. It then computes the actual ampacity over a substantial period of time. The system then identifies, using a GA, which segments of the line hamper the capacity most frequently and would be most cost-effective to upgrade.

The same process can be used to select conductors for use in new transmission lines. The system can choose an optimal conductor strategy that best meets the needs of a transmission utility while minimizing cost and excess resources.

The intelligent line upgrade segment selection system utilizes the heat balance equation described in Section 2.1.3.2, along with high-resolution meteorological data, to compute the line operating characteristics for a series of points along the transmission line of interest. The system then proceeds to determine the sections of the line that are limiting the current for the entire line and it tallies the severity of the limitation. The algorithm optimally identifies the sections of line requiring upgrading to meet user specifications, based on a process involving four major steps.

1) *Preparation of weather data.* In order to compute the climatological impact of weather on power transmission lines, a high resolution data set containing meteorological observations must be obtained. The data may come from a regional reanalysis dataset and be subsequently interpolated to a finer resolution, in order to better coincide with the transmission line placement. Alternatively, a more accurate source of data may be obtained from hindcasts us-

ing high resolution NWP models. Data obtained from these models will more accurately reflect the real-world operating characteristics of the transmission line, by better capturing the impact of topography on local weather patterns near the transmission line. Unfortunately, this source of data requires considerably greater computational resources and time to generate datasets of the required duration and resolution. Hence, using the latter method will incur a larger cost and time penalty to perform a comprehensive upgrade analysis of an entire transmission line.

It is important to note that, in this type of application, NWP models must be operated with the intention of providing accurate numerical weather outputs, as opposed to simulating operational forecasts. With this in mind, several key configurations should be made to the selected NWP model and simulation setup. First, the initialization data should only consist of reanalysis data that contains assimilated observations, as opposed to uncorrected global NWP model forecast outputs. Secondly, slowly changing static fields must be updated throughout the simulation run. These includes variables such as water surface temperature and albedo. Finally, grid-scale nudging should be enabled to ensure that the simulated hindcast remains consistent with the coarser initialization data.

2) *Simulation of operating conditions.* From the post-processed historical weather data, the relevant meteorological variables required to solve the heat balance equation are extracted, and necessary intermediate values are computed. The conductor ampacity rating, operating temperature or resistance is computed for the selected points along the power transmission line for the entire time period of the supplied data. Increasing the spatial sampling frequency of points along the line increases the accuracy of locating and assessing the

segments of line that are limiting the overall line ampacity. However, this can incur significant computational penalties in the subsequent optimization process.

3) *Optimization.* To assess the performance of the line upgrading system, statistical measures of the line's ampacity, operating temperature or resistance values are calculated for each sampled point along the transmission line for a given conductor type selection. This provides the upgrade system with the measure necessary to assess a particular point's performance against the overall operating characteristics of the entire line. The measures used for the simulations presented in this section evaluate the potential ampacity of each point against the overall ampacity of the entire line.

The line upgrade configuration is determined by using a GA to find the best conductor selection matching the desired user criteria. The use of a GA permits optimizing the line segment selection without having an explicit mathematical model of the problem, which would be required by classical optimization techniques. Each chromosome encodes a potential line upgrading configuration, matching a conductor type with every sampled point along the transmission line.

4) *Output presentation.* The discovered line configuration is presented to the user in a visual format. Segments of the transmission line are marked out in a Geographic Information System (GIS) application, and the actual gain in ampacity using the optimal upgrade strategy is presented. Statistical measures of the upgrade are also calculated and presented to the user. These outline the overall ampacity gain that would be achieved by performing the presented upgrades, based on the same data used in the upgrading analysis.

4.4.2.2 Optimization Function

To use a GA to identify segments of a transmission line for upgrading, a given transmission line upgrade strategy must first be represented as a chromosome. The selected conductor type for each sampled point i along a transmission line is encoded as a gene in an individual chromosome

$$\text{chromosome}_j = \{c_1, c_2, \dots, c_n\}, \quad (54)$$

where c_i is the conductor type at point i .

An effective fitness function is essential for the GA to find an optimal conducting strategy. To this end, the following criteria were devised to evaluate a chromosome's fitness.

First the average gain in line ampacity is calculated.

$$Ag = \frac{1}{t} \sum_t \left[\min_i A_i^c(t) - \min_i A_i^0(t) \right], \quad (55)$$

where Ag is the average ampacity gain for the upgraded line using the given upgrade configuration, t is the number of time steps in the dataset, i is the i -th sampled point along the transmission line, A_i^c is the ampacity at the i -th point along the conductor using the selected conductor c . A_i^0 is the existing or default conductor ($c = 0$) ampacity at point i .

Next, the net benefit of the selected upgrade must be weighed against the actual costs of performing the upgrade and costs based on the quality of the upgrade configuration. For this, a series of cost functions are used.

The cost of the conductor material and the associated fixed costs for the line upgrade are computed by

$$E^c = \sum_i \begin{cases} P_{c(i)} + F & c(i) > 0 \\ 0 & \text{otherwise} \end{cases}, \quad (56)$$

where E^c is the cost of performing the upgrade reconductoring for the selected segments, P_c is the price of the conductor c selected for the i -th point along the transmission line, and F is the fixed cost associated with performing the conductor upgrade installation for any unit length segment.

A penalty cost is calculated for selecting an upgrade configuration composed of many short upgrade segments scattered along the transmission line.

$$E^s = \sum_i \begin{cases} SC \times \min \left(\exp^{-d(j,j+1)+w}, mf \right) & c(i) > 0 \\ 0 & \text{otherwise} \end{cases}, \quad (57)$$

where SC is the scattered upgrade penalty cost, $d(j, j+1)$ is the distance between a contiguously upgraded segment j and a neighbouring upgraded segment $j+1$, w is the minimum allowable distance between two upgraded segments for which a penalty is substantially reduced or not applied, and mf is the maximum scattered upgrade penalty factor.

A penalty cost is also assessed for switching between conductor types in a contiguous segment of line chosen for upgrading.

$$E^u = \sum_i \begin{cases} P_s & c(i) \neq c(i+1) \wedge c(i) > 0 \\ 0 & \text{otherwise} \end{cases} \quad (58)$$

where E^u is the total conductor switch penalty cost, and P_s is the unit penalty cost of switching to a different conductor type.

To ensure that the system achieves a configuration acceptable by the user, constraints are incorporated into the GA optimization process in the form of “large” penalty cost(s) E^p , should they not be satisfied.

From the above measures, the net fitness is computed.

$$F = \frac{Ag}{E^c + E^s + E^u + E^p} \quad (59)$$

where F is the net fitness value of a given chromosome’s upgrade configuration.

The chromosome’s fitness value F can also be computed as the net Return on Investment (ROI), based on the incremental profit P from the additional amount of energy that can be transmitted and sold over the upgraded line, less the incurred upgrade costs

$$F = P - (E^c + E^s + E^u + E^p). \quad (60)$$

This study presents only the results of using the above described objectives. However, the same methodology can be easily adapted to optimize the segment selection algorithm for other criteria. Other possible goals, that can be specified for upgrading with the presented system include:

- Minimizing the average or maximum conductor operating temperature.
- Maximizing the average or minimum transmission efficiency.
- Minimizing the average or minimum conductor sag.
- Minimizing conductor aging.

4.4.2.3 Case Study

To evaluate the line upgrading decision support system, a set of constraints was selected. These constraints include: upgrading the line for the best ratio between the maximum average ampacity gain and the minimum cost (M/M), three different minimum average ampacity gains (5 A, 50 A, and 100 A), and a ROI optimization.

To test the proposed approach of finding transmission line segments that need to be upgraded based on average ampacity criteria, two lines were selected: one operated by Newfoundland and Labrador Hydro (NLH) in the Province of Newfoundland and the second operated by AltaLink in the Province of Alberta. These two transmission lines are depicted in Figures 50 and 51 in Section 4.4.2.4. Performing the upgrading study on these two lines provides an opportunity to evaluate the system performance on transmission lines situated in vastly different terrain and subject to different climatology. The former is located very close to the sea coast, while the latter is located in

mostly prairie land. In the conducted simulations, it was assumed that both of these transmission lines use the Drake conductor, which is described in Table 34. The number of spatial samples for the Alberta line is significantly larger (971) compared to the TL-201 line (369). To lessen the computational burden of the large number of samples, the system was configured to choose only two candidate upgrade conductors for the Alberta line, as opposed to three for the TL-201 line.

To test and evaluate the second proposed approach of finding transmission line segments which provide the best ROI, the BC Hydro transmission line 5Lo11, depicted in Figure 52, was selected. It was assumed that this transmission line uses the Finch conductor. The intelligent upgrade system was configured to choose only one possible upgrade conductor, BlueBird. The system was then configured to discover transmission line segments for upgrading that provide the maximum ROI over a ten year period using the method described in the previous section.

The NARR historical dataset [83] was spatially and temporally interpolated to provide the meteorological data for the line thermal model. This dataset comes in the form of meteorological variables defined on a 32-km horizontal grid, derived from NWP forecasts and assimilated weather observations. Using this interpolated dataset provided a time-effective method of obtaining the meteorological conditions necessary to compute the transmission line operating characteristics. Line ampacities were computed for each hour in the period spanning the years of 2000 to 2009, inclusive.

The assumed upgrading costs and penalties are described in Table 22. It is important to note that, for actual real-world use, the utility must specify actual upgrade costs, in order to obtain a reliable assessment of which seg-

Table 21: Conductor indices used in the intelligent line upgrade segment selection system. The conductors' physical parameters are listed in Table 34 of Appendix B.

Conductor	Index
Drake	0
Finch	1
Dipper	2
BlueBird	3

Table 22: Assumed transmission line upgrading costs used in the line upgrading GA fitness function.

Item	Cost
Fixed Upgrade Cost [$\$.km^{-1}$]	13048.80
Drake [$\$.km^{-1}$]	12382.87
Finch [$\$.km^{-1}$]	16263.94
Dipper [$\$.km^{-1}$]	19137.43
BlueBird [$\$.km^{-1}$]	32376.08
Switch Conductors Penalty [\$]	20,000.00
Scattered Upgrade (SU) Penalty [\$]	200,000.00
SU Dist. [samples]	5
SU Maximum Penalty Factor	100

ments are most economical to upgrade and, hence, to get the best gain from a given line upgrade venture. The GA was configured with the parameters listed in Table 23.

The transmission line upgrade system results for the NLH TL-201 power line are presented in Table 24, the results for the selected AB power line are presented in Table 25, and the results for the BC Hydro 5L011 Line are pre-

Table 23: GA parameters used for the presented line upgrading study.

Parameter	Value
Population Size	1000
Minimum Num. Generations	600
Maximum Num. No-change Generations	300
Crossover Rate	0.4
Mutation Rate	0.2
Gene Mutation Rate	0.15

sented in Table 26. These tables highlight the additional amount of ampacity that a DTCR equipped line is able to carry after performing the upgrading suggested by the system. It highlights the overall line average ampacity gain, as well as the greatest gain for any single point along the line. It also shows the fraction of overall line length line that would need to be upgraded to attain the presented increase in capacity.

Visually, three examples of the suggested upgrades are provided for the lines in Figures 50, 51, and 52. Each selected segment for upgrading along the transmission line is marked with a conductor index number. This number corresponds to the conductor type enumerated in Table 21. Figure 53 shows an example of the convergence of the GA optimization algorithm to the optimal upgrading configuration.

4.4.2.4 *Analysis*

It is evident from the results of the simulations performed on the transmission lines that the system is indeed capable of finding an upgrade strategy to increase the capacity of the respective lines. For each minimum upgrade ampacity specified, replacing the conductor for the identified segments of the transmission line does in fact increase the ampacity with an average gain exceeding the minimum requirement specified by the user. Based on this result, it can be inferred that there are in fact certain segments of the transmission line that more frequently pose a capacity bottleneck on the transmission line compared to other parts. Hence, replacing the line conductor at the flagged locations will increase the overall transmission line capacity when coupled with DTCR system. Performing a ROI for a period of just ten years, yields an upgrade configuration covering only 2.2% of the transmission line while at

Table 24: Increase in the NLH TL-201 transmission line capacity after a suggested line upgrade.

Requested Upgrade	None	M/M	5 A	50 A	100 A
Average Point Ampacity [A]	1779.20	1784.30	1841.07	1946.06	1983.92
Maximum Point Ampacity [A]	3628.57	4835.04	6754.06	6982.76	6967.17
Average Line Ampacity [A]	1323.97	1325.24	1347.24	1394.41	1445.77
Maximum Line Ampacity [A]	3041.04	3041.04	3041.04	3044.08	3184.20
Average Line Ampacity Gain [A]	0	1.27	23.27	70.44	121.80
Fraction of Line Upgraded [%]	0	0.81	7.59	19.24	33.06

Table 25: Increase in the given AB transmission line capacity after a suggested line upgrade.

Requested Upgrade	None	M/M	5 A	50 A	100 A
Average Point Ampacity [A]	1651.94	1652.29	1666.78	1675.22	1727.12
Maximum Point Ampacity [A]	2873.92	3827.86	3947.19	3947.19	3947.19
Average Line Ampacity [A]	1188.31	1194.60	1216.76	1276.42	1290.34
Maximum Line Ampacity [A]	2050.68	2050.68	2066.96	2214.27	2214.27
Average Line Ampacity Gain [A]	0	6.29	28.45	88.11	102.04
Fraction of Line Upgraded [%]	0	0.10	3.40	5.36	15.45

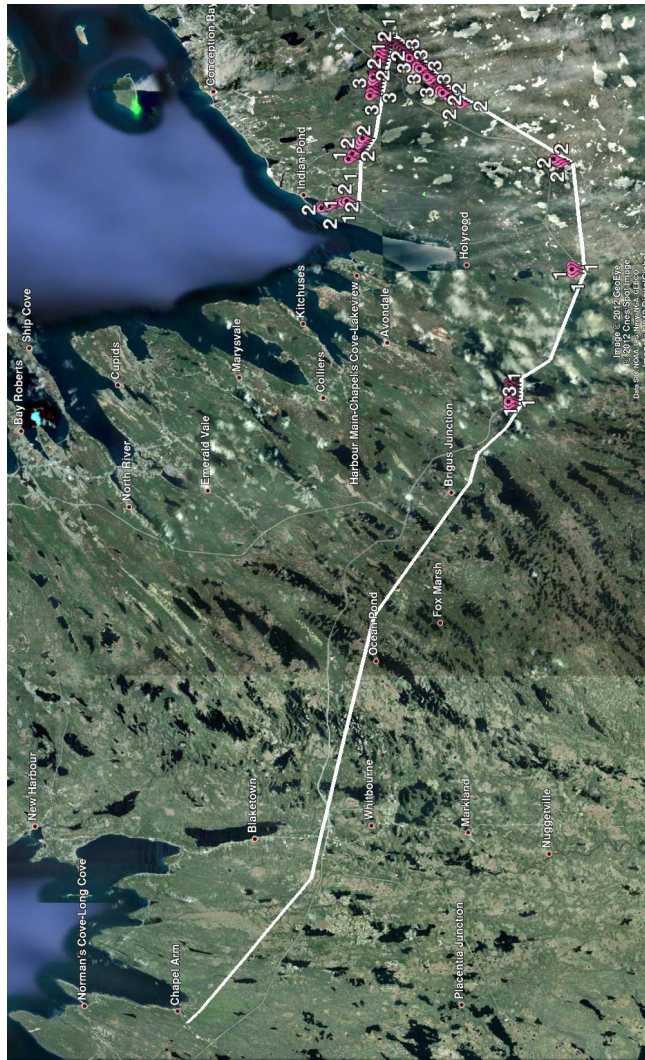


Figure 50: The NLH TL-201 transmission line used for the line upgrade system evaluation study. The numbers beside the transmission line indicates that the given segments have been selected for upgrading with the respective conductor type to increase the average line ampacity by a minimum of 50 A.



Figure 51: The AB transmission line segment used for the line upgrade system evaluation study. The numbers beside the transmission line indicates that the given segments has been selected for upgrading with the respective conductor type to increase the average line ampacity by a minimum of 50 A.

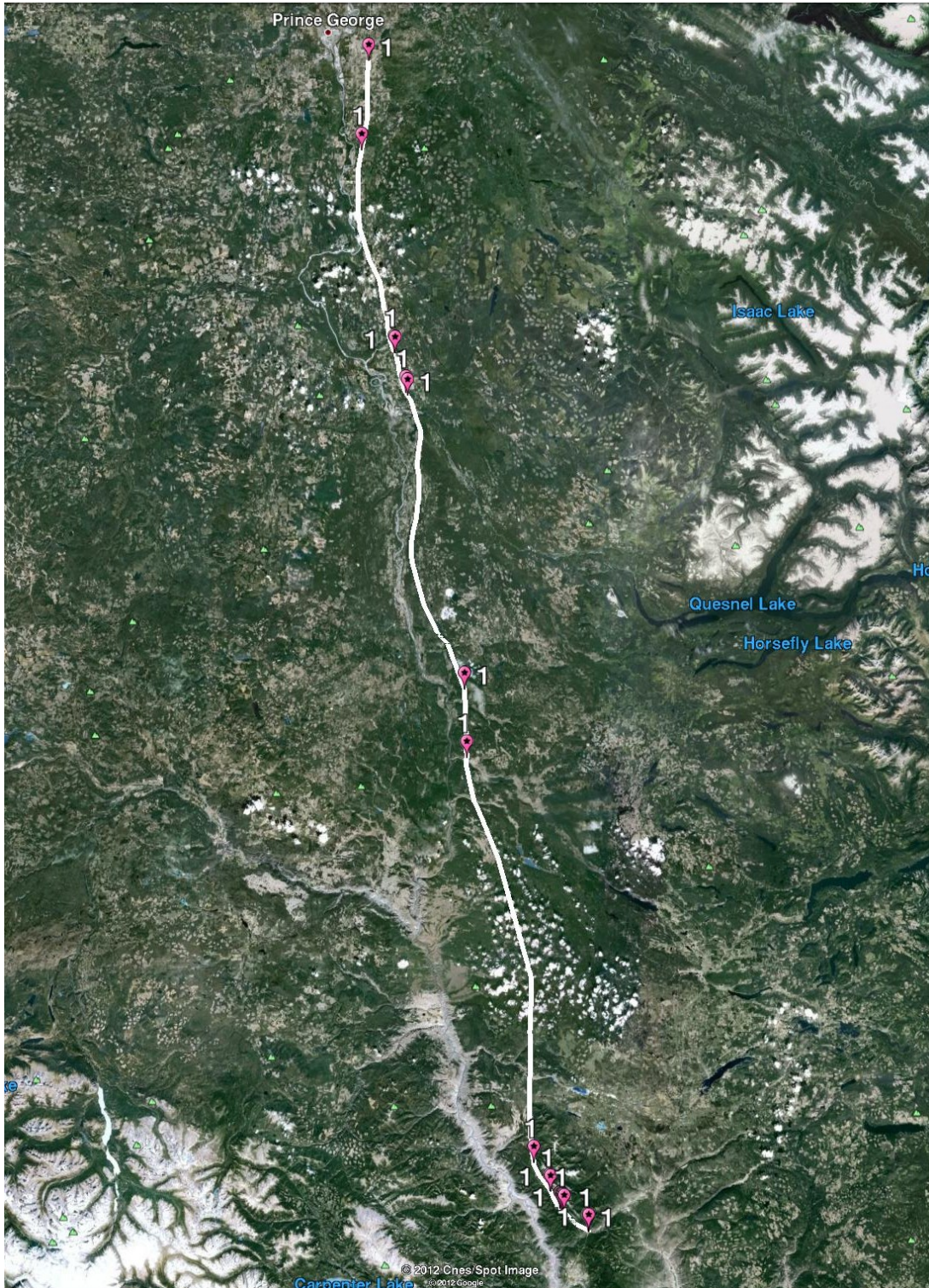


Figure 52: The BC Hydro 5Lo11 transmission line used for the line upgrade system evaluation study. The numbers beside the transmission line indicates that the given segments have been selected for upgrading with the respective conductor type to maximize the ROI from upgrading.

Table 26: Increase in the BC Hydro transmission line 5L011 capacity after a suggested line upgrade.

Measure	Original	Upgraded
Average Point Ampacity [A]	1993	2017
Maximum Point Ampacity [A]	3867	5575
Average Line Ampacity [A]	1425	1455
Maximum Line Ampacity [A]	2399	2671
Average Line Ampacity Gain [A]	0	30
Fraction of Line Upgraded [%]	0	2.2

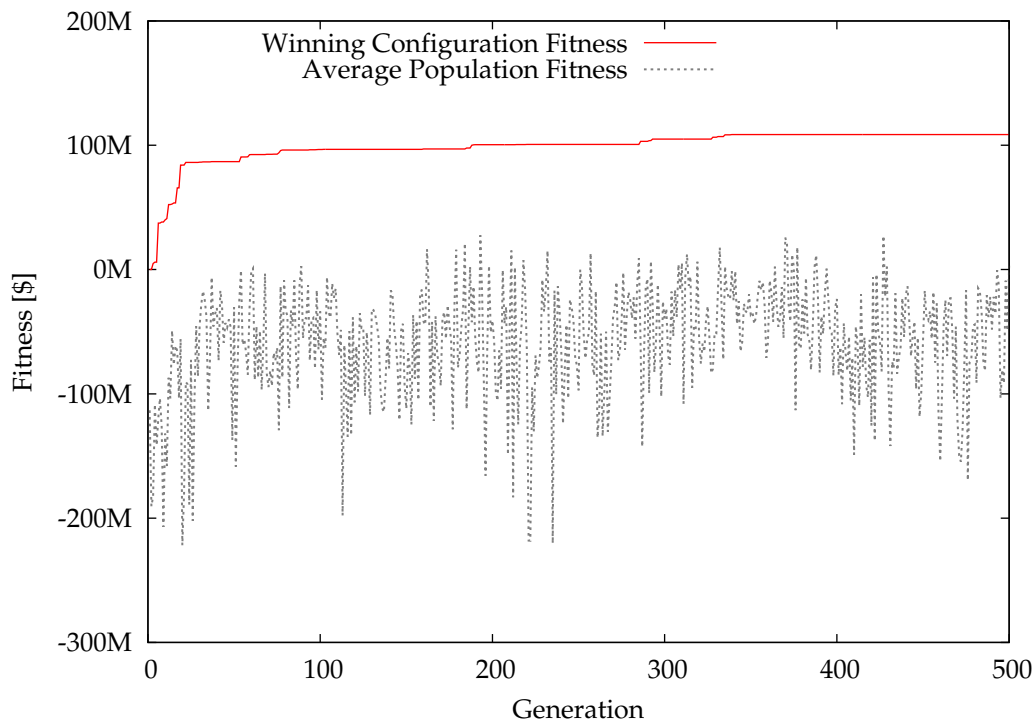


Figure 53: GA population fitness value trend. The solid line shows the fitness value of the winning upgrade configuration at each respective generation. The dotted line shows the overall average fitness value of all elements in the population.

the same time providing an average ampacity gain of 30 A. This indicates that there are opportunities for low-cost upgrades that will yield substantial benefits.

During operation, the selected segments would significantly reduce the amount of power that could be transmitted over the line if the worst-case conditions were to repeat. If these sections are not detected due to lack of sensors or due to approximations taken in the transmission line ampacity estimations, they could compromise the transmission line integrity. The segments of line could suffer from accelerated aging, or in the worst case, cause a safety hazard leading to environmental and/or property damage.

It is important to note that the system is capable of finding an upgrade strategy in so far as the physical layout of the transmission line allows for it. The upgrading system is not able to overcome the physical limits imposed by the climatology and the line positioning. As is evident in the maximum ampacity gain for the minimum upgrade cost results, if there is no small subset of transmission line that can be upgraded to give a substantial increase in capacity, the system will fail to find an upgrade strategy. For average line ampacity optimization, the presented system is capable of finding an upgrade strategy only if a small segment or segments of the transmission lines pass through region(s) that consistently provide suboptimal operating conditions. If such regions do not exist, there is no “silver bullet” to solve the problem.

Another worthy observation is that, even if a transmission line does not employ DTCR technologies, benefits of using the system can still be obtained. As the identified segments pose the greatest capacity limitation, their operating temperature will be the highest with respect to the rest of the transmission line. As a result, replacing the conductor would reduce degradation of the

aluminium conductor from unintentional overheating when the transmission line is operated at the assumed static limit, and the limiting segments have an ampacity lower than the static limit. The reason for this possibility is the fact that typical static rating procedures [103] assume a near-worst-case operating condition. There is a margin of error for which the actual line rating will be less than the static rating. The proposed system is capable of identifying such conditions and providing an upgrade strategy to ensure that the transmission's ampacity is at or above the static rating as often as possible. Additionally, efficiency of the transmission line will be increased due to lower operating temperatures and hence, lower conductor resistance.

While not explicitly evaluated and presented, the upgrading system is also capable of being used to select the optimal conductor strategy for a new transmission line. This mode of operation requires that the default conductor (i.e. with index zero) have a non-zero cost specified. Next, the cost of performing the upgrade should be replaced with the cost of constructing each respective line segment and applied to all conductors. Subsequent operation of the system would be identical to the methodology described above. This method of selecting conductors would provide the most cost effective strategy to ensure that desired minimum operating criteria are met, while minimizing the material costs from using over-specified conductors. It will also increase the stability of the system by minimizing segments with suboptimal operating characteristics.

4.4.3 Reduction of Power Generation Emissions by Using DTCR

Existing power transmission lines were generally not designed and built with sparsely distributed, renewable generation sources in mind. Thus they frequently are not rated to carry the additional amount of energy that could be generated. However, as mentioned in Section 2.1.4, the majority of existing power line ratings are based on conservative estimates of the near-worst-case ambient weather conditions. Since these extreme case conditions occur infrequently, DTCR systems can unlock valuable capacity based on actual rather than assumed extreme conditions. Additionally, the ideal conditions for wind power generation are also the conditions which will provide the highest line capacity. Hence, it should be possible to incorporate more green energy into the existing power grid without incurring significant costs.

The following study illustrates the offset in emissions that would be gained by importing additional clean power through an existing saturated transmission line utilizing a DTCR system, rather than relying solely on conventional polluting power sources. It also illustrates the potential of constructing even larger renewable generation facilities that would add more clean energy onto the existing infrastructure.

4.4.3.1 *Power Generation Emissions*

The net GHG and pollution emissions resulting from the operation of power generation stations come from four main components: the initial emissions related to the acquisition of raw materials and the construction of the power

A version of this subsection has been published in [108]. I made a substantial contribution to the material of this publication. I also wrote a major portion of the published manuscript.

Table 27: Average GHG emissions released by electric power generation technologies over the plant life cycle.

Technology	Avg. CO₂ per kWh
Wind	3 – 22 g
Hydro	4 g
Nuclear	6 g
Photovoltaic Solar	60 – 150 g
Natural Gas	430 g
Coal	800 – 1050 g
Wood	1500 g

plant; the emissions associated with the procurement, refinement and utilization of the fuel (if applicable); any emissions associated with maintenance operations; and finally emissions from the decommissioning of the power plant [109]. As shown in Table 27, over the entire lifespan of a power plant, wood-fired plants release the greatest amount of carbon dioxide per kilowatt of power produced of all the power generating sources. Coal-fired plants are the second most polluting source, when it comes to CO₂ emissions. However, due to the large number of technologies on the market, from a simple steam generator to the latest generation super-critical boilers, there is a relatively large range in the emission levels. Furthermore, the type of coal that is burned has a significant impact on the amount of GHG emissions. At the opposite end of the spectrum, wind energy can be the cleanest source, with net emissions of as little as 3 grams of CO₂ per kWh of electricity. As with coal-fired plants, given the wide range of technologies available on the market and the locations selected for specific installation, the emission figures can vary considerably. The next cleanest source of energy is hydro, with only 4 grams of CO₂ per kWh of produced energy. Given the energy intensive process of refining silicon for solar panels, photovoltaic solar results in emissions ranging from 60 to 150 grams of CO₂ per kWh, based on the entire plant life.

Table 28: Major pollutants released by coal-fired power plants per kWh during power generation.

Compound		Avg. Emissions per kWh
Carbon Dioxide	CO ₂	371.95 g
Sulfur Oxides	SO _x	2.72 g
Nitrogen Oxides	NO _x	1.81 g
Methane	CH ₄	476.27 g
Mercury	Hg	4.08×10^{-7} g

Given the prominence of coal-fired power plants in the generation mix of many countries, both in terms of capacity and actual energy generated, Table 28 provides a detailed description of the various GHG and pollutant emissions of coal power plants, based on combustion emission figures in [110]. These values only quantify emissions released from actual power generation and they do not take into account indirect emissions associated with a plant's construction, maintenance and decommissioning. This table illustrates the substantial carbon dioxide and methane footprint of coal power generation sources.

4.4.3.2 Case Study

The scenario presented in this case study is modelled on the situation in the Province of Alberta, Canada. The power transmission infrastructure in Alberta has not been significantly upgraded in the last few decades and is in need of significant investment [111]. The City of Edmonton, one of two major urban centres in the Province, has a peak summer power consumption of 1186 MW and a peak winter consumption of 1151 MW, based on 2009 figures provided by the Alberta Electric System Operator (AESO). Peak consumption is projected to grow to 1581 MW by 2019 [112]. Province wide, the Alberta

Internal Load (AIL) peak consumption is expected to grow from 9846 MW, to 14759 MW by 2019. In the face of this expected growth in load, existing transmission infrastructure is inadequate for any major generation capacity expansion without significant investments in upgrades and new line construction. At the same time, the Government of Alberta is pushing for new renewable energy sources. As a result, the current capacity of 629 MW of wind power is expected to grow by 7400 MW in the next decade [113].

Of the numerous power plant construction projects planned for the province, two new 150 MW wind farms are scheduled to be constructed in the vicinity of Edmonton: the Ponoka Wind Project and the Chigwell Wind Project. To incorporate these and other new green generation sources, transmission asset owners are in the final stages of planning a massive overhaul of the entire province's transmission grid [114]. However, these upgrades will cost billions of dollars and delay the introduction of new clean energy sources.

This leads to the following question: can the existing power transmission grid integrate new green power generation sources, thus contributing to pollution reduction without substantial investment? If so, what is the optimum capacity of the planned wind farms if they were to be connected using the existing transmission and/or distribution lines?

For the purpose of this study, several assumptions are made. The simulation uses a simplified transmission network, illustrated in Figure 54. In this scenario, the power is supplied to the consumers, both for the metropolitan area and neighbouring rural communities by the base load generator, i.e. the Genesee power station. The generators are connected to the customers by a 240 kV transmission circuit using a "Drake" conductor. This conductor

can carry a nominal current of 907 A at a maximum operating temperature of 75 °C. Detailed parameters of the conductor used in the simulations are listed in Table 34 of Appendix B. A constant power factor of 0.9 is assumed.

The two wind farms are modelled to each be composed of 50 Vestas V90 3 MW VAS wind turbines. This 3 MW turbine has a $4 \text{ m}\cdot\text{s}^{-1}$ wind speed cut in, reaches its rated power output at a wind speed of $15 \text{ m}\cdot\text{s}^{-1}$, and cuts out at a wind speed of $25 \text{ m}\cdot\text{s}^{-1}$. The power curve for this turbine is presented in Figure 55. The study also assumes that the wind farm production is not curtailed, i.e. that all available wind energy is harnessed and supplied onto the power grid.

Two operating cases are simulated. In the first scenario, the power transmission line is operated at 100% capacity, based on the transmission line's static rating, with power being transmitted to the major metropolitan area and the neighbouring communities. The amount of additional power that could be supplied onto the power grid using DTCR is assessed, and the reduction in GHG and pollution emissions is quantified. In the second scenario, the size of the wind farms that can saturate the power lines if they were using DTCR technology is calculated. This is done to illustrate the optimal size of the wind farms that could be constructed and integrated using the existing infrastructure and DTCR systems.

In order to calculate the ampacity of the transmission line and to determine the wind power output, a historical weather dataset is required. For this purpose, the NARR historical dataset [83] was used. To reduce the computational burden of performing this study, ampacity values were calculated for every three hour sampling interval provided by the NARR dataset. An NWP hindcast was not performed to generate 10 minute weather data, as this



Figure 54: Simplified power transmission scenario used for the simulations performed in this study.

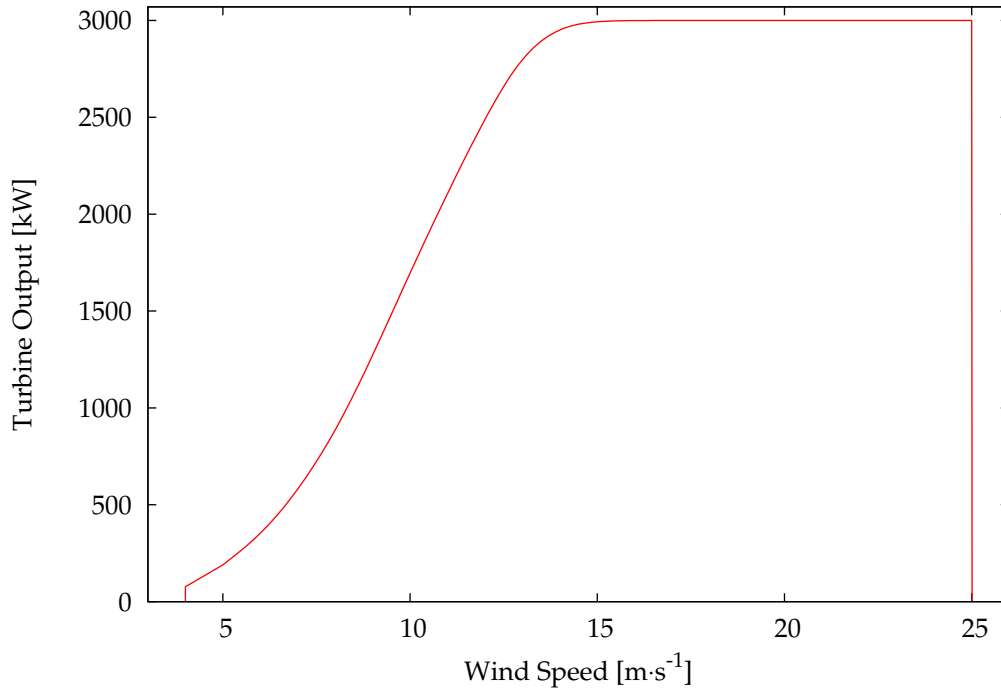


Figure 55: Power curve for the wind turbine model used in this study. The turbine has a cut in wind speed of $4.0 \text{ m}\cdot\text{s}^{-1}$ and a cut out speed of $25 \text{ m}\cdot\text{s}^{-1}$.

study is concerned with long-term operational averages rather than real-time operating conditions.

A subset of this dataset was extracted for the region covering the scenario illustrated above, for the period spanning the year 2009. To improve the accuracy of the modelled output, the source dataset was first spatially interpolated using numerical interpolation methods provided by WRF Preprocessing System (WPS) to a finer resolution of 3.2 km.

To determine the line ampacity, the relevant meteorological variables required to solve the heat balance equation were extracted from the interpolated dataset. All necessary intermediate values were computed. Using the thermal model equation, presented in Section 4.1, the current required to

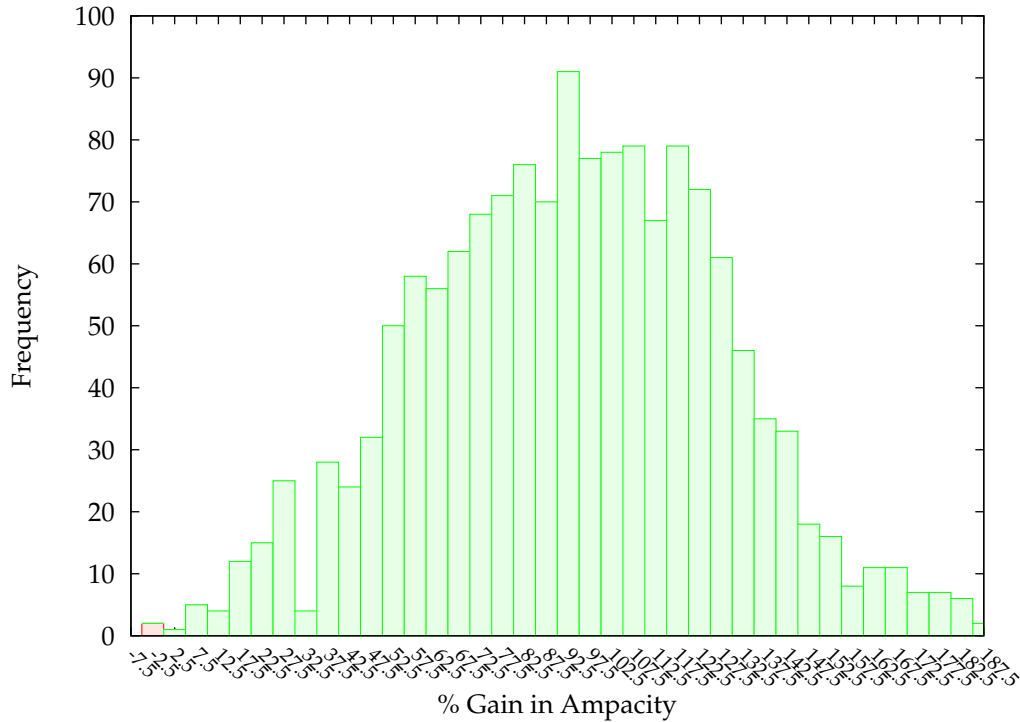


Figure 56: Distribution of the ampacity gain at a given sample point on the line for the six summer months, May to October.

reach a maximum temperature of 75°C was calculated for every three hour interval in the dataset.

Likewise, the wind farm power output was determined by calculating the turbine output, using the power curve shown in Figure 55, for the wind speed present at the two respective locations.

The increase in available capacity using a DTCR system is illustrated in Figures 56 and 57. The former shows the gains for the summer months, i.e. May to October, for a point on the transmission line and the latter illustrates the gain for the winter period, i.e. November to April. For the entire transmission line segment, on average, the gain in available capacity is 880.88 A. In the best case scenario, a gain of 1956.17 A over the static rating is achieved. However, in the worst case, there is a loss of 194.9 A in capacity.

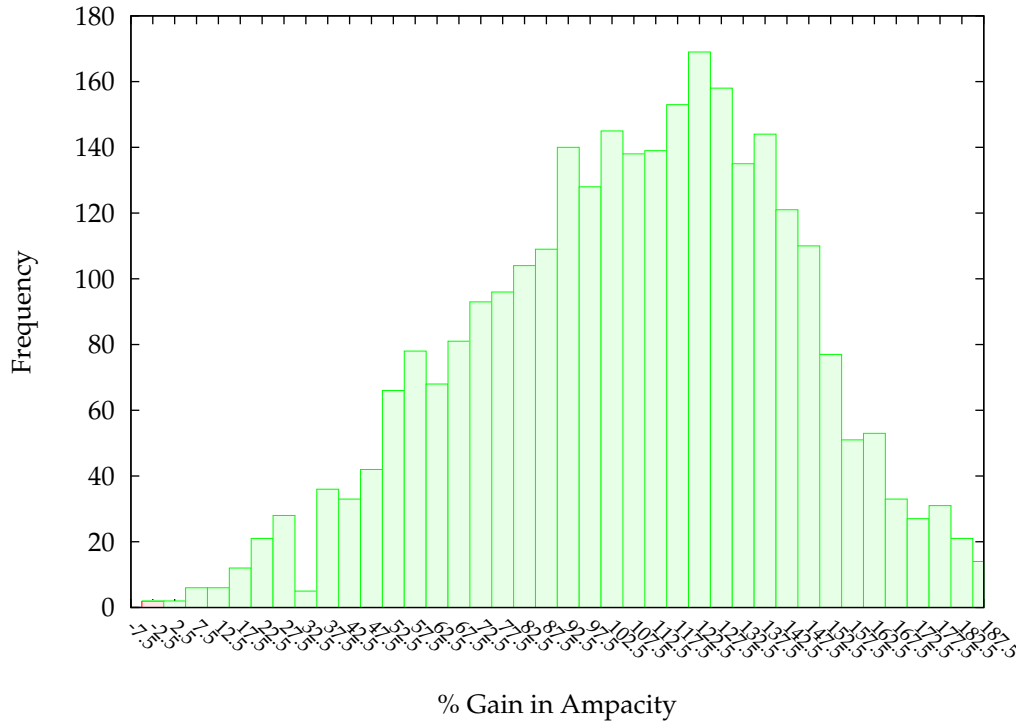


Figure 57: Distribution of the ampacity gain at a given sample point on the line for the six winter months, November to April.

The distribution of the potential amount of power generated by each turbine for the year 2009 for the Ponoka and Chigwell sites is shown in Figures 58 and 59, respectively. Additionally, Figures 60 and 61 show time series of the potential amount of power that could have been generated throughout the year.

On average, the two wind farms can supply an additional 94.36 A of current onto the line. Considering the determined line ampacity, this figure is reduced slightly to 94.34 A. To assess the size of the wind farm that could be constructed and how much of its output could be supplied onto the grid, Figure 62 illustrates the additional amount of current that could be generated and then carried by the transmission line from the wind farms with respect to the number of turbines per installation.

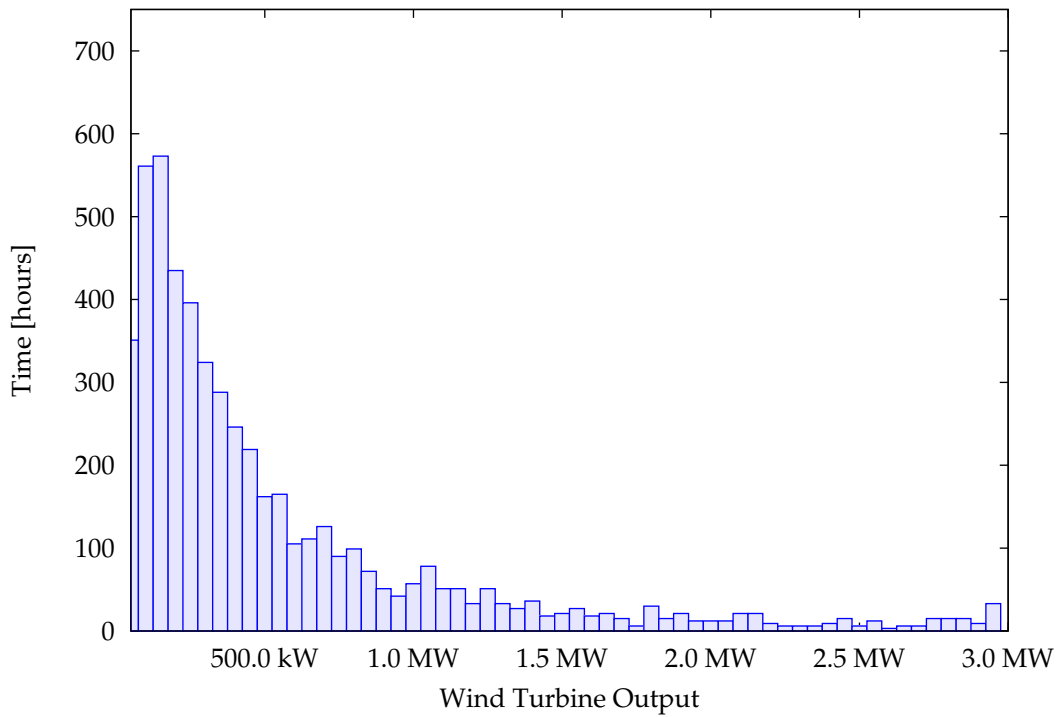


Figure 58: Distribution of the amount of potential power generated by a single turbine for the Ponoka site, based on the 2009 NARR meteorological data.

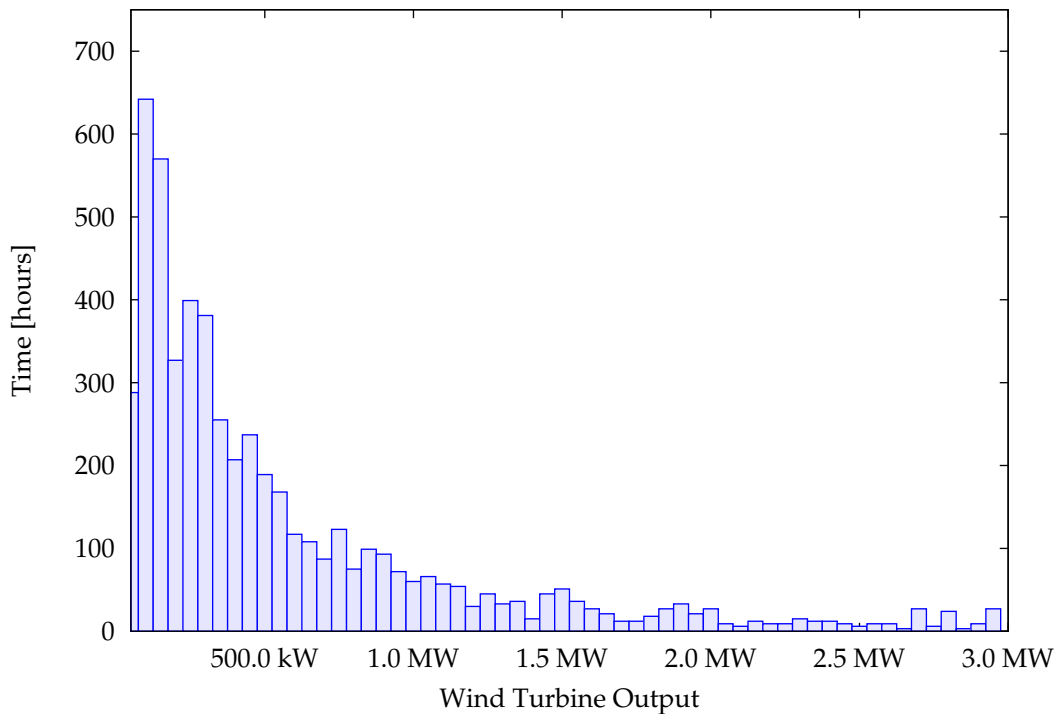


Figure 59: Distribution of the amount of potential power generated by a single turbine for the Chigwell site, based on the 2009 NARR meteorological data.

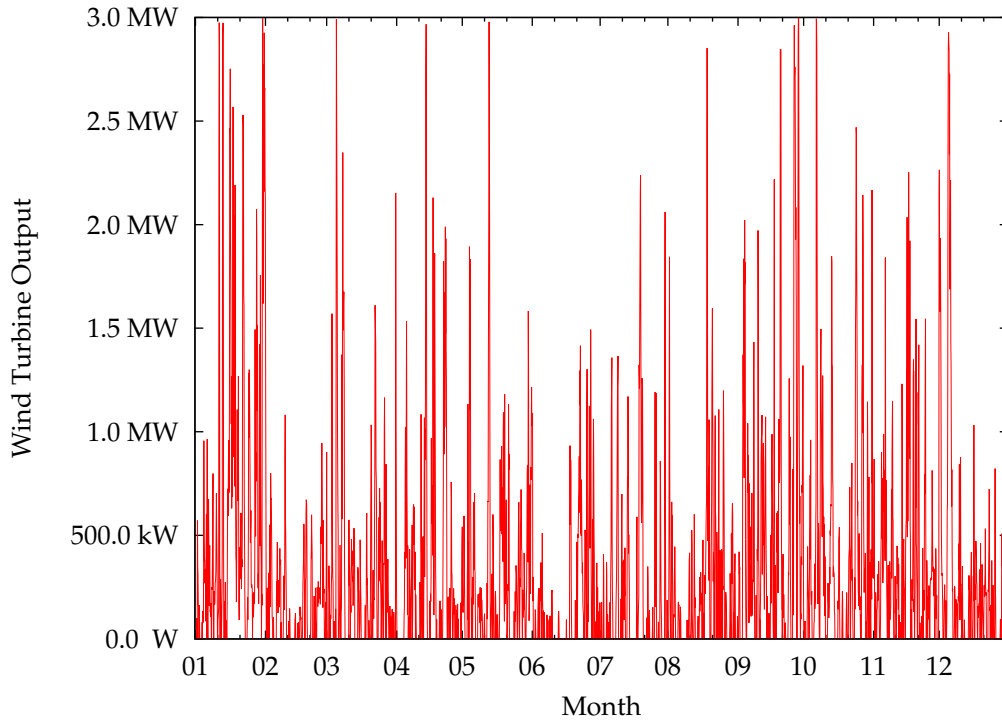


Figure 60: Amount of potential power generated by a single turbine for the Ponoka site, based on the 2009 NARR meteorological data.

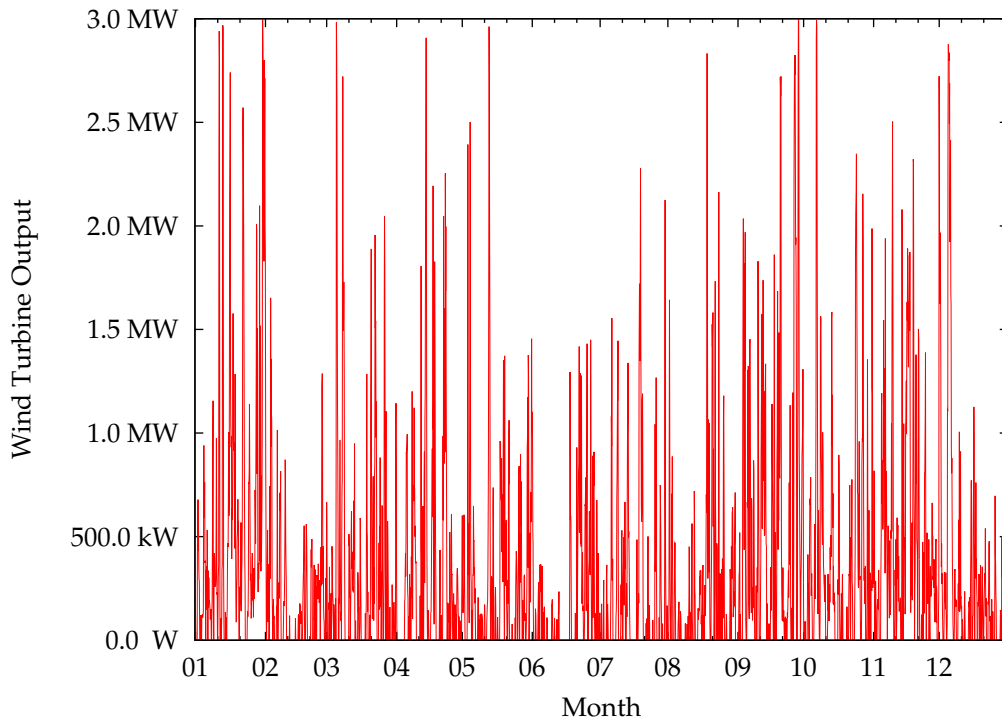


Figure 61: Amount of potential power generated by a single turbine for the Chigwell site, based on the 2009 NARR meteorological data.

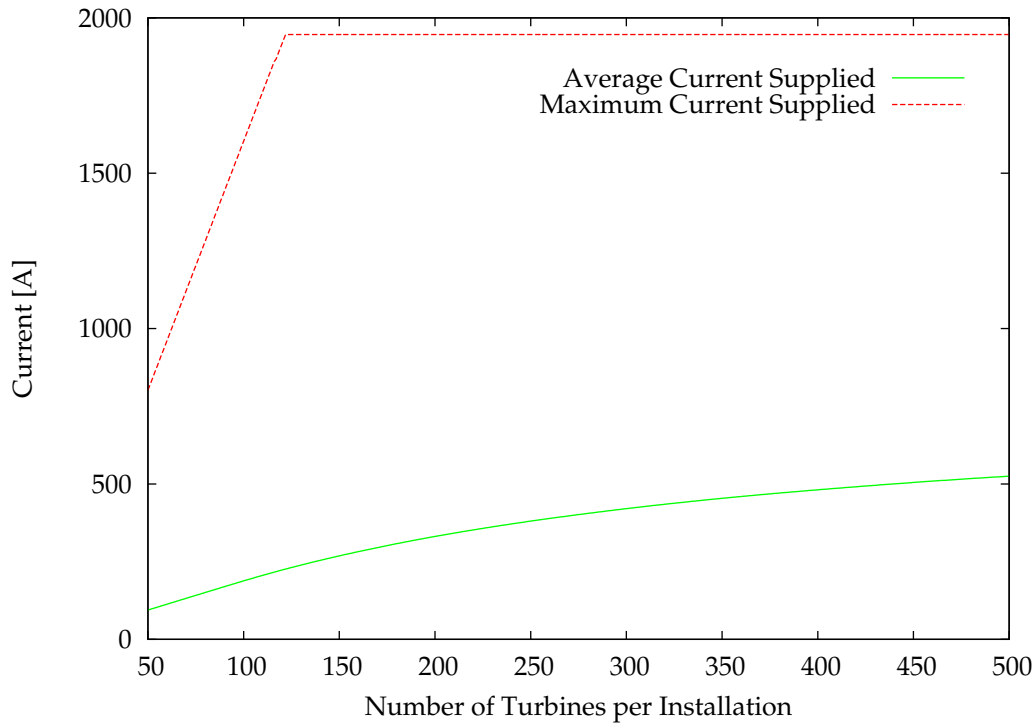


Figure 62: Amount of current supplied and carried by the transmission lines with respect to the number of turbines and available line capacity.

4.4.3.3 *Reduction in Emissions*

For the considered scenario, the reductions in the pollutant emissions of a typical coal-fired power plant are presented in Table 29. This table illustrates the average and peak reduction in emissions by connecting the two wind farms to a saturated transmission line and using DTCR to harness the excess capacity, based on the simulated operating conditions.

4.4.3.4 *Analysis*

The simulated gains in available capacity for the transmission line between the proposed wind farm locations and the city are substantial. This is due to two factors. First, given the fact that the transmission line follows a relatively straight path, both in the simulated scenario and the real world configuration,

Table 29: Reduction in GHG emissions gained by using DTCR systems.

Compound	Emissions [$\text{t}\cdot\text{h}^{-1}$]	
	Avg	Max
Total Carbon Dioxide	28.13	239.10
Carbon Dioxide	13.13	111.59
Methane	16.81	142.88
Sulfur Oxides	0.096	0.82
Nitrogen Oxides	0.064	0.54
Mercury	1.44×10^{-8}	1.22×10^{-7}

the angle between the wind direction and the axis of the line is generally the same. This reduces the cases where a short section of transmission line will be subject to parallel or near parallel wind flow, while the remainder of the transmission line benefits from a perpendicular airflow. Next, the topography of the considered region is relatively flat. This also reduces the potential bottlenecks if the line passed through an area that is prone to poor cooling conditions.

It is evident, based on the histograms of the turbine outputs for both wind farm locations, that, for the majority of the wind conditions throughout the year, they would generate less than one third of their rated capacity. During most operating conditions, the actual output is an order of magnitude less than the rated turbine output. On average, a turbine located at the Chigwell site produces 365 kW of power, and a turbine located at the Ponoka site produces 341 kW. This provides a substantial opportunity to include a much larger number of wind turbines and connect them onto an existing grid without causing congestion issues. The optimal sizing of a wind farm can be estimated by analyzing the fraction of power generated and then transmitted over the existing power line with respect to the number of wind turbines at a given installation. For the case study, this relationship is shown in Figure 63.

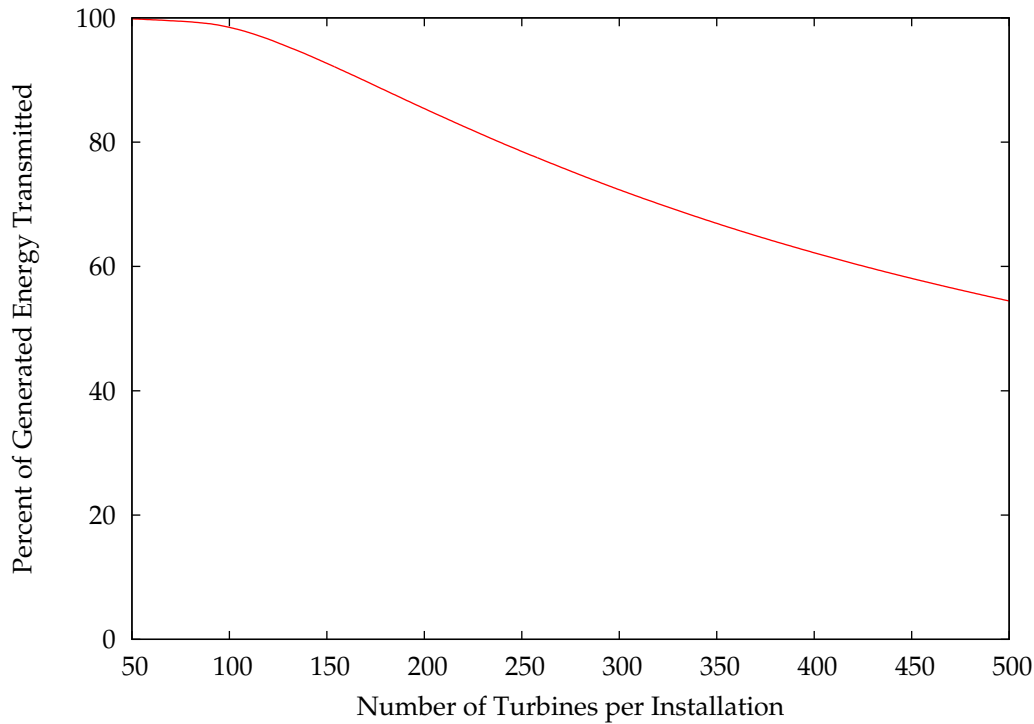


Figure 63: Fraction of total generated energy carried by transmission line with respect to wind farm size.

Thus, using DTCR equipment and constructing a much larger wind farm can result in a significant reduction in GHG and pollution emissions.

4.5 SUMMARY

This chapter presented a new precipitation-based conductor cooling model for use in DTCR systems. It has also established the optimal sampling interval of weather data for use in DTCR systems. Furthermore, it has presented a study which assesses the accuracy of using a NWP model to predict available line capacity. Finally, this chapter presented a number of novel applications for deploying and managing power transmission infrastructure.

The enhanced line thermal model extends the heat balance formulation provided by IEEE Std. 738-2006. It improves estimates of heat loss to the environment from overhead transmission lines during periods of precipitation, permitting more accurate calculations of line temperature. The precipitation-cooling calculations rely on estimation of water mass flux from falling and wind-blown precipitation, calculation of evaporation rate under specified atmospheric and line loading conditions, and computation of the amount of heat required to warm and evaporate the water. Water from snow and rain precipitation is heated and evaporated mostly with heat from the transmission line, thereby cooling the line and leading to lower line temperatures and greater ampacity. Under typical rainfall conditions observed for the year 2010, line temperature measurements indicate that up to a few degrees of additional line cooling can be observed during periods of precipitation. This observation correlates well with the results of the enhanced model. Furthermore, tests with the model show that, for a given conductor, ampacity gains of tens of amperes are possible during periods with low precipitation rates, and over 400 A for rainfall exceeding $14 \text{ mm}\cdot\text{h}^{-1}$. Should a transmission line be fully loaded while precipitation is falling, significant additional line capacity can potentially be achieved.

The IEEE Std. 738-2006 thermal model was tested to assess the effect of instantaneous vs. averaged meteorological inputs, and various update frequencies, on the calculation of conductor temperature and ampacity. The frequency of occurrence of temperatures exceeding recommended values, caused by ampacity determination errors, is about 1.6% when 60-minute averaging intervals are used, compared to only 0.01% for 10-minute intervals. Based on these results, the use of 10-minute averaged values of meteorolog-

ical inputs is recommended for weather-based thermal rating systems. In any case, averaged values are preferable to instantaneous measurements or predictions.

The NWP ampacity forecast verification study showed substantial promise for the use of NWP models for DTCR purposes; however, additional research work is required to capitalize on the ampacity gains that can be achieved. A large majority of forecast ratings are within an acceptable tolerance. However, 29.5% of the forecast values would cause the conductor temperature to exceed acceptable safe limits, should the full forecast ampacity value be utilized. Nevertheless, using only 75% of the forecast rating may provide acceptable risk. Reducing the forecast ampacity by 25% still provides a significant increase in line capacity over the static rating, while diminishing the risk of overheating the conductor to approximately 5%.

The last section of this chapter introduced three applications of DTCR technology. The power line routing system is based on finding a line placement that optimizes a user's criteria, by specifying the optimal line operating characteristics. First, operational parameters are determined for each possible line segment joining two adjacent nodes in a spatial grid covering the potential construction area, over an extended period of time. Subsequently, statistical measures of the line segment's operating characteristics are computed. A graph search algorithm is then employed to find a line positioning within the grid that meets the desired objective.

The line upgrading system identifies segments of transmission line that are in greatest need of an upgrade, based on user specified criteria. As in the previous case, operational parameters are first determined for a series of points sampled along a transmission line, over an extended period of time. A GA-

based optimization algorithm is then used to identify the segments along the line that limit the available line capacity and whose upgrading will meet or exceed the given constraints. This reduces the reliance on subjective human analysis and intuition. By performing the suggested upgrade strategy, the capacity of existing transmission lines utilizing DTCR systems can be expanded in an optimal way. This makes it possible to avoid or minimize expensive power line construction projects and full-scale upgrades.

Based on the emission reduction study, it is clear that DTCR systems allow for the inclusion of higher capacity renewable generation sources, without costly infrastructure upgrades. A significant reduction in emissions can be achieved by incorporating DTCR systems into existing transmission networks alongside green energy sources. Additionally, using this technology permits the construction of more substantial renewable energy installations, further reducing emissions and allowing for more energy to enter the grid than would otherwise be possible using conservative static ratings.

5 | CONCLUSIONS

This thesis presents research work that couples modern, high resolution Numerical Weather Prediction NWP models (or other sources of high resolution meteorological data) with methods of computational intelligence. The result of this work is a significant enhancement of an existing freezing rain and a conductor thermal rating model, and the development of a set of novel decision support systems, using Dynamic Thermal Circuit Rating (DTCR), for the power transmission industry. The enhanced models and developed systems provide the industry with a set of advanced tools to support both daily operations and long-term planning.

5.1 CONTRIBUTIONS

The conducted research work contributes to a number of important theoretical and practical advances in several areas, including meteorology, electric power engineering, and the environment. To further the ability to predict adverse weather conditions, the following contributions are made:

- Ice Accretion Forecast System (IAFS) is optimized using a Genetic Algorithm (GA) optimization technique to increase its predictive accuracy

- IAFS is evaluated on a range of different ice storms to gauge its generality
- IAFS is tested in a simulated forecast scenario on a recent, significant ice storm, to evaluate its forecasting capability

To improve the efficiency of electric power transmission systems, the following contributions are made:

- an industry standard conductor thermal model is enhanced to incorporate the significant cooling effect of precipitation
- an optimal data sampling strategy for DTCR calculations is determined
- an Numerical Weather Prediction (NWP)-based DTCR system is evaluated to ascertain the forecast ampacity risk at different forecast horizons
- two intelligent systems to support planning and maintenance of power transmission infrastructure, based on weather data, are developed and tested; these include
 - an intelligent line routing system to identify an optimal route to maximize the ampacity of the line
 - an intelligent conductor selection system that can be used to assess the optimal conductor type for new line construction, or existing line upgrades, based on user specified optimization criteria
- a study is conducted to assess the potential for emission reduction using DTCR technology, and the optimal size of a renewable energy installation (wind farm) that could be constructed and integrated into the existing power grid

5.2 SIGNIFICANCE

Weather has a significant impact on the operation of power transmission infrastructure. In order for the power industry to remain competitive and cost effective, this impact needs to be well understood. The research work described in this thesis will significantly benefit the power industry, both in day-to-day operations and in long term planning, by giving it relevant supporting information for today's challenging problems. These include challenges caused by severe weather, line capacity congestion and the enormous costs related to transmission line construction and maintenance.

Icing phenomena can have a critical impact on the transmission infrastructure; therefore, it is imperative that an accurate forecast of the amount of icing that can accrete on a conductor be known. The optimized forecasting system, introduced in this thesis, will alert power system operators to conditions that can cause damage. This will allow utilities to take mitigative action, such as heating up the conductors using excess current, or having repair crews on standby to minimize the downtime experienced by customers.

Incorporating the precipitation cooling model into the IEEE Std. 738-2006 standard will ensure that sporadic but significant cooling by precipitation is accounted for. As a result, additional power can be transmitted over existing infrastructure using DTCR systems. Application of the model in DTCR deployments in regions with frequent rain and snow events could maximize the investment in DTCR technology, by identifying the maximum potential line capacity with minimal additional investment. Furthermore, the expanded

model can be used to increase the accuracy of line sag and aging calculations due to better estimates of line temperature.

Forecasts of the power transmission line ampacity and temperature will make it possible to maximize existing or future investment in transmission lines. Using NWP models to determine the available capacity will ensure that an assessment of the entire transmission line is made. This DTCR method considers all possible bottlenecks that can exist along the line, which can otherwise be missed by sparsely spaced sensors. Knowing the accuracy of ampacity forecasts will make it possible to ensure that adequate transmission capacity is available, capitalize on power trading opportunities, and save costs by avoiding or postponing line upgrade and expansion projects.

Using the enhanced thermal model alongside intelligent methods will help to prioritize upgrades, as only certain sections of power lines may be limiting the overall line capacity. These can be identified by the developed decision support system, based on high resolution weather data. Subsequently, the identified critical areas can undergo reconductoring, rather than replacing the entire line. This could be accomplished at a lower investment cost due to the targeted upgrades. Additionally, for utilities having a small number of sensors installed in their network, or relying on a limited number of meteorological stations for DTCR calculations, this approach will ensure that no parts of the transmission line exceed their design specifications. Consequently, this will prolong the lifespan of transmission conductors and ensure that no safety issues arise.

When planning new transmission lines, the weather impact can be assessed to find a line routing that minimizes the operating temperature of a new line. By selecting the best connecting regions, the available dynamic ampacity

of the transmission line can be maximized. Alternatively, the average line operating temperature can be minimized, leading to reduced power losses due to Joule heating, and reducing the potential for conductor degradation.

An additional side benefit of expanding existing transmission line capacity is that a greater number of green power generation sources can be connected to the grid, without prolonged delays associated with new line construction projects. This will, in turn, indirectly reduce the amount of greenhouse gases released into the atmosphere. Furthermore, in cases where the industry relies on a non-renewable resource, the total amount of consumed fuel could be reduced.

5.3 FUTURE WORK

This thesis describes several significant contributions to methods which help assess the impact of weather on the power transmission infrastructure. Nevertheless, there are still a number of potential opportunities to expand upon the research work presented.

The enhanced ice accretion forecasting system still has room for further refinement. The fuzzy engagement function used in IAFS consists of a bounded linear function. This function is crucial to identify the presence of freezing rain in forecast precipitation. It is possible that alternative functions, or a piecewise combination of multiple functions may yield additional improvements, by better separating the icing and non-icing conditions and describing the dependency between meteorological conditions and accretion. Next,

less variability in the values of the engagement function parameters can be expected if a larger, re-analyzed data set of ice accretion observations for ice storms were to be generated and used for parameter training. There is also potential for further increase in accuracy by using other combinations of Weather Research & Forecasting (WRF) parametrization options. The system uses a single WRF parametrization scheme selected based on its suitability for modelling winter weather and precipitation. While good performance has been achieved, additional gains may be attained using other combinations of WRF parametrization options. A more thorough testing of the system using storms from different geographic and climatic conditions would be beneficial to evaluate IAFS's general applicability. It is possible that a different set of optimal of engagement function parameters will be required for different climates. A comprehensive study would need to be conducted to assess this possibility.

The precipitation-based cooling model for DTCR also has many possibilities for refinement. Better approximations of line cooling related to heating and evaporation of precipitation are possible. Gains in accuracy can be achieved by employing more accurate estimates of the water surface temperature prior to evaporation. Improved modelling of the melting dynamics of frozen precipitation and ice on power lines may also increase the accuracy of the model. Additional factors may also play roles not accounted for in the current extension. For example, some precipitation could drip and be blown off the conductor surface before it is evaporated, or it may evaporate prior to reaching the temperature of the conductor.

To use NWP ampacity forecasts operationally, additional processing steps will need to be performed. First, model output statistics should be applied as

a post-processing step to improve the accuracy of the forecast weather time series data [115]. Second, a risk assessment model will need to be developed to differentiate between high risk and low risk ampacity forecasts. It is hypothesized that only certain weather conditions, such as calm conditions with intermittent gusts of wind, bring excessive risk. Having knowledge of these types of cases would inform utility operators when ampacity forecasts are safe to use (i.e. within an acceptable margin of error), and when they should not be trusted, because they could potentially lead to conductor degradation or failure.

Further refinement of the line routing procedures is expected to provide greater gains in the available line capacity. As the system currently makes use of a regular grid to position the line, only four line directions were considered; however, a more accurate assessment of a potential line segment's ampacity would be attained if an evaluation of the wind direction was calculated with respect to the true line orientation. Additional gains are expected to be achieved by incorporating a hierarchical approach to discovering the optimal line paths. This will allow the routing system to be more flexible, by permitting the addition of constraints at a lower resolution (to e.g. avoid specific regions), thereby providing a mechanism to select which areas a line can be constructed through, and then allowing the system to refine the selection. Finally, the line routing system would benefit from expanding the cost function to allow for multi-objective optimization. This could take into consideration business factors such as the power line construction cost at a particular location, for the construction and acquisition of land; the transmission capacity available at particular location for the specified conductor type; and environmental factors that will need to be addressed at that location.

To improve the presented line upgrading system, a more comprehensive dataset is required. Ideally, the meteorological data must span a longer time frame to ensure that the period considered is not an anomalous one, in comparison with the recent 30-year climate statistics. Additionally, given our knowledge of global climate change, using hindcasts may not be adequate enough to assess the operating conditions in the future. To account for this, simulations of future climate with global climate models could be performed, along with meteorological hindcasts, in order to obtain a better image of future operating conditions. Such an extension would permit utility operators to assess how a given trend in the region's weather patterns may influence the operation of transmission lines, and to suggest necessary proactive interventions.

BIBLIOGRAPHY

- [1] W. T. Jewell, "Electric industry infrastructure for sustainability: Climate change and energy storage," in *IEEE Power Engineering Society General Meeting*, Jun. 2007, pp. 1–3.
- [2] J. Pell, "Implications of global climate change for the U.S. national power grid," in *IEEE Power Energy Society General Meeting*, Jul. 2009, pp. 1–3.
- [3] "Underground vs overhead distribution wires - issues to consider," Tech. Rep., Edison Electric Institute, Washington, DC.
- [4] "National electric transmission congestion study," Tech. Rep., United States Department of Energy, Dec. 2009.
- [5] P. Fox-Penner, "Easing gridlock on the grid: Electricity planning and siting compacts," *The Electricity Journal*, vol. 14, no. 9, pp. 11–30, 2001.
- [6] T. Mount, A. Lamadrid, S. Maneevitjit, B. Thomas, and R. Zimmerman, "Evaluating the net benefits of investing in new wind and transmission capacity on a network," in *42nd Hawaii International Conference on System Sciences (HICSS 2009)*, Jan. 2009, pp. 1–10.
- [7] G. Orawski, "Overhead lines - the state of the art," *Power Engineering Journal*, vol. 7, no. 5, pp. 221–231, Oct. 1993.
- [8] R. J. Thomas, J. T. Whitehead, H. Outhred, and T. D. Mount, "Transmission system planning-the old world meets the new," *Proceedings of the IEEE*, vol. 93, no. 11, pp. 2026–2035, 2005.
- [9] C. Crocombette, "The weather impact on the transmission of electricity in France," in *8th European Conference on Applications of Meteorology*, Oct. 2007, ECAM'07.
- [10] G. F. Moore, *BICC Electric Cables Handbook*, p. 742, Blackwell Publishing, 1997.
- [11] F. Kiessling, P. Nefzger, J. Nolasco, and U. Kaintzyk, *Overhead Power Lines: Planning, Design, Construction*, Springer, 2003.
- [12] C. R. Sullivan, V. F. Petrenko, J. D. McCurdy, and V. Kozliouk, "Breaking the ice [transmission line icing]," *IEEE Ind. Appl. Mag.*, vol. 9, no. 5, pp. 49–54, 2003.

- [13] Y. Sakamoto, "Snow accretion on overhead wires," *Philos. T Roy. Soc. A*, vol. 358, no. 1776, pp. 2941–2970, Nov. 2000.
- [14] R. J. Hauer, J. O. Dawson, and L. P. Werner., *Trees and Ice Storms: The Development Ice Storm-Resistant Urban Tree Populations*.
- [15] D. A. Gay and R. E. Davis, "Freezing rain and sleet climatology of the southeastern USA," *Climate Res.*, vol. 3, pp. 209–220, 1993.
- [16] S. Changnon and T. Creech, "Sources of data on freezing rain and resulting damages," *J. Appl. Meteorol.*, vol. 43, pp. 1514–1518, 2003.
- [17] E. Lecomte, A. Pang, and J. Russell, *Ice Storm '98*, ICLR Research Paper Series, 1998.
- [18] P. Zsolt, *Modelling and simulation of the ice melting process on a current-carrying conductor*, Ph.D. thesis, University of Quebec in Chicoutimi, 2006.
- [19] R. W. Lenhard, "An indirect method for estimating the weight of glaze on wires," *Am. Meteor. Soc.*, vol. 36, pp. 1–5, 1955.
- [20] P. M. Chaine and G. Castonguay, "New approach to radial ice thickness concept applied to bundle-like conductors," *Climate Res.*, pp. 1–11, 1974.
- [21] E. J. Goodwin, J. D. Mozer, A. M. Di Gioia Jr., and B. A. Power, "Predicting ice and snow loads for transmission lines," in *First Int. Workshop on Atmospheric Icing of Structures*, 1982, pp. 267–273.
- [22] L. Makkonen, "Modeling power line icing in freezing precipitation," *Atmos. Res.*, vol. 46, pp. 131–142, 1998.
- [23] K. F. Jones, "A simple model for freezing rain ice loads," *Atmos. Res.*, vol. 46, pp. 87–97, 1998.
- [24] K. Szilder, "The density and structure of ice accretion predicted by a random-walk model," *Q. J. Roy. Meteor. Soc.*, vol. 119, pp. 907–924, 1993.
- [25] L. Makkonen, "Models for the growth of rime, glaze, icicles and wet snow on structures," *Philos. Trans. R. Soc. Lond., Ser. A*, vol. 358, pp. 2913–2939, 2000.
- [26] T. Vassbo, J. E. Kristjansson, S. Fikke, and L. Makkonen, "An investigation of the feasibility of predicting icing episodes using numerical weather prediction model output," in *Proc. 8th International Workshop on Atmospheric Icing on Structures (IWAIS)*, 1998, pp. 343–347.

- [27] G. Thompson, B. E. K. Nygaard, and L. Makkonen, "Using the weather research and forecasting (WRF) model to simulate ground/structural icing events," in *Proc. 13th International Workshop on Atmospheric Icing of Structures (IWAIS)*, 2009.
- [28] S. Dierer, R. Cattin, S. Muller, B. E. K. Nygaard, B. Steiner, and B. Calpini, "Modeling the risk of icing in switzerland," in *Proc. 13th International Workshop on Atmospheric Icing of Structures (IWAIS)*, 2009.
- [29] B. E. K. Nygaard and D. Nikolov, "Comparison between measured ice loads caused by freezing rain and corresponding simulations with a NWP model for the northeast part of Bulgaria," in *Proc. 13th International Workshop on Atmospheric Icing of Structures (IWAIS)*, 2009.
- [30] K. F. Jones, A. C. Ramsay, and J. N. Lott, "Icing severity in the December 2002 freezing-rain storm from ASOS data," *Mon. Wea. Rev.*, vol. 132, no. 7, pp. 1630–1644, 2004.
- [31] R. R. Czys and R. W. Scott, "A physically based, nondimensional parameter for discriminating between locations of freezing rain and ice pellets," *Wea. Forecasting*, vol. 11, pp. 591–598, Dec. 1996.
- [32] M. Baldwin, R. Treadon, and S. Contorno, "Precipitation type prediction using a decision tree approach with NMC's mesoscale ETA model," in *10th Conference on the Numerical Weather Prediction*, 1994, pp. 30–31.
- [33] J. Ramer, "An empirical technique for diagnosing precipitation type from model output," in *5th International Conference on Aviation Weather Systems*, Aug. 1993, pp. 227–230.
- [34] A. T. DeGaetano, B. N. Belcher, and P. L. Spier, "Short-term ice accretion forecasts for electric utilities using the weather research and forecasting model and a modified precipitation-type algorithm," *Wea. Forecasting*, vol. 23, no. 5, pp. 838–853, 2008.
- [35] P. Musilek, D. Arnold, and E. Lozowski, "An ice accretion forecasting system (IAFS) for power transmission lines using numerical weather prediction," *Scientific Online Letters on the Atmosphere (SOLA)*, vol. 5, pp. 25–28, 2009.
- [36] J. Heckenbergerova, P. Musilek, Md. M. I. Bhuiyan, D. Koval, and E. Pelikan, "Identification of critical aging segments and hotspots of power transmission lines," in *9th International Conference on Environment and Electrical Engineering (EEEIC)*, May 2010, pp. 175–178.
- [37] "IEEE standard for calculating the current-temperature of bare overhead conductors," *IEEE Std 738-2006 (Revision of IEEE Std 738-1993)*, pp. 1–59, 2007.

- [38] CIGRE Working Group 22.12, "Thermal behaviour of overhead conductors," Tech. Rep., 2002.
- [39] N. P. Schmidt, "Comparison between IEEE and CIGRE ampacity standards," *IEEE Transactions on Power Delivery*, vol. 14, no. 4, pp. 1555–1559, Oct. 1999.
- [40] H. E. House and P. D. Tuttle, "Current-carrying capacity of ACSR," *Power Apparatus and Systems, Part III. Transactions of the American Institute of Electrical Engineers*, vol. 77, no. 3, pp. 1169–1173, Apr. 1958.
- [41] "Transmission conductors thermal ratings," *Paper 68-TAP-29, Report by Transmission Advisory Panel, East Central Area Reliability Coordination Agreement*, 1968.
- [42] W. Z. Black and R. L. Rehberg, "Simplified model for steady state and real-time ampacity of overhead conductors," *IEEE Transactions on Power Apparatus and Systems*, vol. 104, no. 10, pp. 2942–2953, Oct. 1985.
- [43] T. Y. Wong, J. A. Findlay, and A. N. McMurtrie, "An on-line method for transmission ampacity evaluation," *IEEE Power Engineering Review*, vol. 2, no. 2, pp. 19, Feb. 1982.
- [44] "Dynamic thermal line rating - phase C, D and E," Tech. Rep. EP81-6, Empire State Electric Energy Research Corp., Washington, DC, Dec. 1985.
- [45] M. W. Davis, "A new thermal rating approach: The real time thermal rating system for strategic overhead conductor transmission lines – Part I: General description and justification of the real time thermal rating system," *IEEE Transactions on Power Apparatus and Systems*, vol. 96, no. 3, pp. 803–809, 1977.
- [46] M. W. Davis, "A new thermal rating approach: The real time thermal rating system for strategic overhead conductor transmission lines – part ii: Steady state thermal rating program," *IEEE Transactions on Power Apparatus and Systems*, vol. 96, no. 3, pp. 810–825, May 1977.
- [47] V. T. Morgan, "Rating of bare overhead conductors for continuous currents," *Electrical Engineers, Proceedings of the Institution of*, vol. 114, no. 10, pp. 1473–1482, Oct. 1967.
- [48] Sural Company, "Product catalog – ACSR (aluminum conductor, steel reinforced)," .
- [49] J. L. Reding, "A method for determining probability based allowable current ratings for bpa's transmission lines," *IEEE Trans. Power Deliv.*, vol. PWRD-9, no. 1, pp. 153–161, 1994.

- [50] P. Zhang, M. Shao, A. R. Leoni, D. H. Ramsay, and M. Graham, "Determination of static thermal conductor rating using statistical analysis method," in *Third International Conference on Electric Utility Deregulation and Restructuring and Power Technologies*, 6-9 2008, pp. 1237–1243.
- [51] T. O. Seppa, "Reliability and real time transmission line ratings," Tech. Rep., The Valley Group - A Nexans Company, Ridgefield, CT, USA, 2007.
- [52] B. S. Howington and G. J. Ramon, "Dynamic thermal line rating summary and status of the state-of-the-art technology," *IEEE Transactions on Power Delivery*, vol. 2, no. 3, pp. 851–858, Jul. 1987.
- [53] A. Dino and A. Ketley, "Dynamic transmission line rating: Technology review," Tech. Rep. 208478-CR-001, Hydro Tasmania Consulting, 2009.
- [54] R. Adapa and D. A. Douglass, "Dynamic thermal ratings: monitors and calculation methods," in *Power Engineering Society Inaugural Conference and Exposition in Africa*, 2005, pp. 163–167.
- [55] D. A. Douglass and A. A. Edris, "Real-time-monitoring and dynamic thermal rating of power transmission circuits," *IEEE Transactions on Power Delivery*, vol. 11, no. 3, pp. 1407–1418, 1996.
- [56] J. F. Hall and A. K. Deb, "Prediction of overhead transmission line ampacity by stochastic and deterministic models," *IEEE Transactions on Power Delivery*, vol. 3, no. 2, pp. 789–800, Apr. 1988.
- [57] D. Roberts, P. Taylor, and A. Michiorri, "Dynamic thermal rating for increasing network capacity and delaying network reinforcements," in *SmartGrids for Distribution*, June 2008, pp. 1–4.
- [58] H. Bohme, S. Kornhuber, S. Markalous, M. Muhr, and T. Strehl, "Operation ideas for overhead transmission lines (OHTLs) by using information of online temperature monitoring systems," in *Proc. 15th Int. Symp. High Voltage Engineering (ISH 2007)*, Aug. 2007, pp. 404–405.
- [59] P. M. Callahan and D. A. Douglass, "An experimental evaluation of a thermal line uprating by conductor temperature and weather monitoring," *Power Delivery, IEEE Transactions on*, vol. 3, no. 4, pp. 1960–1967, Oct. 1988.
- [60] J. Ausen, B. F. Fitzgerald, E. A. Gust, D. C. Lawry, J. P. Lazar, and R. L. Oye, "Dynamic thermal rating system relieves transmission constraint," in *IEEE 11th International Conference on Transmission Distribution Construction, Operation and Live-Line Maintenance*, Oct. 2006.
- [61] A. K. Deb, "Dynamic thermal rating system of overhead transmission lines using internet weather data," in *Cigre Cairns Symp*, 2004.

- [62] W. J. Steeley, B. L. Norris, and A. K. Deb, "Ambient temperature corrected dynamic transmission line ratings at two PG&E locations," *IEEE Transactions on Power Delivery*, vol. 6, no. 3, pp. 1234–1242, Jul. 1991.
- [63] L. J. Chaput, "Understanding LiDAR data - How utilities can get maximum benefits from 3D modeling," Tech. Rep., WIRE Services, Nov. 2007.
- [64] G. J. Klir and B. Yuan, *Fuzzy Sets and Fuzzy Logic: Theory and Applications*, Prentice Hall PTR, 1 edition, May 1995.
- [65] G. Chen and T. T. Pham, *Introduction to Fuzzy Sets, Fuzzy Logic, and Fuzzy Control Systems*, CRC, Nov. 2000.
- [66] L. A. Zadeh, "Fuzzy sets," *Information Control*, vol. 8, pp. 338–353, 1965.
- [67] W. Pedrycz and F. Gomide, *Fuzzy Systems Engineering: Toward Human-Centric Computing*, Wiley-IEEE Press, 2007.
- [68] F. O. Karry and C. Silva, *Soft Computing and Intelligent Systems Design*, Addison Wesley, 2004.
- [69] J. H. Holland, *Adaptation in natural and artificial systems*, MIT Press, Cambridge, MA, USA, 1992.
- [70] D. E. Goldberg, *Genetic Algorithms in Search, Optimization and Machine Learning*, Addison-Wesley Longman Publishing Co., Inc., Boston, MA, USA, 1989.
- [71] M. Mitchell, *An Introduction to Genetic Algorithms*, MIT Press, Cambridge, MA, USA, 1996.
- [72] S. Russell and P. Norvig, *Artificial Intelligence: A Modern Approach*, pp. 111–114, Pearson Education, 2003.
- [73] S. Forrest, "Genetic algorithms: principles of natural selection applied to computation.," *Science*, vol. 261, pp. 715–721, 1993.
- [74] A. H. Wright, "Genetic algorithms for real parameter optimization," in *Foundations of Genetic Algorithms*, 1991, pp. 205–218.
- [75] E. W. Dijkstra, "A note on two problems in connexion with graphs," in *Numerische Mathematik*, vol. 1, pp. 269–271. Mathematisch Centrum, Amsterdam, The Netherlands, 1959.
- [76] R. Graham and M. Evans, "Strength and weaknesses of p-type algorithms," Tech. Rep., Dec. 2008.

- [77] R. B. Stull, "Wet-bulb temperature from relative humidity and air temperature," *J. of Applied Meteorology and Climatology*, vol. 50, no. 11, pp. 2267–2269, 2011.
- [78] A. K. Singh, H. Singh, S. P. Singh, and R. L. Sawhney, "Numerical calculation of psychrometric properties on a calculator," *Build. Environ.*, vol. 37, pp. 415–419, Apr. 2002.
- [79] A. C. Best, "The size distribution of raindrops," *Q. J. Roy. Meteor. Soc.*, vol. 76, no. 327, pp. 16–36, 1950.
- [80] P. Pytlak, P. Musilek, E. Lozowski, and D. Arnold, "Evolutionary optimization of an ice accretion forecasting system," *Mon. Wea. Rev.*, vol. 138, no. 7, pp. 2913–2929, Jul. 2010.
- [81] NCDC, "Storm event database," Tech. Rep., 2009.
- [82] W. C. Skamarock, J. B. Klemp, J. Dudhia, D. O. Gill, D. M. Barker, M. G. Duda, X. Y. Huang, W. Wang, and J. G. Powers, "A description of the advanced research WRF version 3," Tech. Rep., NCAR/TND475+STR, NCAR, 2008.
- [83] F. Mesinger et al., "NCEP North American Regional Reanalysis," in *15th Symp. On Global Change and Climate Variations*, Jan. 2004, pp. 11–15.
- [84] K. F. Jones, *Ice accretion in freezing rain*, US Army Corps of Engineers, Cold Regions Research & Engineering Laboratory (CRREL), 1996.
- [85] R. O. Duda, P. E. Hart, and D. G. Stork, *Pattern Classification*, Wiley-Interscience, 2 edition, Nov. 2000.
- [86] J. Hosek, P. Musilek, E. Lozowski, and P. Pytlak, "Forecasting severe ice storms using numerical weather prediction: the March 2010 Newfoundland event," *Natural Hazards and Earth System Science*, vol. 11, no. 2, pp. 587–595, 2011.
- [87] Truro Daily News, "Ice storm in N.L. knocks out power for days, 7,000 still in dark on Sunday," 2010.
- [88] T. A. Short, *Electric Power Distribution Handbook*, CRC Press, 2007.
- [89] Canadian Standards Association, "Overhead systems," Tech. Rep. C22.3 No. 1-06, Oct. 2006.
- [90] P. Pytlak, P. Musilek, E. Lozowski, and J. Toth, "Modelling precipitation cooling of overhead conductors," *Electric Power Systems Research*, vol. 81, no. 12, pp. 2147–2154, Jul. 2011.
- [91] W. H. McAdams, *Heat Transmission*, McGraw-Hill Book Company Inc, New York, 1959.

- [92] L. C. Burmeister, *Convective Heat Transfer*, Wiley-Interscience, 2 edition, 1993.
- [93] G. Poots, *Ice and Snow Accretion on Structures*, Research Studies Press Ltd., Taunton, Somerset, England, 1996.
- [94] C. Antoine, "Tensions des vapeurs: nouvelle relation entre les tensions et les temperatures," *Comptes Rendus des Seances de l'Academie des Sciences*, vol. 107, pp. 681–684, 778–780, 836–837, 1888.
- [95] K. Wark and D. E. Richards, *Thermodynamics*, McGraw-Hill College, 1988.
- [96] R. R. Rogers and M. K. Yau, *A Short Course in Cloud Physics*, Pergamon press, 2e edition, 1989.
- [97] J. Hosek, P. Musilek, E. Lozowski, and P. Pytlak, "Effect of time resolution of meteorological inputs on dynamic thermal rating calculations," *IET Generation, Transmission Distribution*, vol. 5, no. 9, pp. 941–947, Sept. 2011.
- [98] D. Hanslian and L. Pop, "The technical potential of wind energy and a new wind atlas of the Czech Republic," in *Proc. European Wind Energy Conf. and Exhibition (EWEC 2008)*, Apr. 2008, pp. 1–10.
- [99] R. B. Stull, *An introduction to boundary layer meteorology*, Kluwer, 1988.
- [100] J. D. Glover and M. Sarma, *Power system analysis and design*, Brooks/Cole, 3 edition, 2002.
- [101] P. D. Welch, "The use of fast fourier transform for the estimation of power spectra: a method based on time averaging over short, modified periodograms," *IEEE Trans. Audio Electroacoust.*, vol. AT-15, pp. 70–75, 1967.
- [102] D. Poggi and G. G. Katul, "Turbulent intensities and velocity spectra for bare and forested gentle hills: flume experiments," *Bound.-Layer Meteorol.*, , no. 129, pp. 25–46, 2008.
- [103] J. Heckenbergerova, P. Musilek, and K. Filimonenkov, "Assessment of seasonal static thermal ratings of overhead transmission conductors," in *IEEE Power and Energy Society (PES) General Meeting*, Jul. 2011, pp. 1–8.
- [104] EPRI, "Conductor and associated hardware impacts during high temperature operations: issues and problems," Tech. Rep., Electrical Power Research Institute, 1999.

- [105] D. McCollor and R. B. Stull, "Evaluation of probabilistic medium-range temperature forecasts from the north american ensemble forecast system," *Weather and Forecasting*, vol. 24, no. 1, pp. 3–17, 2009.
- [106] P. Pytlak and P. Musilek, "An intelligent weather-based system to support optimal routing of power transmission lines," in *IEEE 10th Electrical Power and Energy Conference (EPEC 2010)*, Aug. 2010, pp. 1–6.
- [107] P. Pytlak and P. Musilek, "Selective upgrading of transmission lines using DTCR," in *IEEE 25th Canadian Conference on Electrical and Computer Engineering (CCECE 2012)*, Jun. 2012, pp. 1–4.
- [108] P. Pytlak, P. Musilek, and J. Doucet, "Using dynamic thermal rating systems to reduce power generation emissions," in *IEEE Power and Energy Society (PES) General Meeting*, Jul. 2011, pp. 1–7.
- [109] Jean-Pierre Bourdier, "Bois, charbon, petrole, gaz, nucleaire et autres. Memes problemes ?," *La Jaune et La Rouge*, May 2000.
- [110] "Compilation of emission factors," Tech. Rep. AP-42, United States Environmental Protection Agency, 2008.
- [111] "Planning for Alberta's power future," Tech. Rep., Alberta Electric System Operator, Jan. 2007.
- [112] "Future demand and energy outlook (2009-2029)," Tech. Rep., Alberta Electric System Operator, Feb. 2010.
- [113] "Wind power in Alberta," Tech. Rep., Alberta Electric System Operator, Sept. 2010.
- [114] "AESO long-term transmission system plan," Tech. Rep., Alberta Electric System Operator, 2009.
- [115] K. Filimonenkov, "Weather-based thermal rating of overhead power transmission lines," M.S. thesis, University of Alberta, 2011.
- [116] G. Thompson, R. M. Rasmussen, and K. Manning, "Explicit forecasts of winter precipitation using an improved bulk microphysics scheme. Part I: Description and sensitivity analysis," *Mon. Wea. Rev.*, vol. 132, no. 2, pp. 519–542, 2004.
- [117] E. J. Mlawer, S. J. Taubman, P. D. Brown, M. J. Iacono, and S. A. Clough, "Radiative transfer for inhomogeneous atmospheres: RRTM, a validated correlated-k model for the longwave," *J. Geophys. Res.*, vol. 102, 1997.
- [118] J. Dudhia, "Numerical study of convection observed during the winter monsoon experiment using a mesoscale two-dimensional model," *J. Atmos. Sci.*, vol. 46, no. 20, pp. 3077–3107, 1989.

- [119] A. S. Monin and A. M. Obukhov, "Basic laws of turbulent mixing in the surface layer of the atmosphere," *Contrib. Geophys. Inst. Acad. Sci. USSR*, vol. 151, pp. 163–187, 1954.
- [120] T. G. Smirnova, J. M. Brown, and S. G. Benjamin, "Performance of different soil model configurations in simulating ground surface temperature and surface fluxes," *Mon. Wea. Rev.*, vol. 125, no. 8, pp. 1870–1884, 1997.
- [121] Z. I. Janjic, "Nonsingular implementation of the Mellor–Yamada level 2.5 scheme in the NCEP meso model," Tech. Rep. 437, NCEP, 2002.
- [122] J. S. Kain, "The Kain-Fritsch convective parameterization: An update," *J. Appl. Meteorol.*, vol. 43, no. 1, pp. 170–181, 2004.
- [123] S. Sukoriansky and B. Galperin, "Anisotropic turbulence and internal waves in stably stratified flows (QNSE theory)," *Physica Scripta*, vol. T132, no. 014036, pp. 1–8, 2008.
- [124] X. Aijun and P. Jonathan E., "Development of a land surface model. Part I: Application in a mesoscale meteorological model," *J. Appl. Meteorol.*, vol. 40, no. 2, pp. 192–209, 2001.
- [125] G. A. Grell and D. Devenyi, "A generalized approach to parameterizing convection combining ensemble and data assimilation techniques," *Geoph. Res. Lett.*, vol. 29, no. 14, pp. 1693, 2002.

A

WRF PARAMETERIZATION

The WRF NWP model contains a large number of customization options, described in detail in [82]. These options play a significant role in the accuracy of the generated forecast or hindcast. The strength and weaknesses of the various parameterization schemes depends on the simulation goals, the region of WRF application, and the resolution of the produced forecast. Additionally, the accuracy of some options depends on the season. In particular, for modelling icing on structures in the surface layer of the atmosphere using an NWP model, the choice of physical parameterization is crucial. As a result, no single optimal configuration set exists. WRF must be customized to a given location, resolution, forecast time and the application of the generated output.

The following is a list of significant WRF parameterization options chosen for the various studies in this thesis. Modifications to the selected schemes have been performed based on expert opinion, and as new, better parameterization options became available.

Table 30: WRF configuration for the IAFS GA optimization study.

Parameter	Selected Option
microphysics	Thompson ice, snow and graupel scheme [116]
longwave radiation	Rapid Radiative Transfer Model [117]
shortwave radiation	Dudhia scheme [118]
surface layer	Monin-Obukhov similarity theory [119]
land surface	RUC scheme [120]
boundary layer	Mellor-Yamada-Janjic scheme [121]
cumulus parameterization	Kain-Fritsch scheme [122]
grid nudging	yes

Table 31: WRF configuration for the Newfoundland 2010 ice storm event forecast.

Parameter	Selected Option
microphysics	Thompson ice, snow and graupel scheme [116]
longwave radiation	Rapid Radiative Transfer Model [117]
shortwave radiation	Dudhia scheme [118]
surface layer	Quasi-Normal Scale Elimination scheme [123]
land surface	Pleim-Xiu scheme [124]
boundary layer	Mellor-Yamada-Janjic scheme [121]
cumulus parameterization	Grell scheme [125]
grid nudging	no

Table 32: WRF configuration for the NWP DTCR verification study.

Parameter	Selected Option
microphysics	Thompson ice, snow and graupel scheme [116]
longwave radiation	Rapid Radiative Transfer Model [117]
shortwave radiation	Dudhia scheme [118]
surface layer	Pleim-Xiu scheme [124]
land surface	Pleim-Xiu scheme [124]
boundary layer	Mellor-Yamada-Janjic scheme [121]
cumulus parameterization	Grell scheme [125]
grid nudging	no

Table 33: WRF configuration for the optimal transmission line routing study.

Parameter	Selected Option
microphysics	Thompson ice, snow and graupel scheme [116]
longwave radiation	Rapid Radiative Transfer Model [117]
shortwave radiation	Rapid Radiative Transfer Model [117]
surface layer	Pleim-Xiu scheme [124]
land surface	Pleim-Xiu scheme [124]
boundary layer	Quasi-Normal Scale Elimination scheme [123]
cumulus parameterization	Grell scheme [125]
grid nudging	yes

B | CONDUCTOR PARAMETERS

Table 34 lists the essential properties of conductors used in the various studies presented in this thesis. Exact values quoted may vary depending on the conductor manufacturer.

Table 34: Conductor specifications obtained from manufacturers' data-sheets.

Parameter	Value				
Name	Linnet	Drake	Finch	Dipper	BlueBird
Nominal Rating [A]	529	907	1093	1229	1623
Diameter [mm]	8.31	28.12	32.84	35.21	44.75
Res. @ 25.0 °C [$\Omega \cdot \text{km}^{-1}$]	0.1701	0.07284	0.05052	0.0418	0.02953
Res. @ 75.0 °C [$\Omega \cdot \text{km}^{-1}$]	0.2036	0.08689	0.06463	0.0530	0.03215
Emissivity Coeff.	0.5	0.5	0.5	0.5	0.5
Absorption Coeff.	0.5	0.5	0.5	0.5	0.5
Has Steel Core	Yes	Yes	Yes	Yes	Yes